Heavy-ion Beam Transport in Plasma Channels – Transport Properties and Channel Stability

Vom Fachbereich Physik der
TECHNISCHEN UNIVERSITÄT DARMSTADT

zur Erlangung des Grades
eines Doktors der Naturwissenschaften
(Dr. rer. nat.)

genehmigte Dissertation von
Dipl.-Phys. Stephan Neff
aus Bensheim

Darmstadt 2005
D17

Referent: Prof. Dr. Dr. h.c./RUS Dieter H.H. Hoffmann
Korreferent: Prof. Dr. Markus Roth

Tag der Einreichung: 02.02.2005
Tag der Prüfung: 25.04.2005

Zusammenfassung

Gegenwärtige Entwürfe für schwerionengetriebene Trägheitsfusionsreaktoren erfordern Strahlströme von etlichen Kiloampere, die über eine Distanz von einigen Metern in der Reaktorkammer zum Fusionstarget transportiert werden müssen. Eine Möglichkeit, den Strahl zu transportieren, bietet der sogenannte *Assisted Pinched Transport*. Bei dieser Transportmethode werden die Ionenstrahlen zunächst mit einer adiabatischen Plasmalinse fokussiert und dann in einem Plasmakanal zum Fusionstarget transportiert. Der Plasmakanal erfüllt drei Funktionen: er neutralisiert die Raumladung und den Strom des Ionenstrahls und erzeugt zusätzlich ein sehr starkes azimutales Magnetfeld, das den Strahl am Verlassen des Kanals hindert. Dieses Vorgehen trennt den Fokussiervorgang vom Transport in der Kammer und verringert dadurch die Anforderungen an die Fokussierung des Strahls.

Diese Arbeit entstand in Zusammenarbeit mit dem *Lawrence Berkeley National Laboratory*, das den Assisted Pinched Transport Mode im Rahmen der ARIES Reaktorstudie untersucht. Der Schwerpunkt dieser Arbeit ist die Erzeugung von langen, freistehenden Plasmakanälen und die Untersuchung ihrer Dynamik einschließlich der Entstehung von magnetohydrodynamischen Instabilitäten. Ein weiterer Schwerpunkt ist die Untersuchung der Strahltransporteigenschaften mit Hilfe von Schwerionenstrahlen, die im Linearbeschleuniger UNILAC der *Gesellschaft für Schwerionenforschung* erzeugt wurden.

In früheren Transportexperimenten wurde eine Entladungskammer mit einem Durchmesser von 60 cm und einer Länge von 50 cm verwendet. Um näher an den Reaktorbedingungen zu sein, wurde die Kammer durch das Einfügen eines neuen Abschnitts um 50 cm verlängert, so dass nun Kanäle mit einer Länge von 1 m erzeugt werden können. Da die Verlängerung die Geometrie der Kammer wesentlich änderte, wurde es notwendig, das elektrische Feld zu optimieren. Aufgrund der Ergebnisse elektrostatischer Rechnungen wurden die drei Abschnitte der Kammer elektrisch isoliert und auf unterschiedliche Potentiale gesetzt, was das Absinken des elektrischen Feldes zur Kammermitte hin wesentlich reduzierte und somit das Erzeugen der Kanäle erleichterte.

Die Kanalerzeugung erfolgt in drei Schritten. Im ersten Schritt wird der Kanal initiiert. Dazu wird das Gas entweder mit dem Ionenstrahl ionisiert oder mit einem Laser erhitzt. Da unser Experiment einen Kohlendioxid-Laser verwendet, ist die Laser-Initiierung auf Gase mit einem geeigneten Absorptionsband, wie es zum Beispiel Ammoniak besitzt, beschränkt. Ioneninduzierte Kanäle wurden in vielen Gasen erzeugt, unter anderen Xenon und Krypton. Der Sinn der Initiierung ist es, Überschläge zur metallischen Wand der Kammer zu verhindern. Im zweiten Schritt wird eine kleine Entladung, der Prepulse, ausgelöst. Sie erhitzt das Gas und führt dadurch zu einer Reduktion der Gasdichte entlang der Achse. Das dadurch entstehende Dichteprofil stabilisiert die nachfolgende Hauptentladung, die den Transportkanal erzeugt. Die Entwicklung des Kanals stimmt qualitativ mit Simulationsergebnissen überein, die mit der eindimensionalen magnetohydrodynamischen Simulation CYCLOPS berechnet wurden. Die Kanäle sind stabil, lediglich bei hohen Gasdichten können Instabilitäten entstehen. Das Wachstum der Instabilitäten wurde in Ammoniak gemessen und ist in guter qualitativer Übereinstimmung mit den Vorhersagen eines einfachen magnetohydrodynamischen Modells. Die Transporteigenschaften des Kanals für Schwerionenstrahlen wurden untersucht und sind in guter Übereinstimmung mit den Erwartungen. Die Transporteigenschaften zeigen, dass die Stromdichte im Kanal homogen ist. Anhand der Meßergebnisse und mit Hilfe von theoretischen Abschätzungen und Simulationen für den Fall hoher Strahlströme konnten geeignete Kanalparameter für das Reaktorszenario abgeschätzt werden.

Abstract

Concepts for heavy-ion fusion (HIF) reactors require the transport of kiloampere ion beams over distances of several meters inside the reactor chamber. A possible solution for this task is to use assisted pinched transport (APT) for the final transport of the beam. This scheme uses an adiabatic plasma lens to focus the beam outside the chamber and a plasma channel to transport it inside the reactor chamber towards the fusion target at the center. The plasma channel has three functions: it neutralizes both the space charge and the current of the ion beam and furthermore creates a large azimuthal magnetic field that prevents the beam ions from leaving the channel. The appeal of the APT scheme is that it separates the focusing of the beam from the final transport, thus relaxing the focusing requirements of the beam.

The purpose of this study is to demonstrate the creation of long, free-standing channels and to study their magnetohydrodynamical stability and their transport properties for low-current heavy-ion beams inside the channels. It is the result of a collaboration with Lawrence Berkeley National Laboratory and thus contributes to the ARIES fusion reactor study. In combination with the results of detailed transport simulations for high-current heavy-ion beams, which are part of the ARIES study, the results of the experiments make it possible to map out a set of suitable operating parameters for the channel transport of beams with reactor-like parameters, for instance the required discharge current and plasma density.

Previous transport experiments at the Gesellschaft für Schwerionenforschung (GSI) used a discharge chamber that was 50 cm long and 60 cm in diameter. To get closer to reactor scales the chamber was extended by inserting a 50 cm long chamber section, resulting in a total length of 1 m. Since the prolongation changed the geometry of the chamber and thus the electric fields inside of it, it was necessary to optimize the fields by setting each section of the chamber to a separate potential. The electric setup was optimized with the help of detailed electrostatic calculations for the chamber.

The channels are created in a three-step process. After the channel initiation, which guides the discharge along the chamber axis, a prepulse, that is a small discharge, heats the gas on the axis, resulting in a rarefaction and thereby stabilizing the subsequent main discharge. Two methods of channel initiation were used successfully. Laser-initiated channels were created in ammonia and ion-beam initiated channels in various other gases, such as krypton and xenon. The evolution of the channels is consistent with results from a one-dimensional MHD simulation. The channels are stable for normal operating conditions. A detailed study of channels in ammonia revealed that the channels become unstable for high gas densities, when the prepulse can no longer be used. The instabilities show the characteristics of kink instabilities, and their growth is consistent with the predictions of a simple analytical model.

Proof-of-principle experiments demonstrate the transport of low-current heavy-ion beams.

The transport properties of the channel were studied and found to be consistent with the assumption of a homogeneous current density in the channel, leading to betatron oscillations. In combination with the results of simulations for the transport of high-current beams and theoretical estimates about the growth of beam-plasma instabilities, the experimental results yield an estimate for a suitable set of operating parameters for assisted pinched transport in a fusion reactor.

Contents

1. Introduction

The limited sources for fossil fuels and uranium and the necessity to curb the carbon-dioxide emission in order to limit the greenhouse effect make it necessary to search for new ways to generate electrical power. One possibility is to utilize nuclear fusion. The appeal of nuclear fusion lies in the fact that the fuel supply can be considered unlimited for all practical purposes and that it creates only small amounts of radioactive waste (mainly activated reactor walls and tritium, which is relatively short-lived), in contrast to nuclear fission. In addition, it would create less problems regarding nuclear proliferation than fission reactors. Unfortunately, fusion conditions are very hard to reach. The basic mechanism of stars, in which the gravitational pull of the fuel itself leads to ignition, is obviously not applicable to reactors.

There are two main concepts for fusion reactors, based on either magnetic or inertial confinement. In the case of magnetic confinement, a low-density, high-temperature plasma is contained at fusion conditions by large magnetic fields, whereas in the case of inertial confinement a small capsule with fuel is compressed by laser or ion beams so as to reach ignition conditions.

1.1. Heavy-ion fusion

In typical inertial fusion designs, the fuel, typically some milligrams of a mixture of deuterium and tritium (DT), must be compressed to densities of $400\,\mathrm{g/cm^3}$[Lin98]. To reach this high density, the fuel is located in a thin shell of frozen DT, which encloses a low density gas and is surrounded by an ablator, which absorbs the driver energy and compresses the fuel. This fusion pellet can be heated either directly or indirectly. In the indirect approach, the pellet is located in a high-Z enclosure, called a hohlraum, which is heated by the driver beams and compresses the pellet with x-rays. While the direct drive is more efficient than the indirect approach, it requires a very homogeneous irradiation, as otherwise strong instabilities develop, which disrupt the pellet before it can ignite. An indirect approach relaxes these symmetry requirements at the cost of a lower driver efficiency, since the conversion of the driver energy to hohlraum radiation is lossy. All in all, the reduction of the instability growth rate outweighs the efficiency loss. The hohlraum can be heated either by laser or heavy-ion beams. Heavy-ion beams are especially suited drivers for this scheme, as they have short absorption lengths, so that they do not penetrate into the hohlraum.

The target chamber, in which the target heating takes place, is exposed to the target debris and, more importantly, the neutrons generated during the fusion reactions. For a reactor to be economically feasible, the reactor chamber should be in use for at least ten years. To reach such a long life-cycle, it is necessary to use suitable materials for the wall and to reduce the neutron load. Various shielding concepts have been proposed for this purpose.

Properties	**Neutralized Ballistic Transport**	**Plasma Channels**	**Self-Pinch**
Number of ion beams	60-200	2	100
Gas pressure (Torr)	0.001	1-10	0.001-0.1
Level of study	simulations	simulations and experiments	simulations
Advantages	best studied	simpler design and better shielding	simpler design

Table 1.1.: A comparison of the three final transport methods and reactor parameters for the thick-liquid wall scenario (chamber radius 3 m). The channel-transport mode can also be used in dry-wall and wetted-wall shielding scenarios.

Three different chamber designs are currently under discussion[Ros04]: the dry wall concept, in which the radiation load is reduced by simply increasing the chamber radius; the wet wall concept, in which the walls are wetted with a liquid that absorbs a part of the neutrons; and finally the thick-liquid wall scenario[Saw00], in which liquid jets shield the chamber walls. The use of shielding liquids in the last two concepts makes it possible to use smaller chambers than in the first scenario.

In the case of heavy-ion beam fusion, the shielding of the chamber and the beam transport inside the chamber are strongly linked, since the difficulties in transporting the ion beams naturally increase with the chamber radius. Moreover, concepts which work with a large number of ion beams are much harder to implement in a thick-liquid wall chamber than in a dry wall chamber, since the beams must not hit the liquid jets during transport. The required beam currents are determined by the total energy that is necessary to ignite the target and the energy per ion, which depends on its mass and velocity. Currently, most schemes suggest particle energies of roughly 15 MeV/u, since this keeps the accelerator costs within reasonable limits and the stopping range of the ions is short enough for the absorbers mounted in the hohlraum target. The duration of the beam pulse is usually limited to 10 ns, so that particle beam currents in the kiloampere range are required, depending on which ion species is used. These high currents make the beam transport very challenging, because the beam has to travel over a distance of several meters and must still hit a target area of 1 cm^2 and no magnets can be used inside the target chamber, as they would be exposed to strong radiation which would reduce their lifetime significantly.

The ARIES reactor study investigates three schemes for final transport[Ros04, Wel02]: neutralized-ballistic transport, self-pinched transport, and plasma-channel transport, also called assisted pinched transport. Table 1.1 gives an overview of the different schemes. Neutralized-ballistic transport is the main line approach, whereas the other schemes are alternatives, which would simplify the chamber and accelerator design. All of these schemes reduce the self-fields of the beams, so that they can reach the target at the center.

In the case of neutralized-ballistic transport, the basic idea is to split the beams into a large number of small beams and focus the beams individually with magnets placed outside the chamber. Typical designs operate with more than 100 beams. In combination with a par-

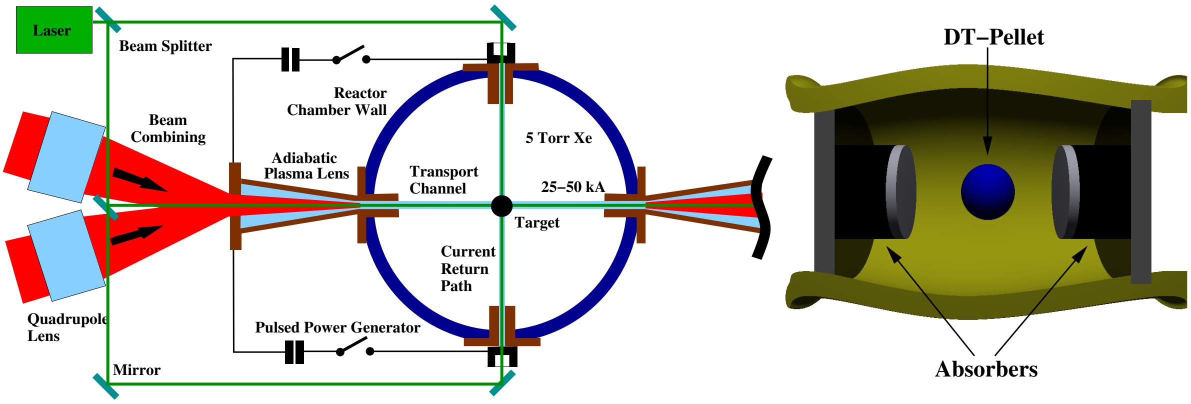

Figure 1.1.: Scheme for a heavy-ion fusion reactor with channel transport and a simplified sketch of a target proposed for this reactor concept. The actual target is more complicated, as it uses symmetry shields to improve the irradiation of the pellet.

tial neutralization of the beam charge, which is reached by sending it through a low-density plasma, this reduces the space charge and self-current sufficiently to transport them other several meters to the center of the chamber[Wel01].

Self-pinched transport also works with roughly 100 beams, but uses a low-pressure background gas in the chamber. The high-current ion beam creates free electrons in the gas by impact ionization. These free electrons provide neutralization for the space-charge effects and the beam current. Simulations and experiments for protons indicate good beam transport capabilities[Wel02, Ott00], yet experiments with high-current heavy-ion beams are still missing and will not be possible in the near future.

1.2. Assisted Pinched Transport

In contrast to these methods, assisted pinched transport works with only two ion beams to heat the fusion target. The ion beams are first focused by an adiabatic plasma lens and then transported inside a plasma channel to the target at the center of the chamber. The plasma of the discharge channels reduces the large self-fields of the beam, since it has many free electrons which neutralize the space charge and the current of the beam. In addition, the discharge also creates a large azimuthal magnetic field, which counteracts the spreading of the beam[Ott80].

Figure 1.1 shows a schematic view of a heavy-ion fusion reactor with plasma channel transport[Tau96b], and a sketch of a hybrid target with two beam absorbers[Cal02, Tab97, Lin98, Atz04] which is proposed for this transport scheme. The beam focusing system consists of three sections: a beam matching section, an adiabatic plasma lens, and the transport channel. In the matching section, quadrupole magnets combine the beams from the accelerators and focus them into the adiabatic plasma lens. The plasma lens reduces the beam diameter to 1 cm and guides the beam into the chamber. Inside the chamber, the plasma channel ensures the transport of the ion beam to the target at the center.

As indicated in Figure 1.1, the channels have the form of a ‘cross’: the anodes are mounted on the beam axis, whereas the cathodes are mounted on the vertical axis. In the created ‘crossed’ discharge, the horizontal channels transport the beam, whereas the vertical ones provide a path for the return current. To create this rather special shape, a short-pulse laser ionizes the gas, thereby guiding the subsequent discharge.

1.3. Transport channel experiments

In order to check the feasibility of this scheme, experiments that research the transport capabilities of the channel, its dynamics and its stability are necessary. In the first experiments, the channels were initiated by wire discharges, but this mechanism cannot be used repeatedly, as required in a reactor. To get closer to reactor conditions, transport experiments with laser-initiated channels were started in the 1980s.

The idea of channel transport originated from the Naval Research Laboratory and resulted in a series of theoretical and experimental studies[Ott79, Col80, Ott80, Ott81b, Ott81a, Ott82, Hub92, You93]. The studies resulted in experiments demonstrating the transport of a 1.2 MeV proton beam that was 2 cm in diameter and had a current of 100 kA in wall-stabilized discharge channels.

Another transport experiment was located at the *Sandia National Laboratories* and used 1 MeV protons [Ols81b, Ols81a, Ols82]. The channels were created in a glass tube, which was 9 cm in diameter, 50 cm in length, and filled with 5 to 25 mbar of ammonia. The channels, 6 mm in diameter and with a maximum current of 45 kA, reached a transport efficiency of over 50 % for 1 MeV protons.

In 1995 the *Lawrence Berkeley National Laboratory* (LBNL) started its plasma channel experiment[Tau96b]. The experiment studied the channel dynamics, but did not include beam transport measurements. The discharge chamber was a metal cuboid with the dimensions $41\,\mathrm{cm} \times 30\,\mathrm{cm} \times 28\,\mathrm{cm}$. The electrodes had an outer diameter of 15 cm, an inner diameter of 13 mm, and a length of 10 cm and were insulated from the walls with Plexiglas. The chamber gas was nitrogen, mixed with traces of benzene to yield a better absorption of the KrF laser which was used to initiate the channel. The setup used a two-staged discharge, consisting of a prepulse and a main discharge. The experiment succeeded in creating stable channels with currents of up to 55 kA[Tau96c].

Based on the results of this experiment and in close collaboration with the LBNL, the *Gesellschaft für Schwerionenforschung* (GSI) started its channel transport experiment in 1998. The experiment, which is the subject of this thesis, studies the transport of heavy-ion beams in the plasma channels and the evolution and stability of the channels. The original setup used a metal chamber with a diameter of 60 cm and a length of 50 cm (distance between the electrodes). In 2003, this chamber was prolonged to 1 m to get closer to reactor dimensions. In addition to laser-initiated channels, ion-beam-initiated channels were successfully created.

The goal of this thesis is to demonstrate the creation of long, free-standing discharge channels and to study their stability and their transport properties for low-current heavy-ion beams. In addition, simulation results and theoretical estimates are used to determine an operating window for the assisted pinched transport mode, that is the range of parameters for which a successful beam transport is possible. These parameters can be divided into two groups: the beam parameters and the channel parameters. The beam parameters, that is the ion species, the kinetic energy, and the beam current, are largely determined by the design of the fusion target. Starting from this set of parameters, it is now necessary to determine the operating parameters for creating the channel, including the ambient gas pressure and the discharge current. Naturally, due to the lack of high-current heavy-ion beams, the experiments in these study are only proof-of-principle experiments which demonstrate the beam transport for low current beams and must therefore be supplemented by theoretical simulations for beams with reactor parameters.

This thesis consists of three major parts. Section 2 explains the theoretical background necessary for understanding the channel dynamics and the ion beam transport and discusses effects which might impede successful beam transport. These remarks are supplemented with estimates for channel and beam parameters typical for our experimental setup and the reactor scenario. Also mentioned are the results of recent simulations of the transport of high-current heavy-ion beams in an assisted pinched transport scheme consisting of a 125 cm long plasma lens and a 325 cm long plasma channel. The results of these simulations are used to determine a suitable set of operating parameters. Section 3 focuses on the experimental setup. The components of the setup are discussed in detail, including an electrostatic calculation of the electric field in the chamber prior to the discharge. The section concludes with an explanation of the channel creation, illustrated with the results of a one-dimensional magnetohydrodynamical simulation. Section 4 reports on the results of our measurements, which focused on beam transport and channel instabilities. Finally, the results are summarized and their consequences for the use of the assisted pinched transport mode in a fusion reactor are discussed.

2. Basic properties of channel transport

This chapter gives an overview of the processes involved in plasma channel beam transport. Starting with a short summary of the basic plasma physics required in plasma channel transport, the essential factors for the pinch dynamics and the pinch stability will be discussed. After the discussion of betatron oscillations, which are typical of the transport of low-current beams and some ray-tracing calculations for low-current beams, the effects of large self-fields are treated. This includes the magnitude of the space-charge forces for a non-neutralized beam and the discussion of charge and current neutralization. Furthermore, the interaction between the beam and the channel is analyzed, including a short overview of possible beam-plasma instabilities. The chapter concludes with a short overview over recent computer simulations of assisted pinched transport of high-current beams, which are part of the ARIES reactor study, and an estimate for suitable operating parameters for the APT mode.

2.1. Plasma

During the channel creation, a high-current discharge ionizes the gas, turning it into plasma. Plasma, which is also called the fourth state of matter, is basically a collection of free electrons and ions. In addition, neutral particles may form a part of the plasma. The modelling of plasmas is a complex task, since short-range interactions between particles as well as collective long-range interactions are involved. The short-range interactions are caused by collisions of particles, the long-range electromagnetic forces by the moving ions and electrons. For a complete description of the plasma, both effects must be taken into account.

An important scale in plasma physics is the Debye length. On scales smaller than the Debye length, the plasma must be treated as a collection of individual particles. On larger scales, the ion densities (n_i) and the electron density (n_e) are connected by the condition of *quasi-neutrality*

$$n_e \approx \sum_i Z_i \, n_i \tag{2.1}$$

where i denotes different ion charge states and Z_i is the charge state of an ion species. The quasi-neutrality is caused by the enormous energy that charge separation on a macroscopic scale requires. The Debye length can be derived by considering charged particles in a potential ϕ. The total energy of the particles is the sum of the kinetic and the potential energy

$$E_{\text{tot}} = \frac{1}{2} m v^2 + q\phi \tag{2.2}$$

For a Maxwellian particle ensemble

$$f(x,v) \propto \exp\left(-(m v^2/2 + q\phi(x))/(k_B \cdot T)\right) \tag{2.3}$$

the density is proportional to $\exp(-q\phi/(k_B \cdot T))$, yielding the densities

$$n_e = n_0 \cdot \exp(e\phi/T_e); \qquad Z_i n_i = n_0 \cdot \exp(-eZ_i\phi/(k_B \cdot T_i)) \tag{2.4}$$

The spatial charge distribution is determined by the Poisson equation. Inserting the ansatz for the densities into the equation yields

$$\varepsilon_0 \Delta\phi = e(n_e - Z n_i) = e n_0 \left[\exp(e\phi/k_B \cdot T_e) - \exp(-e Z \phi/k_B \cdot T_i)\right] \tag{2.5}$$

This equation can be solved analytically, if the arguments of the exponential functions are small (this assumption is *not* valid near the electrodes). Using a Taylor expansion to first order yields[Gol98]

$$\Delta\phi \approx \frac{e n_0}{\varepsilon_0} \left[e\phi/(k_B \cdot T_e) + eZ\phi/(k_B \cdot T_i)\right] = \frac{e^2 n_0}{T_e \varepsilon_0}(1 + Z T_e/T_i)\,\phi = \frac{1}{\lambda_D^2}\,\phi \tag{2.6}$$

where we introduced the Debye length λ_D. The solution of this differential equation is proportional to $\exp(-x/\lambda_D)$, so the Debye length is a shielding scale. Typically the contribution of the ions is neglected and we get the standard formula (e.g. [Hut00])

$$\lambda_D = \sqrt{\frac{\varepsilon_0 k_B T_e}{e^2 n_0}} \tag{2.7}$$

The number of electrons in a sphere with a radius of one Debye length is

$$N_D = \frac{4\pi}{3} \lambda_D^3 \cdot n_0 \tag{2.8}$$

This number also gives a lower limit for the scale on which the assumption of quasi-neutrality holds, since a Debye sphere containing only a fraction of an electron does not provide for efficient screening.

Another important plasma parameter is the plasma frequency. It is the characteristic frequency for the the reaction of a plasma to an external perturbation and its inverse gives a timescale for plasma waves and other collective plasma effects. It is also a lower limit for the frequency of light that is able to pervade the plasma: if it is not well above this limit, the light will be reflected at the plasma boundaries. The electron plasma frequency depends on the electron density and is given by[Hut00]

$$\omega_p = \sqrt{\frac{n_e e^2}{m_e \varepsilon_0}} \tag{2.9}$$

In most cases, the dynamical properties of the plasma are determined by the electron plasma frequency and the ion plasma frequencies are of less importance.

The ionization degree of the plasma depends on the plasma temperature and the free electron density. In general, one must solve a set of rate equations to get the fractions of the various ion species. If a local thermodynamical equilibrium exists, matters simplify significantly. In

		$n_e = 10^{22}\,1/\mathrm{m}^3$ $T_e = 2\,\mathrm{eV}$	$n_e = 10^{22}\,1/\mathrm{m}^3$ $T_e = 10\,\mathrm{eV}$	$n_e = 10^{24}\,1/\mathrm{m}^3$ $T_e = 2\,\mathrm{eV}$	$n_e = 10^{24}\,1/\mathrm{m}^3$ $T_e = 10\,\mathrm{eV}$
ω_p	(1/s)	$5.6 \cdot 10^{12}$	$5.6 \cdot 10^{12}$	$5.6 \cdot 10^{13}$	$5.6 \cdot 10^{13}$
t_p	(ns)	$1.1 \cdot 10^{-3}$	$1.1 \cdot 10^{-3}$	$1.1 \cdot 10^{-4}$	$1.1 \cdot 10^{-4}$
λ_D	(nm)	105.1	235.1	10.5	23.5
N_D		48.7	544.3	4.9	54.4
Z_{eff}		1.05	2.0	0.905	1.89
$\ln\Lambda$		6.03	8.45	3.88	5.56
ν_{ei}	(1/s)	$6.2 \cdot 10^{10}$	$7.2 \cdot 10^{9}$	$4.0 \cdot 10^{12}$	$5.1 \cdot 10^{11}$
σ_{Sp}	$(1/\Omega\mathrm{m})$	$4.5 \cdot 10^{3}$	$3.9 \cdot 10^{4}$	$7.0 \cdot 10^{3}$	$5.5 \cdot 10^{4}$

Table 2.1.: Plasma parameter range typical for our experiment (for measurements of the electron densities and temperatures see [Nef02, Nie02]). The effective charge state and the subsequent quantities are calculated for ammonia.

this case the detailed knowledge of the rate coefficients for the involved processes (ionization or recombination) is no longer necessary. The equilibrium condition is sufficient to derive the Saha equations, which yield the density of the various charge states for a given temperature and free-electron density. The detailed calculation is described in Appendix D. Figure 2.1 shows the composition of an ammonia plasma with a fixed free-electron density of $10^{22}\,\mathrm{m}^{-3}$. The calculation assumes that the ammonia is already fully dissociated. This assumption is fairly safe for temperatures in the electronvolt range, since the dissociation of ammonia starts at 2100 K[Ger85]. The ammonia plasma is a mixture of hydrogen and nitrogen ions; the average charge state of the plasma is therefore dependent on the average charge state of hydrogen and nitrogen. For a free-electron density of $10^{22}\,\mathrm{m}^{-3}$ significant ionization starts at a temperature of roughly 1 eV. At 1.5 eV hydrogen is already fully ionized and nitrogen is singly ionized, yielding an average charge state of 1. For higher temperatures, the charge state of the nitrogen increases, reaching an average of 5 at 10 eV. The total charge state is averaged over the hydrogen and nitrogen charge states, resulting in an average of 2. Due to the large influence of hydrogen, the average charge state of the ammonia plasma increases only slowly from 1 eV to 10 eV.

The transport properties of the plasma channel depend on the total discharge current as well as on the spatial profile of the current density in the channel. The spatial profile depends on the conductivity and the time structure of the discharge current, which can lead to the development of a skin current.

The plasma conductivity depends mainly on the temperature, while the density dependence becomes important only for very low densities. The Spitzer model gives an estimate for the plasma conductivity[Spi56, Spi53, Coh50].

$$\sigma_{\mathrm{Sp}} = \frac{n_e \cdot e^2}{\nu_{ei} \cdot m_e} \tag{2.10}$$

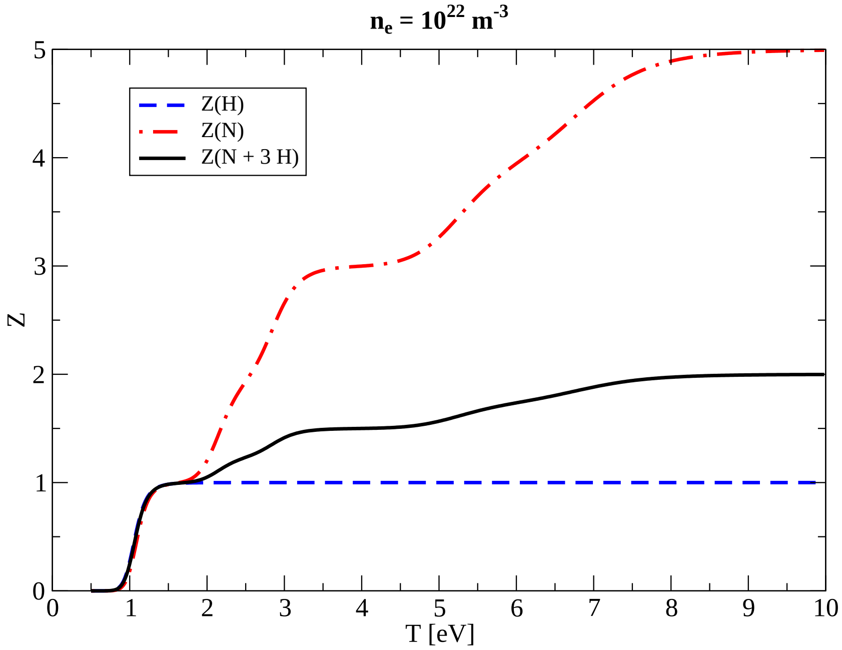

Figure 2.1.: Effective charge states for hydrogen, nitrogen, and the hydrogen-nitrogen mixture. Calculated with the Saha equation (see also Appendix D). The plot shows the temperature dependence for a fixed electron density of $10^{22}\mathrm{m}^{-3}$

The electron-ion collision frequency is given by[Gol98]

$$< \nu_{ei} >= \sqrt{\frac{2}{\pi^3 m_e T_e^3}} \frac{n_e Z e^4 \ln \Lambda}{12 \varepsilon_0^2} \tag{2.11}$$

The Coulomb logarithm

$$\ln \Lambda = \ln(b_{\max}/b_0) \tag{2.12}$$

is determined by the impact parameters $b_{\max}$ (cut-off parameter, determined by Debye shielding) and b_0 (impact parameter for 90° scattering). A possible approximation is[Gol98]

$$b_{\max} = \lambda_D; \qquad b_0 \approx \frac{Z e^2}{12\pi\varepsilon_0 T} \approx \frac{Z}{12\pi n_e \lambda_D^2} \tag{2.13}$$

Z is the effective charge state of the plasma; for a fully ionized plasma it is equal to the nuclear charge. The conductivity is therefore proportional to $T^{3/2}$ and nearly independent of the density, since the Coulomb logarithm depends only weakly on the plasma temperature and density.

Table 2.1 lists the most important plasma parameters, calculated for an ammonia plasma in a parameter range typical for our plasma channels. The electron densities and temperatures in the channel were measured in previous experiments with the old, 50 cm long discharge chamber[Nef02, Nie02]. The calculations for these parameters yield conductivities in the range of $5 \cdot 10^3\, 1/\Omega\mathrm{m}$ and $5 \cdot 10^4\, 1/\Omega\mathrm{m}$ in ammonia. This is in good agreement with older conductivity measurements at a plasma lens, which was operated at similar parameters, but with other gases. These measurements yielded conductivities in the range of 15000/Ωm to 200000/Ωm[Tau93]. These conductivities are significantly lower than those of real conductors. The conductivity of copper, for instance, is roughly $6 \cdot 10^7/\Omega\mathrm{m}$ (room temperature), and thereby more than two orders of magnitude higher than in discharge plasmas.

2.2. The z-pinch

After this discussion of general plasma properties we can now focus on a specific configuration, namely plasma channels, which are also known as z-pinches. All z-pinches are created by discharges, but the methods used to initiate the discharge vary. One common method is to create wire-initiated discharges. In this setup, the electrodes are connected by thin wires. Due to their resistivity, these wires evaporate and create a highly conducting plasma, which guides the discharge. While this method can create channels with currents of several MA , it is limited to single-shot experiments and is therefore not suitable for the final transport in a reactor. In contrast, our setup uses a carbon-dioxide laser to heat the gas along the desired discharge path, creating a rarefaction channel that guides the following discharge. Alternatively, the gas can be ionized with an ion beam prior to the discharge.

2.2.1. Equilibrium

The z-pinch is essentially a one-dimensional configuration, provided that end-effects near the electrodes are insignificant and no instabilities occur. Due to the azimuthal symmetry of the channel, its dynamics are best described in cylindrical coordinates (r (radius), θ (angle), z), where the symmetry axis is identical to the z-axis. The current density is then given by

$$\mathbf{j} = j(r) \cdot \mathbf{e}_z \tag{2.14}$$

The magnetic field is therefore purely azimuthal

$$\mathbf{B} = B(r) \cdot \mathbf{e}_\theta \tag{2.15}$$

The plasma mass density ρ and the plasma pressure p depend only on r and the fluid velocity $\mathbf{v}$ is only radial. The magnetic force equation[Kip75, Gol98, Spa90]

$$\rho \cdot \frac{d\mathbf{v}}{dt} = -\nabla p + \mathbf{j} \times \mathbf{B} \tag{2.16}$$

therefore simplifies to

$$\rho \cdot \frac{dv}{dt} = -\frac{\partial p}{\partial r} - j \cdot B \tag{2.17}$$

In equilibrium, the inertial term on the left-hand side vanishes and the pressure gradient balances the magnetic force:

$$\frac{\partial p}{\partial r} = -j \cdot B \tag{2.18}$$

We will now derive the equilibrium configuration for a channel with a homogeneous current density $j(r) = j$ and channel radius R. In this case, the magnetic field created by a discharge current I is given by

$$B(r) = \begin{cases} \frac{\mu_0 I}{2\pi R^2} r & \text{for} \quad r \leq R \\ \frac{\mu_0 I}{2\pi r} & \text{for} \quad r > R \end{cases} \tag{2.19}$$

so that Equation 2.18 turns into

$$\frac{\partial p}{\partial r} = \begin{cases} -\frac{\mu_0 I^2}{2\pi^2 R^4} r & \text{for} \quad r \leq R \\ 0 & \text{for} \quad r > R \end{cases} \tag{2.20}$$

Taking into account that the pressure vanishes on the boundary ($r = R$), integration yields

$$p(r) = \frac{\mu_0 I^2}{4\pi^2 R^2} \left(1 - \left(\frac{r}{R}\right)^2\right) = p_0 \cdot \left(1 - \left(\frac{r}{R}\right)^2\right) \tag{2.21}$$

inside the channel. So in this equilibrium, the current density inside the channel is constant, the magnetic field is proportional to r, and the gas pressure is proportional to $1 - (r/R)^2$.

2.2.2. Skin effect

Obviously the distribution of the current density inside the channel has a major influence on the channel dynamics and its transport properties for an ion beam. If we consider only a constant discharge current, the current density profile is determined by the conductivity profile. Yet this does not apply to alternating currents. Even if the conductivity is homogeneous inside the plasma column, the *skin effect* can still influence the current density profile. This effect is well-known in normal conductors (for example copper cables). If we impress a high-frequency voltage on the conductor, the self-inductance restricts the current to its surface. If we take Maxwell's equations[Jac98, Sch87] in the quasi-static approximation and assume an ohmic conductor ($\mathbf{j} = \sigma \mathbf{E}$), we get the following differential equation[Pau00]

$$\nabla^2 \mathbf{E} = \sigma \mu_0 \frac{\partial \mathbf{E}}{\partial t} \tag{2.22}$$

Since our channel is (at least approximately) cylindrical, we use cylindrical coordinates with symmetry conditions and we obtain

$$\left(\frac{\partial^2}{\partial r^2} + \frac{1}{r}\frac{\partial}{\partial r}\right) E_z(r,t) = \sigma \mu_0 \frac{\partial}{\partial t} E_z(r,t) \tag{2.23}$$

If we furthermore assume that the field is periodic in time (that is, the applied voltage is periodic in time)

$$E_z(r,t) = E_z(r) \cdot \exp[i\omega t] \tag{2.24}$$

we get

$$\left(\frac{\partial^2}{\partial r^2} + \frac{1}{r}\frac{\partial}{\partial r}\right) E_z(r) = i\omega\sigma\mu_0 E_z(r) \tag{2.25}$$

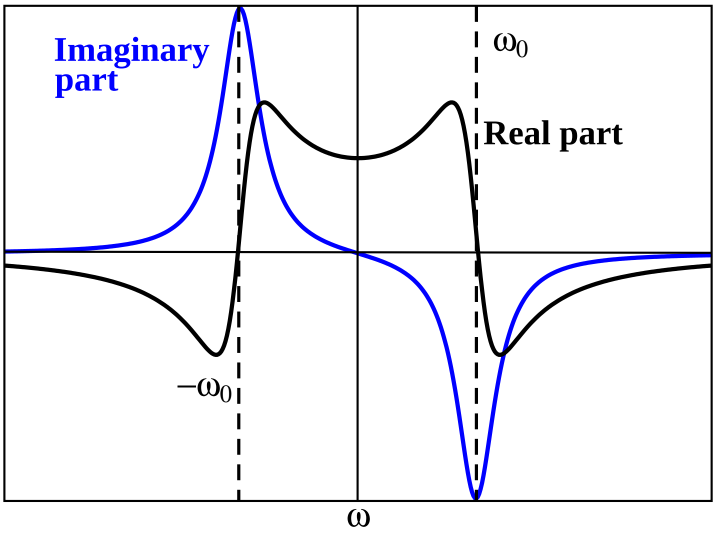

Figure 2.2.: Fourier transform of $f(x) = A \cdot \exp[-a \cdot t] \cdot \sin(\omega_0 \cdot t)$. Plotted are the real and the imaginary part of the transform.

This differential equation has the mathematical form of the diffusion equation. The solution is a Bessel function[Sim71]

$$E_z(r) = C \cdot J_0\left(\sqrt{-i\omega\mu_0\sigma} \cdot r\right) \tag{2.26}$$

The boundary condition is $E_z(R) = E_0$. This determines the constant

$$C = \frac{E_0}{J_0(\sqrt{-i\omega\mu_0\sigma} \cdot R)} \longrightarrow E_z(r) = E_0 \frac{J_0(\sqrt{-i\omega\mu_0\sigma} \cdot r)}{J_0(\sqrt{-i\omega\mu_0\sigma} \cdot R)} = E_0 \cdot \frac{J_0(pr)}{J_0(pR)} \tag{2.27}$$

where $p^2 = -i\omega\mu_0\sigma$. The discharge current is given by $I(t) = I_0 \cdot \exp(i\omega t)$. The electric field and the current density are therefore given by[Sim71]

$$E_z(r,t) = \frac{I_0\, p}{2\pi R\sigma} \frac{J_0(pr)}{J_1(pR)} \cdot \exp(i\omega t) \longrightarrow j_z(r,t) = \frac{I_0\, p}{2\pi R} \frac{J_0(pr)}{J_1(pR)} \cdot \exp(i\omega t) \tag{2.28}$$

This expression can be approximated for the borderline cases of low frequencies ($\omega \rightarrow 0$) and high frequencies ($\omega \rightarrow \infty$). For low frequencies the current density is homogeneous inside the conductor

$$J_z(r,t) \approx \frac{I_0}{\pi R^2} \cdot \exp(i\omega t) \qquad \text{(low frequencies)} \tag{2.29}$$

whereas for high frequencies the current density reduces exponentially from the surface to the center[Sim71], plummeting to $1/e$ of its surface value after one skin depth δ_{sk}. The skin depth is given by

$$\delta_{\mathrm{sk}} = \sqrt{\frac{2}{\omega\mu_0\sigma}} \qquad \text{(high frequencies)} \tag{2.30}$$

The discharge current in our experiment is approximately given by a damped sine, that is

$$I(t)=\begin{cases}A\cdot\exp\left[-a\cdot t\right]\cdot\sin(\omega_o\cdot t) & \text{for} \quad t\geq 0\\ 0 & \text{for} \quad t<0\end{cases} \tag{2.31}$$

where a is a damping factor and ω_0 is roughly given by

$$\omega_0=\frac{2\pi}{T}\approx\frac{2\pi}{24\,\mu\mathrm{s}}=2.6\cdot 10^5\,1/\mathrm{s} \tag{2.32}$$

A Fourier transform yields the frequency spectrum of the current curve. The transform is given by[Cha73]

$$F(\omega)=\frac{A}{2}\left[\left(\frac{\omega_0-\omega}{a^2+(\omega_0-\omega)^2}+\frac{\omega_0+\omega}{a^2+(\omega_0+\omega)^2}\right)+i\left(\frac{a}{a^2+(\omega_0+\omega)^2}-\frac{a}{a^2+(\omega_0-\omega)^2}\right)\right] \tag{2.33}$$

Both the real and imaginary part are sketched in Figure 2.2. Obviously, frequencies above $2\,\omega_0$ have only little impact. Assuming a conductivity of $10^4/\Omega\mathrm{m}$, the skin depth for this frequency is 1.8 cm. The current density in the channel is therefore homogeneous inside the channel, which has diameters which are typically between 1-2 cm.

2.2.3. Pinch dynamics

The dynamics of a z-pinch can be modelled with a one-dimensional magnetohydrodynamical (MHD) simulation. In the following chapter, such a program is used to illustrate the different stages of channel creation and dynamics. For now, we will restrict ourselves to a simpler description, which is less realistic but shows the basic characteristics of pinch dynamics. The model assumes that the current density is homogeneous throughout the whole discharge and describes the evolution of the channel radius. The result is a differential equation

$$\frac{d^2R}{dt^2}=-\frac{\mu_0\cdot I^2}{4\pi N\cdot R}+\frac{4\pi P_0\cdot R_0^{10/3}}{N\cdot R^{7/3}}+\frac{4R}{3\pi N}\int_0^t\frac{I^2(\tau)}{R^4(\tau)\cdot\sigma(\tau)}\,d\tau \tag{2.34}$$

where R is the mass-averaged radius, which for a homogeneous channel is related to the channel radius R_{ch} by

$$R_{\mathrm{ch}}(t)=\sqrt{2}\cdot R(t) \tag{2.35}$$

A derivation of this model is given in Appendix B. The first term is the $\mathbf{j}\times\mathbf{B}$ force, whereas the second and third term are pressure terms, the third term taking ohmic heating into account. Figure 2.3 shows the evolution of the channel radius calculated from the model. All calculations assume that the discharge current is given by

$$I(t)=I_{\max}\cdot\sin\left[2\pi t/T_{\mathrm{dis}}\right] \tag{2.36}$$

with a period length of 20 µs. They assume a constant conductivity of $10^5\,1/\Omega\mathrm{m}$ and an initial temperature of 1000 K. The calculations show the effect of the initial gas density and the

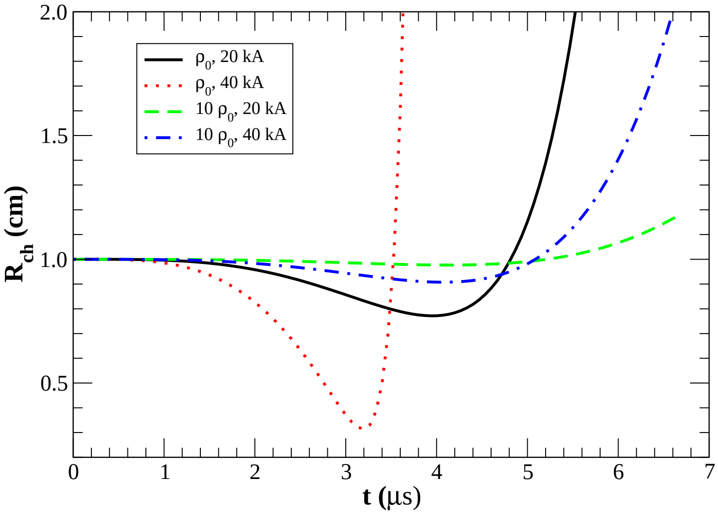

Figure 2.3.: Channel evolution calculated with the model. The calculation assumes a constant conductivity of $10^5/\Omega\mathrm{m}$. $\rho_0 = 0.00526\,\mathrm{kg/m^3}$, corresponding to 1 mbar xenon at room temperature.

discharge current on the pinching. Since the model does not include radiation losses, the expansion after the pinching is much too fast. In reality, the radiation losses are proportional to T^4, thereby limiting the maximum temperature. In addition, the conductivity increases with rising temperature, so that the heating of the channel reduces. In addition, the ambient gas slows down the channel expansion.

2.2.4. Pinch instabilities

The suppression of channel instabilities is crucial for the feasibility of the transport concept. To study the stability of the channel against instabilities, one has to start with a channel in equilibrium. The slow widening of the channel in our experiment is therefore neglected. Gradients in the current density and the pressure drive the development of instabilities. Depending on the conductivity of the plasma, there are two kinds of instabilities: *ideal instabilities* and *resistive instabilities*. Ideal instabilities develop if the electric resistivity is negligible. In this case, the magnetic field lines are ‘frozen’ in the fluid and instabilities do not change the topology of the magnetic field. In the resistive case, the topology of the field can change, since tearing and reconnection of field lines is possible. Due to the high conductivity of the plasma channel (see Table 2.1, resistive instabilities are less important than magnetohydrodynamical instabilities and are therefore neglected.

To analyze the development of instabilities, we start from a pinch equilibrium

$$\nabla p_0 = \mathbf{j}_0 \times \mathbf{B}_0 = \frac{1}{\mu_0}(\nabla \times \mathbf{B}_0) \times \mathbf{B}_0 \tag{2.37}$$

and study the evolution of small perturbations. The physical properties are described as the sum of the equilibrium value and the perturbation:

$$\mathbf{v} = \mathbf{v}_0 + \mathbf{u} = \mathbf{u} \tag{2.38}$$

$$\mathbf{B} = \mathbf{B}_0 + \tilde{\mathbf{B}} \tag{2.39}$$

$$p = p_0 + \tilde{p} \tag{2.40}$$

$$\rho = \rho_0 + \tilde{\rho} \tag{2.41}$$

Inserting this in the MHD force equations yields in linear approximation [Spa90]

$$\rho_0 \cdot \frac{\partial \mathbf{u}}{\partial t} = -\nabla \tilde{p} + \frac{1}{\mu_0}\left[(\nabla \times \mathbf{B}_0) \times \tilde{\mathbf{B}} + (\nabla \times \tilde{\mathbf{B}}) \times \mathbf{B}_0\right] \tag{2.42}$$

Assuming an adiabatic equation of state

$$\frac{d}{dt}\left(\frac{p}{\rho^\gamma}\right) = 0 \tag{2.43}$$

and setting $\dot{\boldsymbol{\xi}} = \mathbf{u}$, we obtain a differential equation for the perturbation[Man73, Spa90]

$$\rho_0 \ddot{\boldsymbol{\xi}} = \nabla(\boldsymbol{\xi} \cdot \nabla p_0 + \gamma p_0 \nabla \cdot \boldsymbol{\xi}) + \frac{1}{\mu_0}[\nabla \times [\nabla \times (\boldsymbol{\xi} \times \mathbf{B}_0)]] \times \mathbf{B}_0 + \frac{1}{\mu_0}(\nabla \times \mathbf{B}_0) \times [\nabla \times (\boldsymbol{\xi} \times \mathbf{B}_0)] \tag{2.44}$$

A Fourier analysis is used to study the dynamics of the instability. The common ansatz is

$$\xi \propto \exp\left[\Gamma \cdot t + i\,(kz + m\,\theta)\right] \tag{2.45}$$

where Γ is the growth rate of the instability, k is the wave-vector, and θ the angle in cylindrical coordinates. The qualitative behavior of the instability is determined by the parameter m, which is an integer number. For $m = 0$, the perturbation is cylindrically symmetric and results in a variation of the channel diameter along the axis. This instability is called *sausage instability*. For $m = 1$, the *kink instability* has the shape of a helix. Instabilities with larger values of m are suppressed in typical conditions[Fre82].

Figure 2.4 illustrates the physical mechanism of both instabilities. If we assume a stable, time-independent channel, the magnetic pressure, which is proportional to B_θ^2, and the gas pressure compensate each other at the surface.

The sausage instability starts with a local reduction in the channel radius. This reduction in the channel diameter leads to an increased current density and therefore an increased magnetic field. If the current density is concentrated on the surface of the channel, there is no magnetic pressure inside the channel. The magnetic pressure then ‘squeezes’ the gas out of the constriction, along the channel axis. This leads to an ever decreasing radius and finally the disruption of the channel. If, on the other hand, the current density is distributed homogeneously inside the channel, the instability is suppressed, since the increase in magnetic pressure is much smaller than in the previous case. The sausage instability is therefore no danger in our setup. Since the sausage instability is driven by pressure gradients, a sufficiently gradual pressure profile stabilizes the channel against this instability[Fre82].

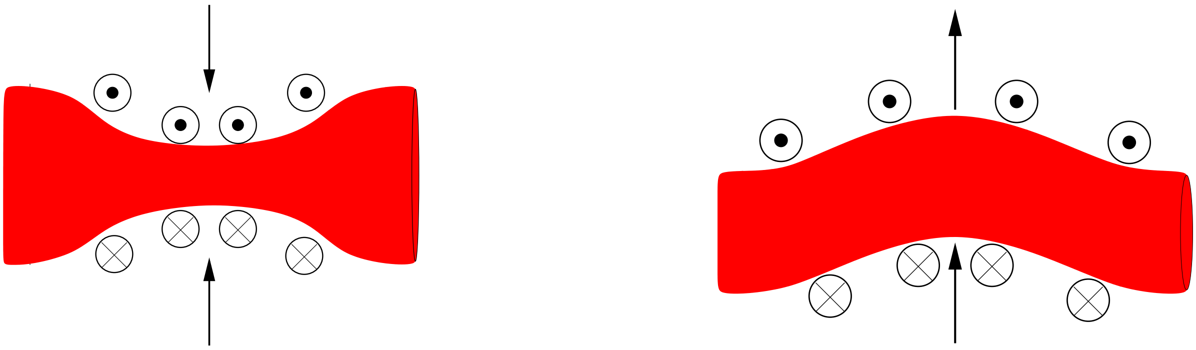

Figure 2.4.: Schematics for the sausage instability (left picture) and the kink instability (right picture). The pictures show the plasma channel and the magnetic field. The movement of the plasma boundary is indicated with arrows.

The kink instability is far more dangerous in our experimental setup. This instability starts with a small local displacement of the channel, as indicated in Figure 2.4. This leads to an increase of magnetic pressure at the inner side of the bend and to a decrease at the outer boundary, which amplifies the bend. In the worst case the kink instability leads to a 'twisting'of the channel, resulting in a helix-like structure. Several factors influence the growth rate of the instability. First of all, the surroundings have a major influence. If the channel is surrounded by a solid wall, like in wall-stabilized discharges, the wall blocks the movement of the channel, thereby preventing kink instabilities. Similarly, the instability develops much faster if the pinch is surrounded by low pressure gas than in gas of a higher pressure, since the channel has to 'shift' the ambient gas during its movement. The gas density inside the channel influences the instability growth, since its inertia hinders the motion of the channel.

The growth rate of the kink instability can be calculated for an idealized setup[Man73]. The calculation considers three regions: the core of the pinch, a corona of negligible width, and the surrounding gas. For the sake of simplicity, the model assumes that all current flows in the corona, and that the core has a homogeneous density ρ_p and infinite conductivity. The density of the corona is ρ_c and the density of the surrounding gas is ρ_g. The temperatures are T_p, T_c, and T_g, respectively. Since the current only flows in the corona, the magnetic field in equilibrium is

$$B_\theta(r) = \begin{cases} \frac{B_0 r_p}{r} & \text{for} \quad r \geq r_p \\ 0 & \text{for} \quad r < r_p \end{cases} \tag{2.46}$$

If the pinch is surrounded by vacuum, the growth rate of the instability is[Man73]

$$\Gamma = k v_{\mathrm{Ap}} \left[-\ln(0.5 \cdot k r_p) - \gamma_E \right] \tag{2.47}$$

where $\gamma_E \approx 0.5772$ is Euler's constant and the Alfvén velocity in the pinch is given by

$$v_{\mathrm{Ap}} = \frac{B_0}{\sqrt{\mu_0 \rho_p}} \tag{2.48}$$

If the pinch is surrounded by gas, the growth rate is altered. The rate depends on the parameter

A, which is given by

$$A = k^2 r_p^2 \left(\frac{T_p \rho_p^2}{T_g \rho_g^2} \right) [-\ln(0.5 k r_p) - \gamma_E] \tag{2.49}$$

For $A \gg 1$, the growth rate is unaltered. If $1 \gg A \gg \rho_p/\rho_g$, the growth rate changes to[Man73]

$$\Gamma_2 \approx k r_p \left(\frac{T_p^{1/2} \rho_p}{T_g^{1/2} \rho_g} \right) k v_{\mathrm{Ap}} [-\ln(0.5 k r_p) - \gamma_E] \tag{2.50}$$

If $\rho_p/\rho_g \gg A$, the growth rate is given by[Man73]

$$\Gamma_3 \approx \left(\frac{\rho_p}{\rho_g} \right)^{1/2} k v_{\mathrm{Ap}} [-\ln(0.5 k r_p) - \gamma_E]^{1/2} \tag{2.51}$$

In a typical discharge, the density is 10-fold reduced, so that $\rho_p/\rho_g = 1/10$. The ambient gas temperature is $T_g = 300\,\mathrm{K}$. Furthermore, we assume a plasma temperature of $T_p = 30000\,K$, and a pinch radius of $r_p = 0.5\,\mathrm{cm}$. A look at the growth rate given in Equation 2.47 shows that the sign of the rate Γ depends on the wavelength of the perturbation. For the set of parameters given above, the growth rate becomes positive only for perturbation wavelengths longer than 2.8 cm. Hence instabilities do not develop for shorter wavelengths.

For a quick estimate of the growth rate, let us assume that the channel carries a current of 50 kA. The magnetic field B_0 at the channel boundary is then $2\,\mathrm{Vs/m^2}$. For a channel density of $7 \cdot 10^{-4}\,\mathrm{kg/m^3}$ (equivalent to 1 mbar ammonia), the Alfvén velocity is $7 \cdot 10^4\,\mathrm{m/s}$. If we, for the moment, consider a pinch in vacuum (Equation 2.47), the maximum growth rate is reached for a wavelength of 7.6 cm. The growth rate for this wavelength is $3 \cdot 10^4$/s, so that an initial perturbation would increase by a factor of $\exp[\Gamma \cdot 10\,\mu\mathrm{s}] = 1.35$ in the first 10 µs. In the next step, we take into account the stabilization by the gas blanket, so Equation 2.51 must be used to calculate the growth rate. Using identical channel parameters as above, the maximum instability growth is then predicted for a wavelength of 4.6 cm with a growth rate of only 3370/s. After 10 µs, an initial perturbation would be increased by a factor of only 1.03. So in this scenario no instabilities occur due to the damping by the gas blanket.

According to the model, the channel should be stable for typical operating conditions. Unfortunately, these results are only a guideline for our setup, since the model makes two approximations which are not fulfilled in our experiment. The first point is that our channel is not in equilibrium, but expands. Secondly, the model assumes that all current flows on the surface, whereas in our case the current density is (roughly) homogeneous inside the channel. Because of these differences, the results should be interpreted qualitatively as indicating the stabilization by the gas blanket, but the calculated growth rates are not directly applicable to our experiment.

2.3. Ion beam transport

Now that we have dealt with the basic processes that determine the dynamics of the z-pinch, we focus our attention on the dynamics of the beam ions in these channels. Starting with the study of the low-current beams supplied by the UNILAC accelerator, we will move on to the (theoretical) study of high-current beams.

2.3.1. Basic beam properties

First of all, we must specify the basic properties of ion beams. Basically, an ion beam is a collection of co-moving ions. In an (hypothetical) ideal ion beam, all the ions have the same velocity, that is, all velocity components perpendicular to the direction of motion vanish. If we identify the direction of motion with the z axis, the velocity of all ions is given by $\mathbf{v} = \beta\, c\, \mathbf{e}_\mathrm{z}$. The phase-space volume occupied by such a beam would be zero. In reality, no such beam exists. A real beam has a velocity spread in the direction of movement and in addition velocity components perpendicular to it. There are many reasons for this velocity spread. To begin with, the ion sources usually extract the ions from a plasma. Due to the temperature of the plasma, the ions already have thermal velocities before their extraction. The extracting voltage increases the velocity in the z-direction, but leaves the other velocity components unchanged.

The quality of the beam can be quantified by studying the six-dimensional phase-space volume occupied by the beam. If we can neglect the interaction between the particles we can study the different parts ((x, v_x), (y, v_y), (z, v_z)) separately. If the effect of collisions between beam particles is negligible, Liouville's theorem ensures the conservation of phase-space volume. Nevertheless, non-linear effects increase the *effective* phase-space volume. Therefore another figure of merit is needed to describe the beam quality. If beam acceleration can be neglected, the *emittance* is such a figure of merit (otherwise, a 'normalized' emittance can be used). To determine the emittance we plot the beam in *trace-space*, that is $(x, dx/dz)$. The emittance is the area of the smallest ellipse containing the beam particles, divided by π[Hum90] and has the unit $\pi - \mathrm{mm} - \mathrm{mrad}$. This definition is not suitable for beam measurements, since real beams have no sharp boundary, and are often surrounded by a halo of small ion density. A better figure of merit is therefore the *rms-emittance*, which is defined as[Lej80, Law73]

$$\varepsilon_\mathrm{rms} = 4\left[\left\langle (x - \langle x\rangle)^2 \right\rangle \cdot \left\langle \left(x' - \langle x'\rangle\right)^2 \right\rangle - \left\langle (x - \langle x\rangle) \cdot \left(x' - \langle x'\rangle\right) \right\rangle^2 \right]^{1/2} \tag{2.52}$$

The $\langle\rangle$ braces denote the ensemble average and $x' = dx/dz$ is the angle with the z axis. This definition of the emittance refers to the covariance ellipse of the data set[Bra99]. The rms-emittance can be increased by non-linearities in the focusing optics of the beam transport system. A typical value for the emittance of a UNILAC beam is $5\,\pi - \mathrm{mm} - \mathrm{mrad}$.

2.3.2. Energy loss of the ion beam

The energy loss of the ions depends on the channel density, the charge state of the ions and their velocity. While passing a gas, the ions lose energy due to collisions with gas atoms. The kinetic energy lost by the ions is converted to an excitation of the target atom, whereas the kinetic energy of the gas atom is negligible. If one neglects correction terms for highly

Gas	p (mbar)	n ($1/\mathrm{cm}^3$)	dE/dx (keV/mm)	Range (m)	I (eV)	N_e
NH_3	1	$2.4 \cdot 10^{16}$	8.98	251.7	13.6	$6.6 \cdot 10^5$
Ne	1	$2.4 \cdot 10^{16}$	7.45	340.4	21.6	$3.5 \cdot 10^5$
Ar	1	$2.4 \cdot 10^{16}$	11.75	208.2	15.8	$7.5 \cdot 10^5$
Kr	1	$2.4 \cdot 10^{16}$	20.9	132.0	14.0	$1.5 \cdot 10^6$
Xe	1	$2.4 \cdot 10^{16}$	28.6	96.2	12.1	$2.4 \cdot 10^6$

Table 2.2.: Energy loss of a bismuth beam in various gases (calculations with SRIM[Zie85]). The beam ions have a kinetic energy of 11.4 MeV/u, resulting in a total ion energy of 2.38 GeV. I is the first ionization energy of the gas and N_e is the upper limit of the number of electrons that can be freed by one ion per traversed meter.

relativistic beams, the stopping power in a gas is given by the Bethe-Bloch formula[Ahl80]

$$\frac{dE}{dx} = -\left(\frac{Z_{\mathrm{eff}} \cdot e \cdot \omega_p}{\beta \cdot c}\right)^2 \cdot \ln\left(\frac{2 m_e (\beta \cdot c)^2}{I_{\mathrm{pot}}}\right) \tag{2.53}$$

where Z_{eff} is the effective charge state, e the electron charge, m_e its mass, and $\beta \cdot c$ the velocity of the beam. The ‘plasma’ frequency is given by

$$\omega_p^2 = \frac{n \cdot Z e^2}{\varepsilon_0 \cdot m_e} \tag{2.54}$$

where n is the gas density and Z the atomic number of the gas. The characteristic absorption properties of a gas enter in the mean excitation potential per electron, which can be calculated from oscillator strengths and energies of the excitation modes[Ahl80].

The stopping power of a plasma differs from that of a cold gas, since the free electrons change the effective charge state of the ions and the Coulomb logarithm. The differences in the stopping power become most pronounced for low ion energies (1-2 MeV/u), but are small for high ion energies[Hof90, Nar82].

An accurate knowledge of the ion charge state is essential, since the stopping power scales with the square of the effective charge state of the ions. For ions in a cold gas and also for energetic ions in plasma, the effective charge state can be calculated with the Betz formula[Wit73, Bet72]

$$Z_{\mathrm{eff}}(\beta) = Z_{\mathrm{ion}}\left(1 - \exp\left[-0.555\left(\frac{137\,\beta\,c}{Z_{\mathrm{ion}}^{0.517}}\right)^{1.175}\right]\right) \tag{2.55}$$

The calculation of the stopping power requires an accurate knowledge of the average ionization potential of the medium. The SRIM code[Zie85] combines theoretical models with experimental data, resulting in very accurate stopping power calculations. The energy loss in various gases over a distance of 1 m was calculated at 1 mbar, the results are summarized in Table 2.2. The calculations were done for a bismuth beam with 11.4 MeV/u, which was used during a beamtime. The stopping power is approximately proportional to the target density, so that the energy loss can be easily derived for other densities. Since the ion beam can also be used to initiate the discharge channel (see Section 3.3.3), an upper limit of the free electrons created by one ion is also estimated. This upper limit is equal to the ratio of the energy loss of the beam ion and the minimum ionization energy of the chamber gas. These calculations indicate that the ion beam can be used efficiently to guide the discharge, as verified by the discharge experiments.

2.3.3. Beam transport

The modelling of beam transport in a plasma channel is a complex task, since three different interactions must be modelled simultaneously and self-consistently: the action of the channel on the beam ions, the interaction between the beam ions, and the action of the beam ions on the channel. Fortunately, matters simplify significantly for low current beams. In this case, the interaction between the individual beam particles as well as the action of the beam on the channel can be neglected, so that the beam transport can be calculated by considering single ions moving in an external magnetic field. This treatment is well suited for the ion beams created in the UNILAC, but of course not applicable to the high-current beams required for a heavy-ion fusion reactor.

2.3.4. Betatron oscillations

The dynamics of low-current heavy-ion beams in the plasma channels follows betatron oscillations, which are derived in the following. We assume that the channel is cylindrically symmetric and neglect end effects at the electrodes. In this case, the magnetic field of the channel depends only on the distance to the symmetry axis. Cylindrical coordinates $(r,\ \theta,\ z)$ are ideally suited for this problem. The magnetic field is given by

$$\mathbf{B} = B_\theta(r)\,\mathbf{e}_\theta \tag{2.56}$$

The position vector is given by

$$\mathbf{r} = r\cdot\mathbf{e}_r + z\cdot\mathbf{e}_z. \tag{2.57}$$

Correspondingly, the velocity is

$$\mathbf{v} = \frac{d}{dt}\mathbf{r} = \dot{r}\cdot\mathbf{e}_r + r\cdot\dot{\theta}\cdot\mathbf{e}_\theta + \dot{z}\cdot\mathbf{e}_z \tag{2.58}$$

and the acceleration is

$$\ddot{\mathbf{r}} = \dot{\mathbf{v}} = \left[\ddot{r} - r\,\dot{\theta}^2\right]\mathbf{e}_r + \left[r\,\ddot{\theta} + 2\dot{r}\,\dot{\theta}\right]\,\mathbf{e}_\theta + \ddot{z}\,\mathbf{e}_z. \tag{2.59}$$

Inserting this in the equation of motion

$$m\,\ddot{\mathbf{r}} = q\,(\dot{\mathbf{r}}\times\mathbf{B}) \tag{2.60}$$

yields three coupled differential equations

$$\begin{aligned} m\cdot\left[\ddot{r} - r\cdot\dot{\theta}^2\right] &= -\dot{z}qB(r) \\ r\,\ddot{\theta} + 2\dot{r}\,\dot{\theta} &= 0 \\ m\ddot{z} &= qB(r)\,\dot{r} \end{aligned} \tag{2.61}$$

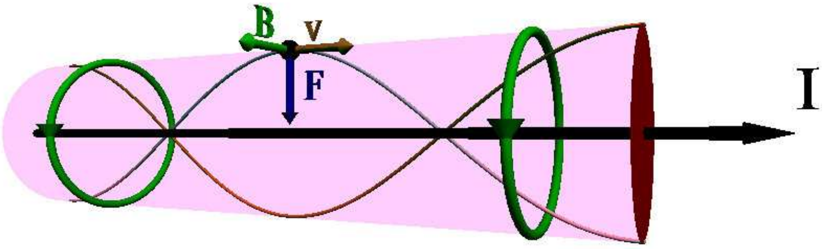

Figure 2.5.: The principle of channel transport: The discharge creates a large azimuthal magnetic field, which forces the beam particles to perform betatron oscillations.

This result can be further simplified with some basic assumptions. In general, the azimuthal velocity $\dot{\theta} \cdot r$ is much smaller than the average beam velocity $\dot{z}$. We can hence neglect it and set θ constant, thereby eliminating the second differential equation. Furthermore, the relativistic ion beam has a velocity of $0.15c$ and we can therefore neglect the change in the axial velocity ($\ddot{z} \approx 0$). So the problem reduces to one differential equation for the radius, with $\dot{z} = v_z$ assumed to be constant:

$$m\ddot{r} = -v_z q B(r) \tag{2.62}$$

If we furthermore assume a spatially homogeneous current density inside the channel, the magnetic field is given by

$$B(r) = \begin{cases} \frac{\mu_0 I}{2\pi R^2} \cdot r & \text{for} \quad r \leq R \\ \frac{\mu_0 I}{2\pi} \cdot \frac{1}{r} & \text{for} \quad r > R \end{cases} \tag{2.63}$$

and the equation of motion inside the channel is

$$m\ddot{r} = -q v_z \frac{\mu_0 I}{2\pi R^2} r \tag{2.64}$$

The solution of this differential equation is of the form $r(t)$. Since we are interested in the trajectory of the particle in the channel, we have to transform the differential equation. Substituting $\ddot{r} = v_z^2 (d^2 r/dz^2)$ eliminates the time derivatives:

$$\frac{d^2 r}{dz^2} + \frac{q \mu_0 I}{2\pi m v_z R^2} r = 0 \tag{2.65}$$

The solutions $r(z)$ of this differential equation are cosine and sine betatron oscillations. The wavelength for these oscillations is the betatron wavelength

$$\lambda_{\mathrm{Bet}} = 2\pi / \sqrt{\frac{q \mu_0 I}{2\pi m v_z R^2}} \tag{2.66}$$

The betatron motion is shown in figure 2.5. The magnetic field of the channel exerts a Lorentz force on the particle which pulls it towards the channel axis and prevents it from leaving the channel.

2.3.5. Ray-tracing calculations

The analytical treatment described above gives useful insight in the transport principle, and yields the betatron wavelength as the scaling length for the beam transport. Yet the particle dynamics in non-uniform channels cannot be described with this analytical model. In addition, the model does not take emittance effects into account. Provided that space-charge effects are negligible, a more realistic calculation is possible with a simple computer program. For the sake of simplicity, the calculation assumes that the current density depends only on the distance from the axis, so that the magnetic field is purely azimuthal. The program starts by generating a Gaussian particle ensemble of given beam width and emittance with a random-number generator. In the next step, the particles that pass the initial pepperpot mask (see for example Figure 2.6) are identified. Finally, the trajectory for each of these particles is calculated for specified channel parameters, yielding the shape of the beam and phase-space plots for arbitrary positions along the channel axis. The calculation takes the full Lorentz force into account, avoiding the simplifications of Equation 2.61. It is important to note that these calculations are not limited to homogeneous channels, but can be applied to arbitrary current density profiles, provided they are radially symmetric. In the following, the transport properties are calculated for two cases: the ideal transport in the channel, and the transport in a channel that is smaller than the ion beam, leading to distortions of the ion beam during transport. For each stage of the transport, both the shape of the beam (the ‘scintillator’ images) and the corresponding phase-space plot are presented. Apart from statistical effects, the phase-space projections for the y and the x component are identical, so only the latter are shown.

Matched channel

The results for an ion beam in a homogeneous channel are shown in Figures 2.6 and 2.7. The channel has a total current of 50 kA and a diameter of 2 cm. The simulated beam consists of gold ions (nuclear charge 79) with a mass of 197 u and a kinetic energy of 11.4 MeV/u. The average charge state (estimated with the Betz formula) of this ions is 59.7. The analytic model yields a betatron wavelength λ_{bet} of 79.4 cm for this set of parameters.

The calculation starts with $50,000$ particles of which roughly $2,400$ pass the pepperpot mask. The standard deviation for the beam positions is set to 5 mm and the emittance to $5\,\pi$ mm-mrad. The beam shape directly after passing the pepperpot mask is depicted in Figure 2.6a. The phase-space plot (Figure 2.6d) shows that the beam velocities still follow a Maxwellian distribution, since the velocities are distributed symmetrically around $v_x = 0$. Figures 2.6b and 2.6e show the beam $1/8$ betatron length after the pepperpot mask. The beam is already slightly ‘compressed’ and converging towards the beam axis. The converging angle is indicated by the negative tilt of the particle distribution in phase-space. After one quarter of a betatron length, the beam has reached its first focal point, resulting in a drastically reduced beam size and an upright particle distribution in phase-space (see Figures 2.6f and 2.6e). After the first focal point the beam is inverted and diverging (Figures 2.7a and 2.7d). After half a betatron length, the beam has reached its original size but is still inverted (see Figures 2.7b and 2.7e). Finally, after one betatron length, the beam has reached its original shape and velocity distribution without any distortions (see Figures 2.7c and 2.7f). The simulations show that

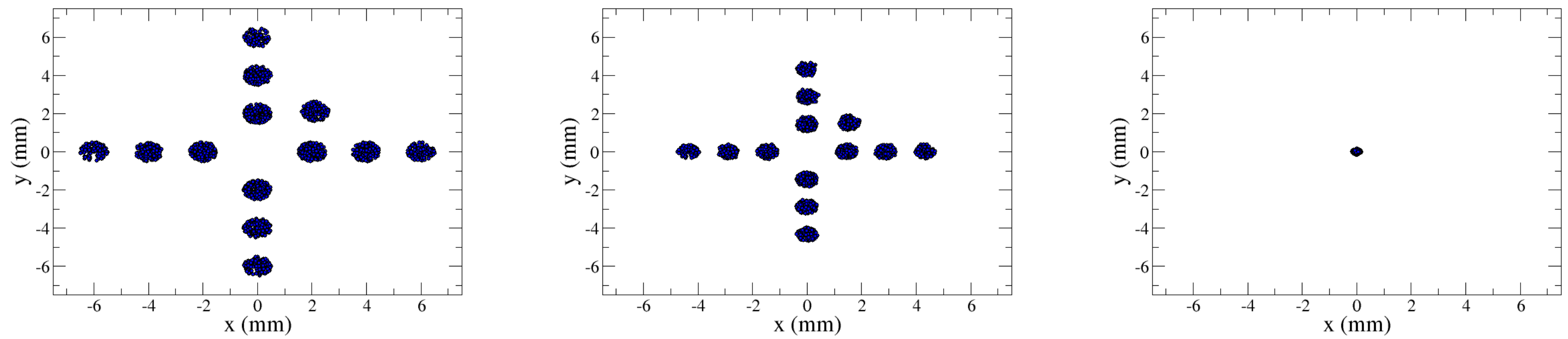

(a) Scintillator: Behind the mask

(b) Scintillator: At $\lambda_{\mathrm{bet}}/8$

(c) Scintillator: At $\lambda_{\mathrm{bet}}/4$ (first focus)

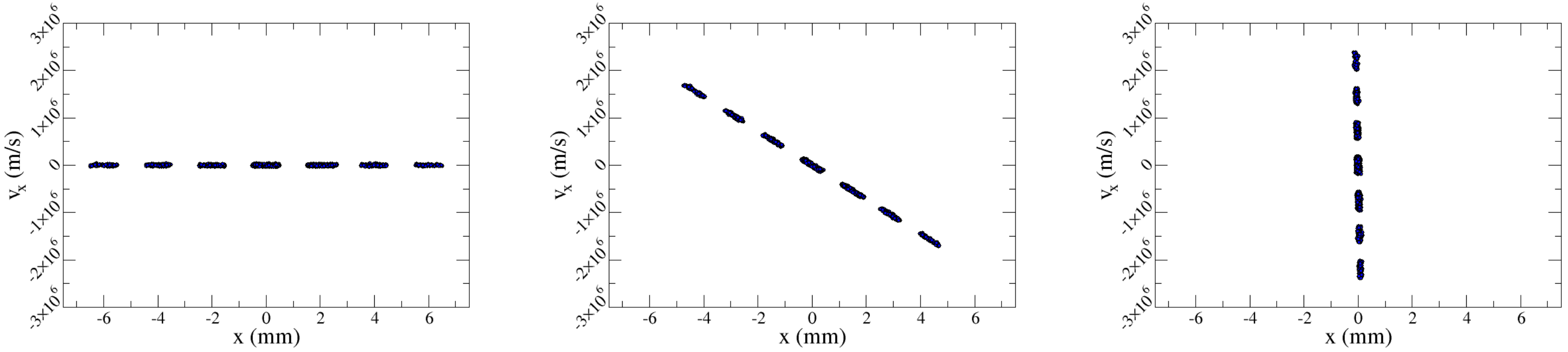

(d) Phase space: Behind the mask

(e) Phase space: At $\lambda_{\mathrm{bet}}/8$

(f) Phase space: At $\lambda_{\mathrm{bet}}/4$ (first focus)

Figure 2.6.: Calculated beam transport in a homogeneous plasma channel. The initial ${}^{197}_{79}$Au beam has a kinetic energy of 11.4 MeV/u and an emittance of 5π mm-mrad. The plots show the beam directly after the pepperpot mask ($z = 0$), at $z = \lambda_{\mathrm{bet}}/8$, and at $z = \lambda_{\mathrm{bet}}/4$

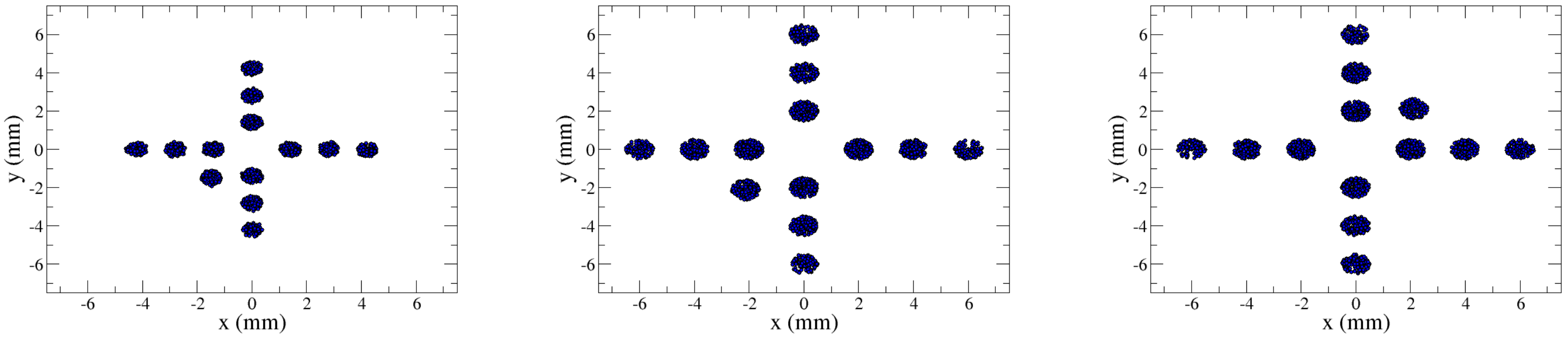

(a) Scintillator: At $3/8\,\lambda_{\text{bet}}$

(b) Scintillator: At $1/2\,\lambda_{\text{bet}}$

(c) Scintillator: After one betatron length

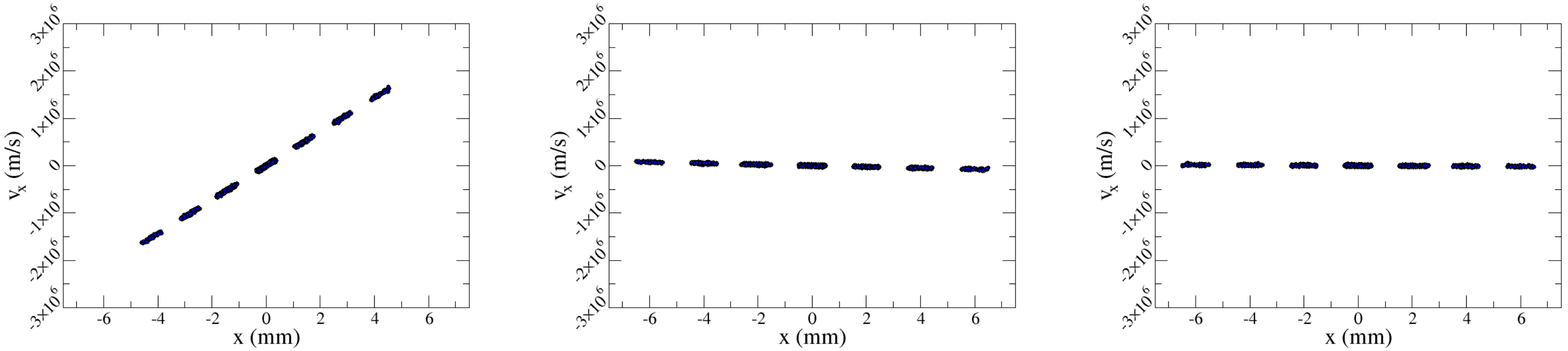

(d) Phase space: At $3/8\,\lambda_{\text{bet}}$

(e) Phase space: At $1/2\,\lambda_{\text{bet}}$

(f) Phase space: After one betatron length

Figure 2.7.: Calculated beam transport in a homogeneous plasma channel. The initial $^{197}_{79}$Au beam has a kinetic energy of 11.4 MeV/u and an emittance of 5π mm-mrad. The plots show the beam directly at $z = 3\,\lambda_{\text{bet}}/8$, at $z = \lambda_{\text{bet}}/2$ and at $z = \lambda_{\text{bet}}$

the transport in an ‘ideal’channel does not distort the ion beam and therefore preserves the beam emittance. In reality, several effects can increase the beam emittance, for example collisions of the beam particles with the plasma particles or non-linearities in the magnetic field of the channel. Yet more sophisticated beam transport simulations[Ros04, Wel02] and first experimental measurements[Kno04] indicate the emittance increase is small (the measurements indicate that the emittance increase is at most 50%).

Mismatched channel

The situation changes considerably if the channel is smaller in diameter than the ion beam (henceforth these channels are called ‘mismatched channels’). This is a special case of the usual ‘mismatching’ of a beam in accelerator physics, which refers to cases when the beam emittance is larger than the acceptance of the accelerator segment, resulting in a loss of a part of the beam. In our experiment, this situation can arise at the beginning of the discharge. Depending on the discharge conditions, the channel diameter can be smaller than 1 cm at this early stage. To study the consequences of this mismatch, the beam transport was calculated for the same set of parameters as before, with the exception of the channel diameter, which was set to half the beam diameter, that is 0.6 cm. The beam particles can now be divided into two sets: particles starting outside the channel (‘outer particles’), and particles starting inside the channel (‘inner particles’). The dynamics of the inner particles is described by betatron oscillations, but the smaller channel diameter results in a reduced betatron wavelength (24 cm). The outer particles also oscillate around the axis, but these oscillations are no longer described by cosine functions, since the magnetic field outside the channel is proportional to $1/r$.

The results of the calculations are shown in Figure 2.8 and 2.9. Naturally, the initial beam configuration is identical to the previous calculation (see Figure 2.8a and 2.8d). In the following, the betatron phases refer to the inner particles. After $1/8$ betatron wavelength, deviations from the ideal transport are already visible (Figures 2.8b and 2.8e). While the inner particles are partly focused, the outer particles converge more slowly, resulting in a lower transversal velocity. When the inner particles reach the first focus, the outer particles are still trailing behind (Figures 2.8c and 2.8f), so that no focus is reached. The beam reaches its minimum size after the first focus. After $3/8$ betatron lengths (Figures 2.9a and 2.9d), the beam is inverted and the image is slightly distorted. While most of the particles are diverging, some of the outer particles are still converging. After half a betatron length (Figures 2.9b and 2.9e), the inner particles are inverted and move parallel to the axis, while the outer particles are still diverging, resulting in a reduced size of the cross. After one betatron wavelength (Figures 2.9c and 2.9f), the ion beam has returned to its original size, but some of the outer particles are converging while some others are still diverging, resulting in a distorted beam. The non-linearity of the channel has also left its ‘footprint’ in the phase-space diagram, where a spiralling of the distribution is clearly visible. These calculations demonstrate that it is necessary to match the channel radius to the beam size, as a too small channel leads to a significant increase of the beam emittance.

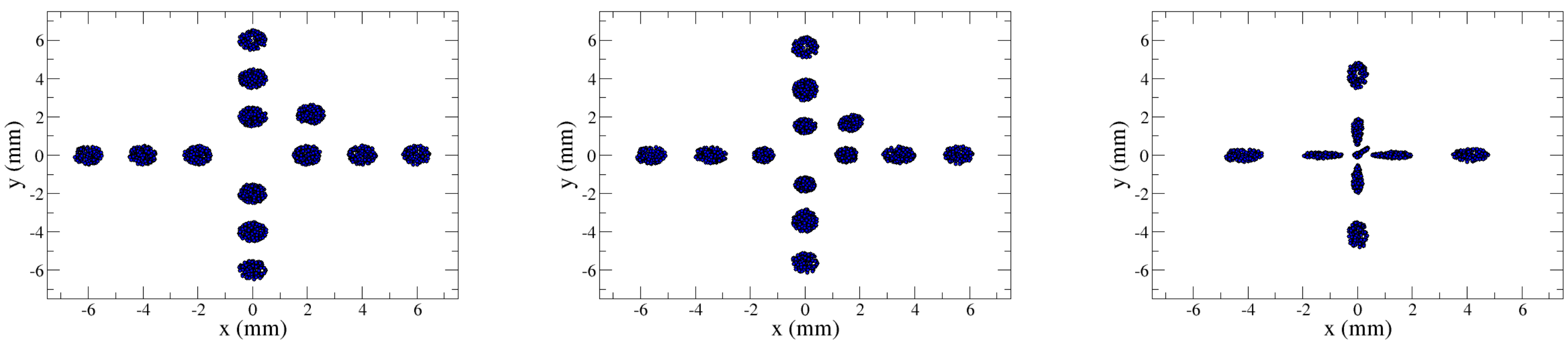

(a) Scintillator: Behind the mask (b) Scintillator: At $1/8\,\lambda_{\mathrm{bet}}$ (c) Scintillator: At $1/4\,\lambda_{\mathrm{bet}}$ (first focus)

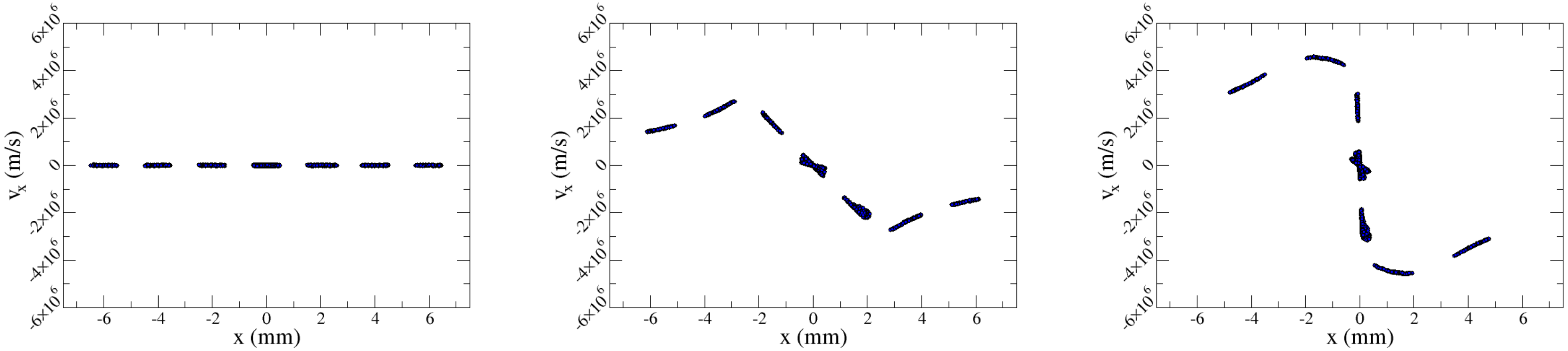

(d) Phase space: Behind the mask (e) Phase space: At $1/8\,\lambda_{\mathrm{bet}}$ (f) Phase space: At $1/4\,\lambda_{\mathrm{bet}}$

Figure 2.8.: Transport in a mismatched channel. Calculations for a 50 kA discharge in a 6 mm diameter channel. The betatron wavelength refers to the particles that oscillate inside the channel.

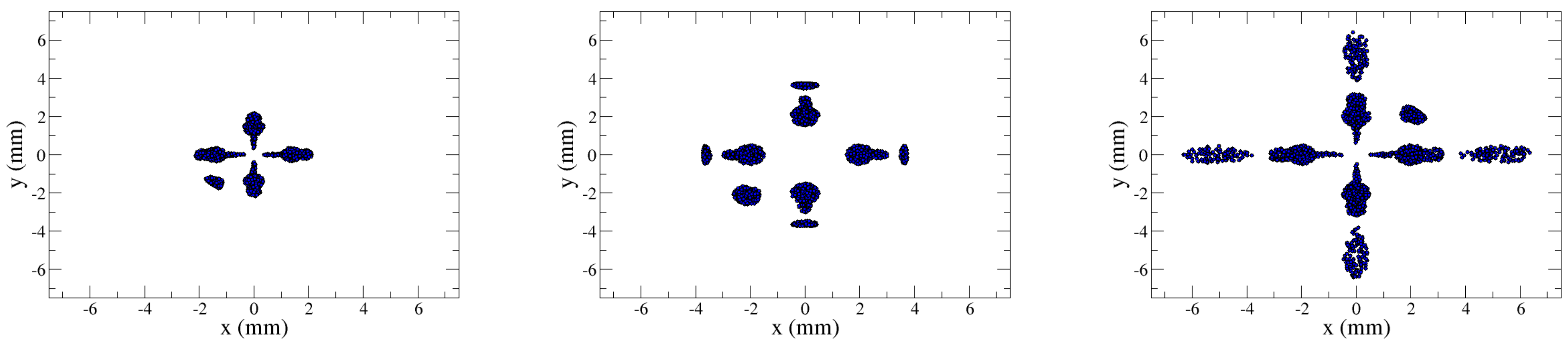

(a) Scintillator: At $3/8\,\lambda_{\mathrm{bet}}$

(b) Scintillator: At $1/2\,\lambda_{\mathrm{bet}}$

(c) Scintillator: After one betatron wavelength

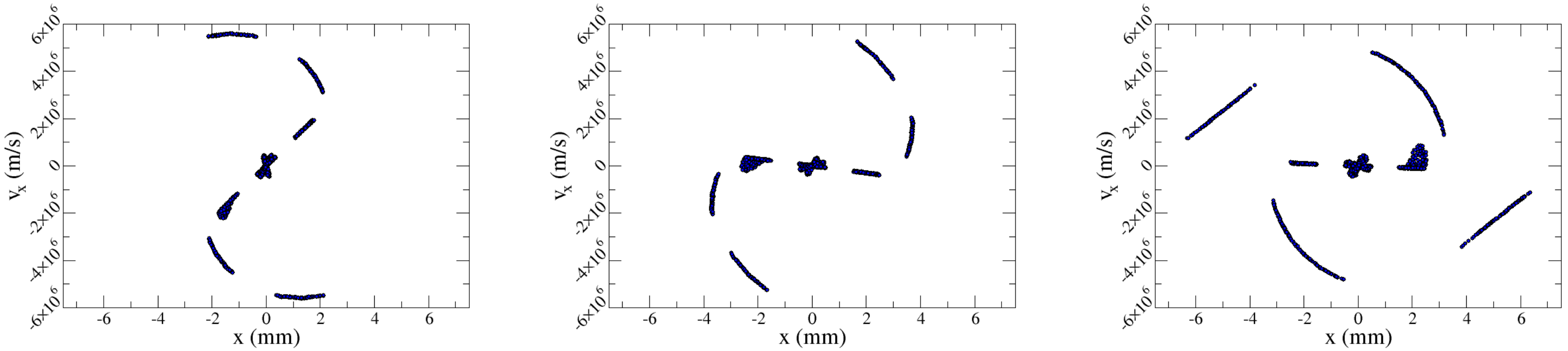

(d) Phase space: At $3/8\,\lambda_{\mathrm{bet}}$

(e) Phase space: At $1/2\,\lambda_{\mathrm{bet}}$

(f) Phase space: After one betatron oscillation

Figure 2.9.: Transport in a mismatched channel. Calculations for a 50 kA discharge in a 6 mm diameter channel. The betatron wavelength refers to the particles that oscillate inside the channel.

2.3.6. High-current beams

Up to now the effects of space charge have been neglected in our considerations. This approximation is justified for the UNILAC beams used in our experiments (see e.g. Table 2.3), since the beam currents are low and the focusing by the external magnetic field is much more important than the interaction between the beam particles. For the huge beam current required for a fusion reactor, however, the self-forces of the beam become very large, so that this approximation is no longer possible. The detailed modelling of high-current beams is challenging, since we can no longer calculate the trajectory of each particle separately, but must also take into account the field caused by the other particles. A realistic simulation requires a detailed simulation of the beam particles and the plasma channel (see [Wel02]). In the following, the magnitude of the beam effects is estimated with some simple models.

We start by analyzing a high-current beam without neutralization. Assuming a cylindrical beam with homogeneous current density, the maximum possible beam current is given by the Alfvén current[Hum90]

$$I_A = 4\pi\,\varepsilon_0\, m_B c^3\, \beta\,\gamma/Q \tag{2.67}$$

where m_B is the mass of the beam particle and Q its charge. For a beam with $\beta = 0.15$, $m_B = A_m \cdot u$ (u: nucleon mass), and $Q = Z \cdot e$ this simplifies to

$$I_A = \frac{A_m}{Z} \cdot 1.5 \cdot 10^6\,\mathrm{A} \tag{2.68}$$

so, in contrast to electron beams, this limit is usually not important for high-current ion beams.

The transverse expansion of the beam is much more important. The magnitude of the space-charge force can be estimated with a simple analytical model. In the following, we shall neglect end effects, that is we assume that the beam is infinitely long. This assumption is valid if the ratio of bunch length over bunch diameter is large. Typical reactor scenarios with assisted pinched transport work with beam velocities of roughly $\beta = 0.2$ and bunch lengths of 5 ns to 10 ns[Ros04], corresponding to a bunch length of 30 cm to 60 cm, so that the assumption made above is valid. Furthermore we assume cylindrical symmetry and a uniform particle density inside the beam bunch. The beam-generated fields then vary linearly with the radius. Because of our symmetry assumptions, the partial derivatives $\partial/\partial z$ and $\partial/\partial\theta$ vanish.

The charge density ρ_q is derived from the particle density n_0 and the average ion charge Q by $\rho_q = n_0\, Q$, so that the current density is given by

$$\mathbf{j} = \rho_q\, \mathbf{v} = \rho_q\, \beta\, c\, \mathbf{e}_z \tag{2.69}$$

Because of symmetry, the electric field has only a radial component ($\mathbf{E}(\mathbf{r}) = E(r)\,\mathbf{e}_\mathbf{r}$). It follows from the charge density by

$$\int_{\partial V} \mathbf{E} \cdot d\mathbf{f} = \int_V \rho_q/\varepsilon_0\, d\tilde{V} \tag{2.70}$$

where the area of the cylindrical shell is given by $d\mathbf{f} = 2\pi\, r\, dz\, \mathbf{e}_r$ and the volume is given by $d\tilde{V} = \pi\, r^2\, dz$. Integration then yields

$$E(r) = \frac{\rho_q}{2\varepsilon_0}\, r \tag{2.71}$$

Ion	Mass (u)	Energy (GeV)	β	I (A)	Bunch length (ns)	Energy (J)
Bi^{25+}	209	2.4	0.15	$1.0 \cdot 10^{-3}$	100,000	9.6
Pb^{72+}	207	3.0	0.17	$0.9 \cdot 10^{6}$	25	$0.9 \cdot 10^{6}$
Pb^{72+}	207	4.0	0.20	$4.8 \cdot 10^{6}$	8	$2.1 \cdot 10^{6}$

Table 2.3.: The parameters of a UNILAC beam used in our experiments and two possible driver beams for a fusion reactor. The two lead beams are the foot and the main pulse used to heat the hybrid target in the reactor scenario[Ros04, Wel03].

The electrostatic force leads to an expansion of the beam. The magnetic field created by the beam is given by

$$\int_{\partial F} \mathbf{B} \cdot d\mathbf{r} = \int_{F} (\nabla \times \mathbf{B}) \cdot d\mathbf{f} \tag{2.72}$$

and contracts the beam. In our case, the magnetic field is

$$B_\theta(r) = \frac{1}{2} \mu_0 \, j \, r \tag{2.73}$$

The relative influence of the space-charge force (F_space) and the beam-current force (F_beam) depend on the beam velocity. The ratio of the two forces is given by

$$\frac{F_\text{beam}}{F_\text{space}} = \frac{B_\theta(r)\, v}{E_r(r)} = \frac{\varepsilon_0 \, \mu_0 \, j \, \beta \, c}{\rho_q} = \beta^2 \quad . \tag{2.74}$$

Although this result was derived for a homogeneous beam density, it holds for arbitrary radial density profiles, since the magnetic field and the electric field are connected by the Lorentz transformation[Hum90]. In consequence, it is much easier to transport relativistic electron beams (β close to unity) than ion beams, since in the first case the magnetic force compensates most of the space-charge force, while in the latter case its influence is negligible.

The space-charge field in the beam ($r \leq R_0$) is given by

$$E(r) = \frac{I_\text{beam}}{2\pi R_0^2 \cdot \varepsilon_0 \, \beta \cdot c} \cdot r \tag{2.75}$$

and therefore proportional to the beam current I_beam. The maximum electric field, which is reached at the boundary of the beam, is inversely proportional to the beam radius R_0. As an example, take a 50 kA beam with a radius of 0.5 cm and a velocity of 0.15 c. Without neutralization, this results in an electric field of more than 28000 V/m.

The influence of the space charge compared to emittance effects can be determined by considering the differential equation for the beam envelope[Hum90] for the simplest case in which there are no external focusing forces and the effects of the acceleration of beam ions is negligible

$$\frac{d^2R}{dz^2} = \underbrace{\frac{\varepsilon^2}{R^3}}_{\text{emittance}} + \underbrace{\frac{K}{R}}_{\text{space charge}} \quad \text{with } K = \frac{e \cdot I_0}{2\pi \, \varepsilon_0 \, m_0 \, (\beta \gamma c)^3} \tag{2.76}$$

In this equation, R is the radius of the beam envelope, ε is the beam emittance, I_0 is the net beam current, and m_0 is the mass of the beam ions. For a 50 kA bismuth beam with a velocity of $0.2c$ and a mass number of 209, the generalized perveance K is equal to $1.8 \cdot 10^{-3}$. A comparison with the emittance force shows that the effect of the space charge is much larger than the emittance force, since the channel has a diameter of 5 mm and the emittance is typically of the order of some mm-mrad. This estimate shows that it is absolutely necessary to neutralize the space charge and the current of the high-current beams to keep the divergence of the beam within reasonable limits.

2.3.7. Neutralization of space charge and beam current

It is possible to prevent the rapid spreading of the ion beam by neutralizing its space charge with free electrons. The z-pinch plasma is ideally suited to provide the required electrons [Ham70]. The free electrons neutralize the space charge of the beam nearly completely, since this reduces the potential energy of the beam-plasma system drastically. The electron density in the case of complete charge neutralization is given by

$$n_e = Z_b \cdot n_b + Z_i \cdot n_i \tag{2.77}$$

where Z_b is the charge state of the beam ions, n_b is the ion beam density, and Z_i and n_i are the charge state and the density of the plasma ions.

The beam-induced movement of the plasma electrons also leads to an additional return current which, depending on the plasma density, partly or completely neutralizes the ion beam current. If the beam current is only partially neutralized, the beam pinches. This is equivalent to the case of two current-carrying wires that also attract each other, since they are charge neutralized, but not current neutralized.

A detailed analysis of the dynamics of the beam-plasma system is complicated and requires the use of a particle-in-cell (PIC) simulation code, but it is possible to estimate the beam neutralization and the interaction between the beam and the plasma with analytical models.

The current neutralization can be calculated for the idealized case of a long, cylindrically symmetrical beam[Kag01]. In the following, the dynamics of the background and beam ions is neglected, that is the background ions are fixed and the beam ions move with the constant velocity v_{bz}. Furthermore, ionization effects are neglected and the plasma electrons are assumed to be cold, so that no thermal effects take place. Using these approximations, the electron flow velocity v_{ez} is given by a simple one-dimensional differential equation[Kag01]

$$-\frac{1}{r}\frac{\partial}{\partial r}\left[r\left(\frac{\partial}{\partial r}\left(m_{e0}\cdot\frac{v_{ez}}{\sqrt{1-v_{ez}^2/c^2}}\right)\right)\right] = \mu_0 \cdot e^2 (\underbrace{Z_b \cdot n_b \cdot v_{bz}}_{\text{beam current}} - \underbrace{n_e \cdot v_{ez}}_{\text{return current}}) \tag{2.78}$$

Here m_{e0} is the electron rest mass, v_{ez} is the flow velocity of the neutralizing electrons, Z_b is the charge state of the beam ions, n_b their particle density, and n_e is the electron density. Equation 2.78 shows that the current neutralization is best at the center of the beam, as the gradients vanish there. Near the border of the beam, the gradients in the electron velocity and the beam density become large, resulting in an imperfect neutralization of the beam current.

The overall efficiency of current neutralization depends on the ratio of the beam radius r_b to the skin depth c/ω_p, where ω_p is the plasma frequency of the ambient plasma. The beam current is well neutralized if[Kag01]

$$r_b \gg \frac{c}{\omega_p} \tag{2.79}$$

Since the plasma frequencies in the channel are well above 10^{12} 1/s (see Table 2.1) and the beam diameter in fusion reactor schemes is typically of the order of 1 cm, this criterion is always fulfilled. In the case of good current neutralization, the background electrons are slowly co-streaming within the beam and thereby reduce the current density to zero. The flow velocity of the electrons follows from Equation 2.78 and is[Ham70, Kag01]

$$v_{ez} = Z_b v_{bz} n_b / n_e \tag{2.80}$$

The kinetic energy that must be transferred from the beam to the co-streaming electrons is proportional to $n_e \cdot v_{ez}^2$. Therefore the required energy decreases with increasing electron density, so that a good current neutralization is much easier with a high electron density than with a low density.

To calculate the net current within the channel in the case of imperfect neutralization, we assume that the ion beam density is given by a step-function profile

$$n_b(r) = \begin{cases} n_{b0} & \text{for} \quad r \leq r_b \\ 0 & \text{for} \quad r > r_b \end{cases} \tag{2.81}$$

For such a homogeneous beam, its density n_b is related to the electric current I_b by the relation

$$n_{b0} = \frac{I_b}{\beta_b c Z_b e \pi r_b^2} \tag{2.82}$$

Therefore a beam with a current of 1 kA and a diameter of 0.5 cm corresponds to a maximum beam density of $1.3 \cdot 10^{18}$ 1/m^3 (less for charge states higher than 1). The total net current in the beam region is given by[Kag01]

$$I_{\text{net}} = \sqrt{\frac{\pi}{4\varepsilon_0}}\, e \int_0^{r_b} (Z_b n_b v_{bz} - n_e v_{ez})\, r\, dr \simeq 4.25 \beta_b \cdot Z_b \cdot \frac{n_{b0}}{n_e} \cdot \frac{r_b}{c} \cdot \omega_p \,[\text{kA}] \tag{2.83}$$

where β_b is the relativistic beam velocity. If the ambient plasma density is much larger than the beam density, the electron density is nearly independent from the beam density (see Equation 2.77) and the relative neutralization of the beam depends only on the plasma density and the beam radius

$$\frac{I_{\text{beam}} - I_{\text{net}}}{I_{\text{beam}}} = 1 - \frac{4.25 \cdot \omega_p \cdot 1\,\text{kA}}{n_e \cdot e \cdot c^2 \cdot \pi \cdot r_b} \tag{2.84}$$

as long as the plasma density is sufficiently larger than the beam density, so that good charge neutralization is guaranteed. Assuming a beam radius of 0.5 cm, the relative neutralization for $n_e = 10^{20}\,\text{m}^{-3}$, $n_e = 10^{22}\,\text{m}^{-3}$, and $n_e = 10^{24}\,\text{m}^{-3}$ is therefore 89.5%, 99.0%, and 99.9%, respectively. For a smooth radial beam profile the current neutralization is even better, so that for typical plasma channel parameters the ion beam current is nearly completely neutralized. The results from the analytical model are consistent with that of PIC simulations[Kag01].

2.3.8. Hydrodynamic response of the channel to the ion beam

So far, the channel was assumed to be static during the beam transport. As far as the normal magnetohydrodynamical motion of the channel is concerned, this assumption is valid, since the duration of the beam pulse is typically between 10 ns and 25 ns, which is well below the hydrodynamical timescale, which is of the order of a microsecond. Yet the ion beam also interacts with the plasma channel and leads to its expansion, which might worsen its transport capabilities.

The influence of the effect of the beam on the plasma channel dynamics is checked with a simple analytical model. Because of the good current neutralization in the interior of the beam, the magnetic field B is approximately identical to that of the channel without the beam[Ott81a, Col80], that is

$$B(r_0) = \frac{\mu_0 I_{\mathrm{ch}}}{2\pi\, r_0} \tag{2.85}$$

at the channel boundary. The discharge current I_{ch} is typically of the order of 50 kA. The net current density in the channel is given by[Ott81a, Col80]

$$j_{\mathrm{net}} = j_{\mathrm{ch}} - j_{\mathrm{beam}} \tag{2.86}$$

since the beam current induces a counterstreaming return current in the plasma. For a step-function beam profile with beam radius r_0, the three current densities are therefore given by

$$j_{\mathrm{ch}} = \frac{I_{\mathrm{ch}}}{\pi r_0^2}\,, \qquad j_{\mathrm{beam}} = \frac{I_{\mathrm{beam}}}{\pi r_0^2}\,, \qquad \text{and} \quad j_{\mathrm{net}} = \frac{I_{\mathrm{ch}} - I_{\mathrm{beam}}}{\pi r_0^2} \tag{2.87}$$

Starting point is the MHD force equation

$$\rho \cdot \frac{d\mathbf{v}}{dt} = -\nabla p + \mathbf{j} \times \mathbf{B} \approx \mathbf{j} \times \mathbf{B} \tag{2.88}$$

where ρ is the mass density of the channel. The kinetic term due to pressure gradients can be neglected, since the dynamics is dominated by the magnetic forces. Assuming cylindrical symmetry, neglecting end effects and inserting Equations 2.85 and 2.87 yields for the envelope of the channel

$$\ddot{r} = -\frac{1}{\rho}\,\frac{\mu_0 I_{\mathrm{net}}\, I_{\mathrm{ch}}}{2\pi^2\, r_0^3} \tag{2.89}$$

As the net current is negative for large beam currents, this leads to an expansion of the channel. An upper limit for the radial expansion is

$$\Delta r \le \frac{1}{2}\ddot{r}(t=0)\,(\Delta t)^2 = \frac{\mu_0 I_{\mathrm{ch}}}{4\pi^2 \cdot r_0^3} \cdot \frac{I_{\mathrm{net}} \cdot (\Delta t)^2}{\rho} = 1.27 \cdot 10^4\, \frac{\mathrm{Vs}}{\mathrm{m}^4} \cdot \frac{I_{\mathrm{net}} \cdot (\Delta t)^2}{\rho} \tag{2.90}$$

for a channel with an initial radius r_0 of 5 mm. This sets a lower limit for the channel mass density for a given set of beam parameters in order to guarantee a successful beam transport to the hohlraum target. The beam parameters for both the foot pulse and the main pulse are given in Table 2.3. If we take a channel mass density of $5.3 \cdot 10^{-3}\,\mathrm{kg/m^3}$, corresponding to 1 mbar xenon at room temperature, the estimate gives an upper limit for the channel expansion of 1.4 mm for the foot pulse (0.9 MA, 25 ns) and 0.8 mm for the main beam pulse (4.8 MA, 8 ns). This is sufficiently low to ensure beam transport, yet it indicates that the use of a light channel gas like helium is problematic due to the faster expansion of the channel.

2.3.9. Beam-plasma instabilities

The beam-plasma system has a highly anisotropic axial velocity distribution and therefore may be susceptible to various kinetic instabilities. Depending on their direction of propagation (which is given by the wave vector $\mathbf{k}$), these instabilities can be divided into longitudinal and transverse instabilities. To illustrate the initial situation, the undisturbed velocity distribution during beam passage is sketched in Figure 2.10. The system consists of three particle sets with different temperatures and different flow velocities. The beam ions have the largest velocity (v_b), typically about $0.2\,c$, and a low axial velocity spread, corresponding to a low beam temperature. In contrast, the plasma ions are, on average, at rest, but have a temperature of several electron-volts. Due to heating by the ion beam, the plasma electrons are slightly hotter than the plasma ions. In addition, they are also co-moving with the beam ions to neutralize the beam current. Yet their flow velocity is much smaller than that of the beam ions, since their density is much larger (see Section 2.3.7 for details about beam neutralization).

One instability that might affect the beam transport is two-stream instability[Hum90] involving the beam ions and the plasma electrons. For effective excitation, the frequency of the mode must be close to the plasma frequency of the electrons ($\omega \approx \omega_p$). Particles with velocity v_i excite modes with wavenumbers $k_i \approx \omega_p / v_i$. The growth rate is strongest if the velocity spread of the beam, and thus its temperature, is negligible. A finite beam temperature therefore reduces the growth rates, since different modes are excited and only a part of the beam particles takes part in the excitation of each mode. Collisional processes further impede the growth of these modes. Analytical studies for the transport of light-ion beams in plasma channels[Ott81a, Ott79] found that the system is stable for typical channel and beam parameters. For a heavy-ion driver, the beam velocities are similar to those in the case of a light-ion driver, yet the beam current is significantly reduced. The system therefore should be stable as well.

Another possible two-stream instability may arise between the plasma electrons and the plasma ions. Yet the electron flow velocity is much smaller than that of the beam ions, and the temperature of the plasma ions is much larger than that of the beam, so instability is even more unlikely than for the previous mode. The drifting electrons could also excite an ion-acoustic mode in the plasma. Yet a sufficient growth rate requires the electron temperature to be much larger than the ion temperature. Because of this condition, ion-acoustic turbulence is not expected in this system[Ott81a].

Apart from these electrostatic modes, electromagnetic modes might impede beam transport. Two modes have been studied: the Weibel instability[Wei59] (radial current bunching, $\mathbf{k} = k\,\mathbf{e}_r$) and the whistler mode (azimuthal current bunching, $\mathbf{k} = k\,\mathbf{e}_\theta$). Analysis of these modes[Ott81a, Ott81b] shows that the Weibel instability does not grow significantly during the passage of the beam. The growth of the whistler instability can be reduced to tolerable levels by a small spread in the angular momentum of the beam ions.

In conclusion, stability analysis suggests that the system is sufficiently stable and that the

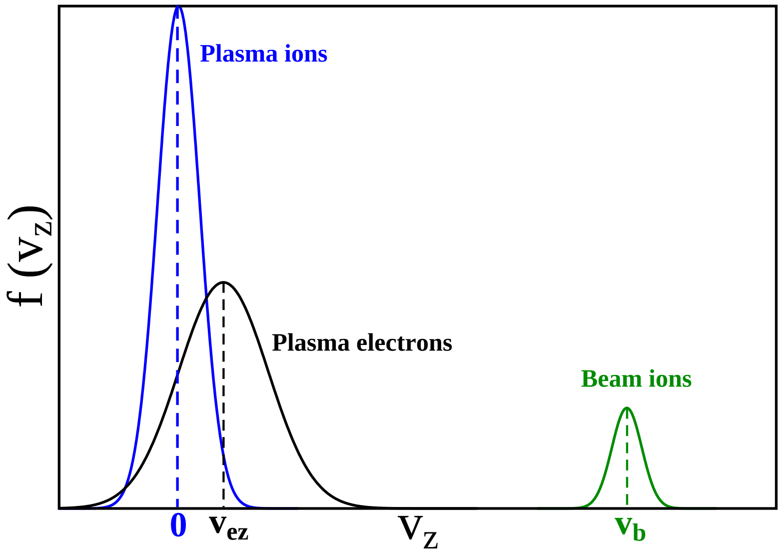

Figure 2.10.: Particle distribution in the beam-plasma system (schematic). Illustrated is the situation for the beam current being larger than the discharge current, so that the plasma electrons are co-moving with the beam ions.

development of microinstabilities is suppressed. The z-pinch should therefore be capable of transporting high-current beams with parameters required for a fusion driver.

2.3.10. Particle-in-cell simulations of the beam-plasma system

In order to study the properties of assisted pinched transport for high-current beams, detailed numerical simulations were carried out by Mission Research Inc. as part of the ARIES reactor study[Ros04, Wel03]. In the following, the basic assumptions used in the modelling and the main results are summarized shortly.

The calculations simulate both the focusing of the ion beams by the adiabatic plasma lens and the transport inside the plasma channel towards the target. As the focus of the simulations is on the beam transport, the channel formation is not covered by these simulations. The simulations utilize the hybrid code IPROP, which models the beam with a PIC code and the plasma with a two-fluid model, using separate temperatures for the plasma electrons and ions. The simulations are two-dimensional, so cylindrical symmetry is assumed.

Various approximations simplify the modelling. While the charge state of the plasma ions can change due to impact ionization by the ion beam, the charge state of the beam ions is fixed. Furthermore it is assumed that the electron temperature is high and that the ion ionization is dominant, so that recombination processes and electron avalanches can be neglected. Finally, radiation by free or bound electrons is also neglected.

Figure 2.11 shows the result of a simulation run. The boundary of the plasma lens and the channel is indicated by a red line. The plasma lens is 125 cm in length, starts with a radius of 2 cm and leads into the plasma channel, which has a radius of 0.5 cm. The length of the channel is 325 cm.

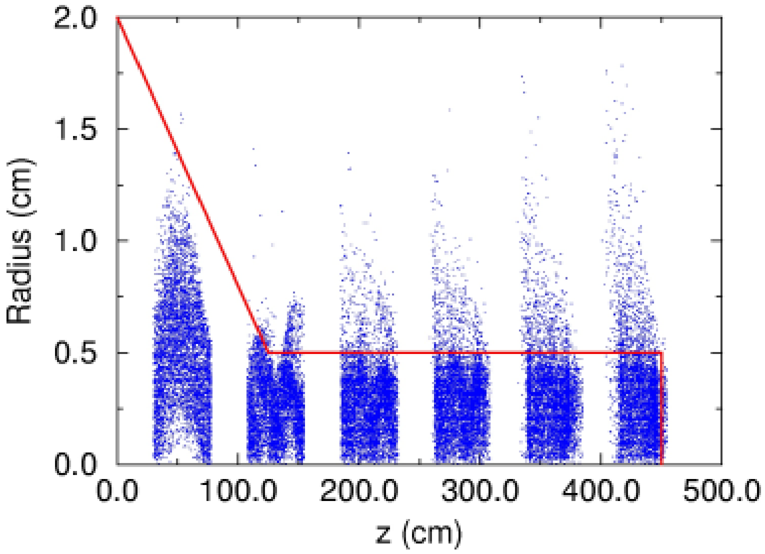

Figure 2.11.: Combined MHD and particle-in-cell simulation for a high-current heavy-ion beam in a final transport system consisting of an adiabatic plasma lens and a plasma channel (the boundary is indicated). Simulation by D. V. Rose and D. R. Welch, Mission Research Corp.[Wel03]

Simulated were driver beams for a hybrid target with a 1 cm absorber[Cal02]. The driver consists of two subsequent pulses, a long low-energy foot pulse which preheats the target absorbers, and a short high-energy main pulse supplying most of the energy. The parameters for lead driver beams are listed in Table 2.3. The chamber was filled with xenon, which had an ambient pressure of 5 Torr. Inside the channel, the density was reduced to the equivalent of 0.5 Torr at room temperature. The initial plasma temperature was 3 eV. The transport efficiency was studied for discharge currents varying between 25 kA and 75 kA. At 50 kA, 87% of the beam energy reached the target, 4% being inductive losses, 6% due to collisions with the plasma, and the rest due to the loss of particles. As is visible in Figure 2.11, some of the particles leave the channel and thereby miss the target. Increasing the discharge current to 75 kA increased the transport efficiency only insignificantly, whereas reducing it to 25 kA reduced the efficiency to 80%. To study the influence of the ion species on the beam transport, the transport was also modelled for Xe^{44+} beams with identical duration and total energy. This change did not result in a significant change of transport efficiency. In summary, the studies showed good beam transport properties for moderate discharge currents of 50 kA and beams with currents required to ignite a hybrid target.

2.4. Operating parameters for assisted pinched transport

Based on these results, it is possible to outline an operating regime for assisted pinched transport. The beam parameters and the channel radius are determined from the properties of the hybrid target[Cel03, Cal02]. To ignite the target, a total energy of 6 MJ is deposited by the driver beams. The current scenario uses Pb^{+72} ions to heat the target. The target absorbers are preheated with two 25 ns long pulses with energies of 0.9 MJ and then the target is ignited by two 8 ns long pulses with energies of 2.1 MJ (for details see Table 2.3). The channel diameter is adjusted to the 1 cm absorbers to guarantee an optimal heating. Its length depends on the chamber radius, which in turn depends on the shielding concept. For thick-liquid wall shielding, typical chamber radii are of the order of 3 m.

The necessary discharge current depends on the magnetic field that is necessary to transport the beam. Fifty kiloampere seems to be the optimum current for the transport of the driver beam. The simulations indicate that the transport efficiency drops by 7% if the current is reduced to 25 kA. Increasing the current to 75 kA does not effect the transport efficiency significantly, but does increase the expansion due to the $j \times B$ force and might increase the likelihood of MHD instabilities.

To minimize energy losses, the density in the channel should be as low as possible. In order to minimize the $j \times B$ expansion, xenon is used as a chamber gas. The simulations assume an ambient density corresponding to 5 Torr, which is reduced to the equivalent of 0.5 Torr inside the channel. The experiments so far produced channels in xenon for pressures about 1 mbar, but a more efficient channel initiation using a short-pulse laser should make it possible to generate channels at higher pressures. Furthermore, the geometry of the reactor chamber is more feasible than that used in our experiment, which is basically a metal tube. The density in the channel must not be too low, since otherwise the channel expansion by the $j \times B$ force gets to large. For very low densities, the charge and current neutralization would no longer be guaranteed. If, on the other hand, the density gets too high, the energy losses of the beam due to collisions increase and thereby reduce the transport efficiency. Theoretical analysis suggests that for this set of parameters no major beam induced instabilities develop during the passage of the beam. To validate this would require high-current heavy-ion beams that are not available in the near future.

3. The experimental setup

The channel-transport experiment is located at the *Gesellschaft für Schwerionenforschung*. Its goal is to study the dynamics of plasma channels and their transport properties for low-current ion beams. In conjunction with the simulations for high-current beams this yields the operating window for channel transport, that is the parameter range in which beam transport is feasible.

Figure 3.1 shows the experimental setup. The gas-filled discharge chamber is connected to the accelerator by a differential pumping section. This section uses several small apertures in combination with two roots pumps and two turbomolecular pumps to reduce the gas pressure from some millibars inside the chamber down to the 10^{-6} mbar required in the accelerator. A pepperpot mask is mounted about 20 cm before the chamber entrance. It is basically a molybdenum plate with several holes (with diameters between 1 mm and 3 mm) and gives the ion beam a definite shape. In addition, it serves as a mirror to reflect the laser beam into the chamber. The chamber is 60 cm in diameter, 1.06 m long, and made of stainless steel. Its wall consists of three parts, which are separated from each other by two nylon flanges, so that they are electrically insulated from each other. A voltage divider is used to set each part of the chamber to a separate potential. The chamber has eight portholes. With the exception of one porthole, which is used as an gas inlet for the chamber, all portholes can be used to employ various diagnostics, like cameras, interferometry, spectroscopy, or to insert probes to study the magnetic field[Nef04, Nie03b, Nie02, Pen02c]. Apart from the portholes, the whole chamber is rotationally symmetric. The two electrodes are mounted at the two ends of the chamber and are separated from the walls by Plexiglas insulators, which prevent an electric breakdown from the electrodes to the walls. The electrodes are hollow, so that the ion beam and the laser can enter the chamber through the anode.

3.1. Electrical setup

Two pulse generators, the schematic circuits of which are shown in Figures 3.2 and 3.3, create the discharge channel. Their functional principle is simple. In a first step, the capacitor in the generator is charged with a power supply. A high-impedance resistor limits the charging current to protect the equipment. A connection with a 4 kΩ resistor ensures that both chamber electrodes are set to ground potential during the charging. When the capacitor is fully charged, the generator is ready. A signal pulse triggers a high-current switch. This closes the circuit, so that the capacitor voltage is applied to the chamber electrodes. A voltage divider with four high-impedance resistors is put in parallel, and sets the potentials for the three chamber walls. The breakdown in the chamber gas creates a channel with a very high conductivity, so that most of the discharge current flows through the chamber. A shunt, that is a low-impedance

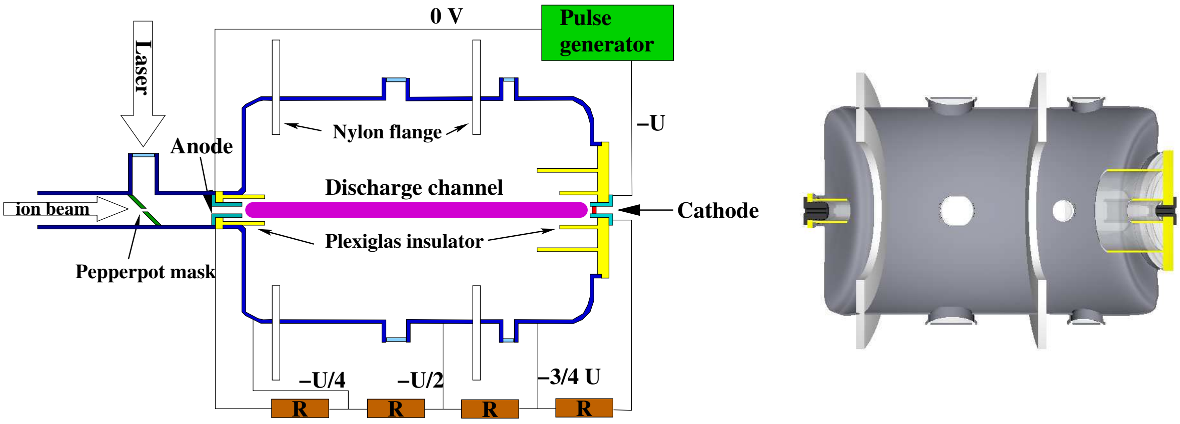

Figure 3.1.: A schematic view of the experiment and a cross-section through the discharge chamber. The chamber has a length of 1 m and a diameter of 60 cm; it consists of three parts, each set to a different potential by a voltage divider.

resistor, is connected in series. The shunt is used to measure the discharge current, as the voltage at the shunt is proportional to the current. Two safety measures are implemented to avoid accidents. If the charging voltage is turned off, the capacitors slowly discharge over high-impedance resistors. In addition, the generator for the main pulse is also connected to an interlock system. If the generator casing is opened or the interlock is otherwise enabled, the capacitor bank is short-circuited using a low-impedance resistor, so that a fast discharging of the bank is guaranteed.

Because of their different purposes, the technical data of the two generators vary significantly. The prepulse generator uses a single capacitor with a capacity of 200 nF that can be charged to voltages of up to 30 kV, equaling a stored energy of 60 J. An additional 5 Ω resistor damps the current, so that the duration of the prepulse is limited to 1 µs.

The generator for the main pulse uses a capacitor bank, consisting of six capacitors. It has a total capacity of 8 µF and can be charged to voltages of 25 kV, so that it can store an energy of 2.5 kJ.

During the discharge, the whole setup can be represented by a RLC circuit with the resistivity, inductivity, and capacity connected in series. The resistance and the inductance of the circuit depend on the plasma channel parameters, which change during the discharge. The differential equation for this circuit is

$$\frac{Q}{C} + L \cdot \frac{dI}{dt} + R \cdot I = 0 \tag{3.1}$$

Expressing this in terms of the charge Q yields

$$\frac{d^2Q}{dt^2} + \frac{R}{L}\frac{dQ}{dt} + \frac{Q}{C \cdot L} = 0 \tag{3.2}$$

The solution to this equation is

$$Q(t) = Q_0 \cdot \exp(-\alpha t) \tag{3.3}$$

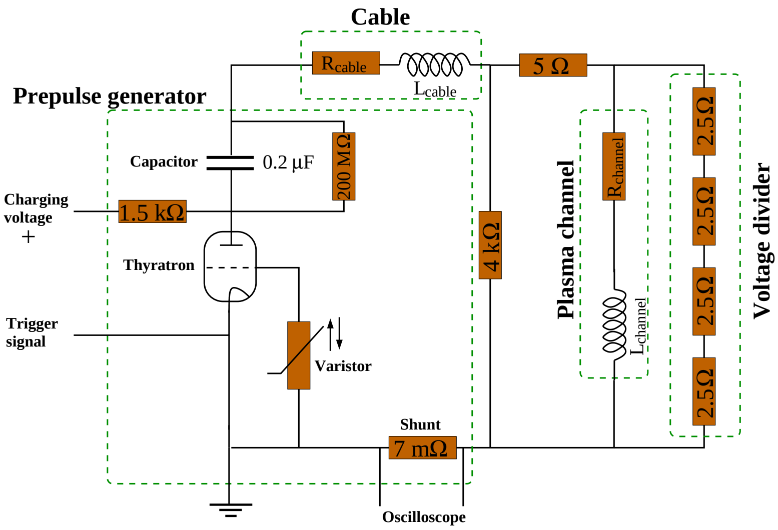

Figure 3.2.: Electrical setup of the prepulse generator.

with α given by

$$\alpha = \frac{R}{2L} \pm \sqrt{\frac{R^2}{4L^2} - \frac{1}{C \cdot L}} \tag{3.4}$$

Depending on the argument of the square-root, three different cases must be distinguished. If the argument of the square-root is zero, the time development of the capacitor charge is given by

$$Q(t) = Q_0 \cdot \exp\left(-\frac{R}{2L}t\right) \tag{3.5}$$

If the argument of the square-root is negative, the result is given by a damped oscillation

$$Q(t) = Q_0 \cdot \exp\left(-\frac{R}{2L}t\right) \cdot \exp\left(\pm i\omega t\right) \tag{3.6}$$

with the frequency

$$\omega = \sqrt{\frac{1}{C \cdot L} - \frac{R^2}{4L^2}} \tag{3.7}$$

Finally, if the argument of the square-root is positive, the result is again an exponential decay, but with a modified damping rate

$$Q(t) = Q_0 \cdot \exp\left(-\left(\frac{R}{2L} \pm \sqrt{\frac{R^2}{4L^2} - \frac{1}{L \cdot C}}\right)t\right) \tag{3.8}$$

The actual discharge curve differs from this solution, since the channel resistivity and inductivity are not fixed, but vary during the evolution of the channel. While the resistivity of the channel is dominant in the initial stages of the channel formation, it becomes negligible once a channel is established. The measured current profiles therefore match the oscillatory solution very well, with the exception of the start of the discharge.

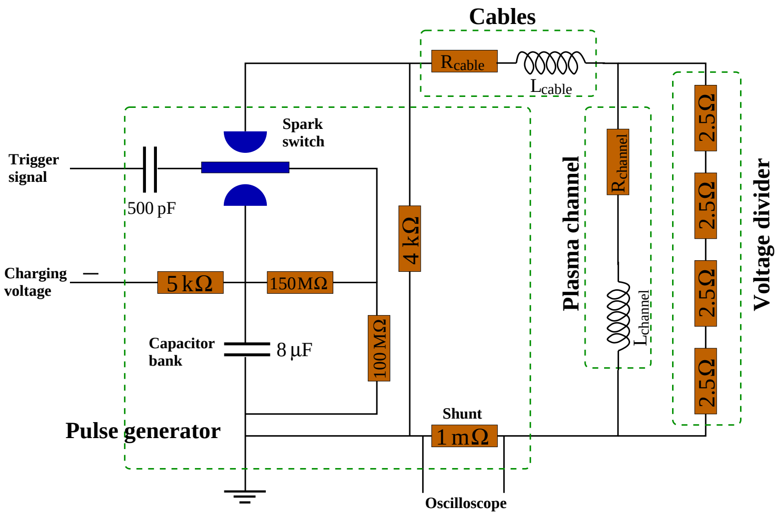

Figure 3.3.: Electrical setup of the main generator. The generator is also connected to an interlock system (not shown in this schematic).

The resistance and the inductance of the channel are essential for the dynamics of the discharge. The derivation of the channel is straightforward, provided the plasma conductivity σ is known. For a homogeneous channel with radius R_{ch} and length L_{ch} it is given by

$$R = \frac{1}{\sigma}\frac{L_{\mathrm{ch}}}{\pi \cdot R_{\mathrm{ch}}^2} \tag{3.9}$$

Typical plasma conductivities in our setup are of the order of $10^5\,\Omega$m. For a 1 m long channel with a radius of 1 cm, this results in a resistivity of 0.1 Ω. Another important characteristic property is the inductance of the channel. The inductance L is defined by the relation

$$W_m = \frac{1}{2}\int \mathbf{B}\cdot\mathbf{H}\,dV = \frac{1}{2}L\cdot I^2 \tag{3.10}$$

where W_m denotes the energy of the magnetic field, which is calculated by integrating over the volume. The magnetic field of the channel is

$$B(r) = \begin{cases} \frac{\mu_0 I}{2\pi R_{\mathrm{ch}}^2}\cdot r & \text{for} \quad r \le R_{\mathrm{ch}} \\ \frac{\mu_0 I}{2\pi r} & \text{for} \quad r > R_{\mathrm{ch}} \end{cases} \tag{3.11}$$

Integration and solving for L yields

$$L = \frac{\mu_0 L_{\mathrm{ch}}}{2\pi}\left[1/4 + \ln\left(R_A/R_{\mathrm{ch}}\right)\right] \tag{3.12}$$

The inductance, like the resistance, is proportional to the length of the channel. The outer integration limit R_A denotes the radius where the magnetic field vanishes. Since the return current is not transported in a coaxial configuration, but by two conducting copper bands, the results is only approximately valid. Nevertheless, the calculation is sufficient to get a rough estimate of the inductance. If we take the outer radius R_A as 45 cm, the channel radius as 1 cm, we obtain an inductance of 814 nH for a 1 m long chamber. For comparison, the inductance of the generator and the cables is approximately 400 nH[Pen02c].

A quick estimate shows that the capacity of the discharge chamber is negligible. For the sake of simplicity, the chamber is treated as a coaxial cable, the channel being the inner conductor (radius R_1) and the chamber walls being the outer conductor (radius R_2). The radial electric field in the chamber is then given by ($R_1 \leq r \leq R_2$)

$$E(r) = \frac{Q}{2\pi r L \varepsilon_0} \tag{3.13}$$

where L is the chamber length. Integration of the energy density $E^2/2$ over the volume yields the total field energy inside the chamber. Since the electrostatic field energy is also given by $Q^2/(2C)$, the capacitance is given by

$$C = \frac{2\varepsilon \pi L \varepsilon_0}{\ln(R_2/R_1)} \tag{3.14}$$

Inserting the parameters of our chamber results in a capacitance of $5.2 \cdot 10^{-12}$ F, which is more than five orders of magnitude smaller than the capacitance of the pulse generators and can therefore be neglected.

3.2. Chamber optimization

In order to successfully create plasma channels, it is necessary to guide the discharge in the chamber. It is clear from Ohm's law and Paschen's law that three factors determine the discharge path inside the chamber: the gas density, the conductivity of the gas prior to the discharge, and the electric field inside the chamber. A detailed modelling of the discharge would be necessary to determine under which conditions a breakdown to the walls can be avoided, but it is clear from these basic considerations that a density reduction along the axis (thereby getting closer to the Paschen minimum), an ionization along the axis, and an optimization of the electric field all favor a discharge along the axis and suppress breakdowns to the walls. As mechanisms for channel initiation will be dealt with in the next section, the focus of this section is on optimizing the electric field inside the chamber.

The old setup consisted of a 50 cm long chamber which was 60 cm in diameter. The full discharge voltage was applied to the two electrodes, and the metallic chamber wall was set to mid-potential. Since it was possible from the start to create stable channels, it was not necessary to optimize the electric field inside the chamber. Things changed drastically with the prolongation of the discharge chamber. The additional 50 cm in length changed the chamber geometry, resulting in a modification of the electric field inside the chamber. Due to these changes, breakdowns to the chamber walls became dominant and it was hard to create discharge channels at all.

As an optimization requires a precise knowledge of the electric field before the discharge, field calculations were carried out with POISSON[Bil93]. POISSON is an electrostatic and magnetostatic field solver written at the *Los Alamos National Laboratories*. In the case of electrostatics, it solves the Poisson equation[Jac98, Sch87]

$$\Delta\Phi = -\rho_q/\varepsilon_0 \tag{3.15}$$

for the electric potential Φ (ρ_q is the charge density). POISSON can solve this differential equation for three-dimensional configurations with cylindrical symmetry and is therefore ideally suited for our setup. Each part of the chamber is given by a set of spline data for its boundary and the specification of the material (metal or dielectric). Each electrode is set to a fixed potential (free-floating electrodes are also possible) and the dielectric constants of the insulators are specified. Naturally, a completely specified electrostatic problem requires boundary conditions. The cylindrical symmetry implies that the electric field on axis must be parallel to the symmetry axis. Furthermore it is assumed that the electric potential is zero on the calculation boundary. This is strictly true only for boundaries at infinite distances, but the error for the field on axis is negligible, provided the boundaries are sufficiently far away. POISSON uses the finite element method to solve the problem, and thus creates a fine mesh that covers the integration area. Since the precision of the calculation decreases with increasing mesh size, a mesh consisting of up to 1,500,000 mesh points was used. The mesh resolution can be locally adjusted to account for regions with large electric fields, for example near the electrodes. An example of the generated mesh is shown in Figure 3.4. The mesh is not generated inside of conductors, since these are field-free in electrostatics.

Figure 3.5c shows the calculated electric potential for the short setup. The electrodes are set to -30 kV and 0 V, respectively, and both parts of the chamber wall are set to a mid-potential

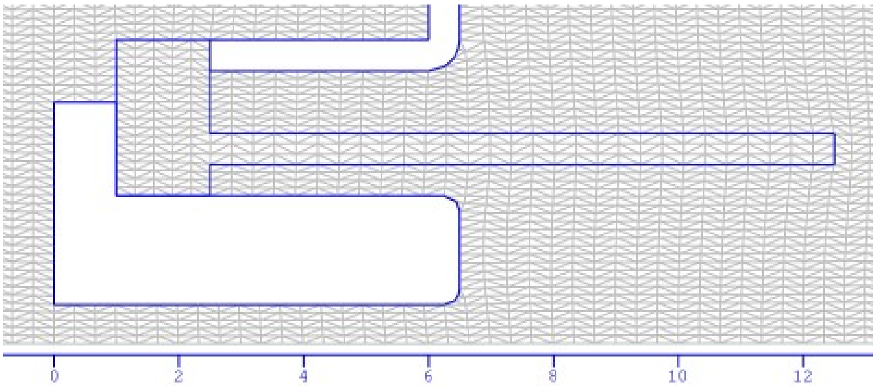

Figure 3.4.: Cutout of the POISSON grid near the electrode. Note that this example uses 96,000 mesh points, whereas the field calculations used 1,500,000 mesh points.

of -15 kV. The potential lines are drawn in 1 kV steps. It is clear from this picture that the largest potential gradient and thus the largest electric field is near the electrodes, whereas the minimum electric field is near the middle of the chamber. The electric field along the axis is plotted in Figure 3.5d. It reaches its maximum of 4000 V/cm near the anode and drops to a minimum of 124 V/cm at $z = 23$ cm. For a Paschen parameter of $p \cdot d = 100\,\text{mbar} \cdot \text{cm}$ the breakdown field strength is roughly 20 V/cm in xenon and krypton[Bha76, Bha79] and even lower in ammonia (see Figure 3.6). Thus the field strength in the chamber is sufficient for channel creation.

Figure 3.5a shows the electric potential in the prolonged chamber. The situation is identical to the previous calculation, with the exception of the chamber length. The potential near the electrodes is very similar to the potential in the short chamber, but the potential gradient in the center of the chamber is drastically reduced. The electric field (Figure 3.5d) now drops from 4000 V/cm to a minimum of 8 V/cm at $z = 44$ cm. So the electric field drops by a factor of 500 from the electrode to the center of the chamber, making it impossible to create stable discharge channels. This made it necessary to optimize the electric field in the chamber.

There are two ways to improve the field ‘quality’. One can either change the chamber geometry or the applied potentials. Since the first method is both time-consuming and expensive, the second alternative was chosen. As the chamber wall consists of three separate parts, each part can be set to an individual potential, provided that the walls are electrically insulated from each other. For this purpose, two nylon flanges were mounted between the walls, as illustrated in Figure 3.1. The flanges are 3 cm thick, resulting in a 6 cm channel prolongation, and have an inner diameter of 40 cm and an outer diameter of 90 cm. A voltage divider consisting of four 2.5 Ω resistors sets the three wall parts to -22.5 kV, -15 kV, and -7.5 kV, respectively. The calculated potential is shown in Figure 3.5b. The potential in the chamber is now much more homogeneous than before. The electric field (Figure 3.5d) still reaches its maximum at the electrodes and reaches its minimum at the center of the chamber, but this time the field drops from a maximum of 2000 V/cm to a minimum of 117 V/cm, which is only marginally smaller than the minimum in the old setup. The calculations are in agreement with the experiments, which demonstrate that the improved field configuration makes it possible to create stable channels in the long chamber.

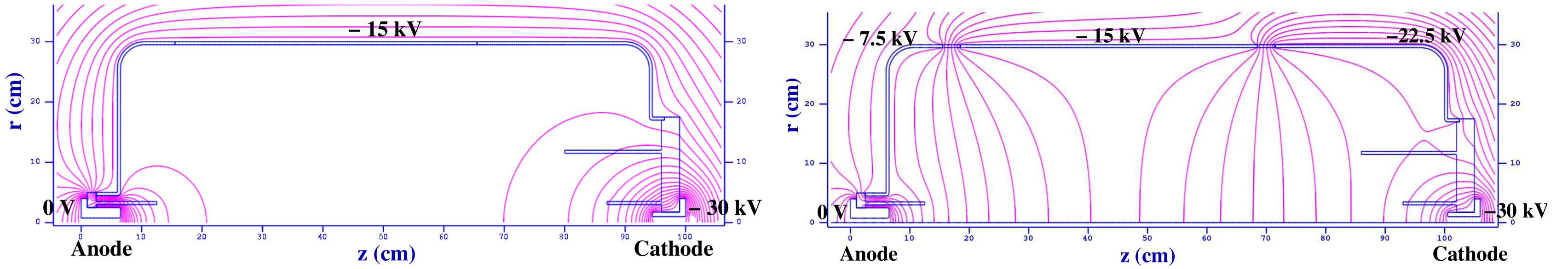

(a) Long chamber with only one wall potential.

(b) Long chamber with three wall potentials. The walls are separated by two flanges.

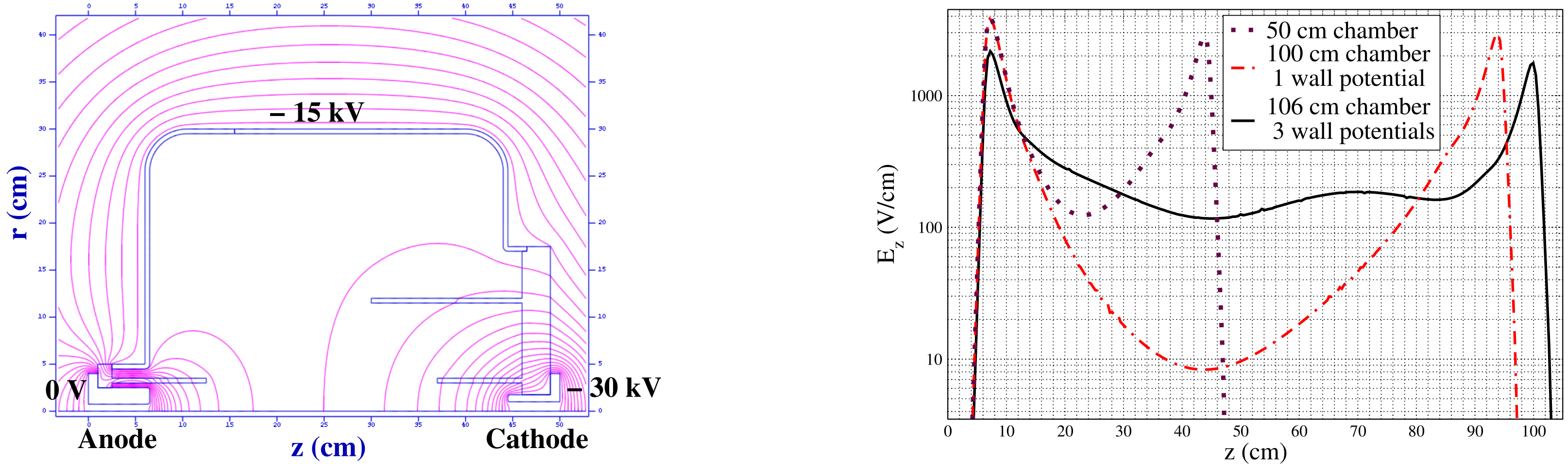

(c) Old experimental setup (50 cm chamber)

(d) Electric fields along the axis ($r = 0$)

Figure 3.5.: Poisson calculations for three electric setups. All calculations assume cylindrical symmetry. Pictures (a), (c), (b): equipotential lines (1 kV steps). Graph (d): electric field along the symmetry axis for the three scenarios.

3.3. Channel creation

An optimized electric field inside the chamber is a necessary, but by no means sufficient condition for creating a discharge channel. Without some kind of guiding mechanism, the discharge will simply break down from the electrode to the adjacent chamber wall. In our experiment, there are two possibilities to guide the discharge: either by ionizing the gas with an ion beam or by heating it with a laser. The ion beam guides the discharge by creating free electrons along the channel axis, whereas the laser heating results in a rarefaction of the gas on axis, which reduces the breakdown voltage. Both methods are used, since they complement each other in their fields of application. While the initialization with the ion beam can be used with all chamber gases, the applicability of the laser heating is limited to ammonia in our setup. This is due to the absorption bands of ammonia in the infrared spectral regions. If the wavelength of the carbon-dioxide laser is fine-tuned to one of these absorption bands, the laser absorption increases greatly compared to the untuned case. Unfortunately, only few gases possess absorption bands near the laser wavelength of 10.6 µm, the most practical and cheapest of them being ammonia.

Despite being limited to ammonia, laser heating is not superfluous, since it has the advantage that it does not require an ion beam and can therefore be used outside of beamtimes to test the experimental equipment and to study the channel dynamics. In addition, by splitting the laser beam, it is also possible to create crossed discharges[Nie02], which is not possible with the ion beam. Furthermore, the reactor scenarios propose the use of a short-pulse laser for channel initiation. In this case, the absorption is high in all gases. After the channel is initiated by either method, the prepulse is triggered in order to stabilize the subsequent discharge. Finally, the plasma channel is created by the main discharge. All three stages of channel creation are studied in more detail in the following.

3.3.1. Breakdown conditions for a gas discharge

The knowledge of the breakdown characteristics in the chamber is essential for the experiments. For a given chamber geometry and assembly of the electrodes, the minimum breakdown voltage is determined by the species of gas, the gas pressure, and, although to a lesser extent, the cathode material. In the following, the breakdown condition is derived from some basic considerations, largely following the derivation in [Dru40, Dru41].

Below the breakdown voltage, a very small current flows between the electrodes, since processes like cosmic radiation or natural radioactivity always create a small amount of ions and free electrons in the gas. If these electrons and ions are able to create an avalanche of new free charges, a breakdown with a huge increase in the current follows. So the breakdown voltage is determined by the ionization rates. The ionization processes can be divided into two classes, namely first order processes and second order processes.

In first order processes, the electrons create new electron-ion pairs either by direct ionization or via meta-stable molecules. Both effects are described by the rate coefficient η, which is related to the first Townsend coefficient α by $\eta = \alpha/E$, E being the electric field. The increase of an initial current I passing a voltage dU by first order processes is proportional to

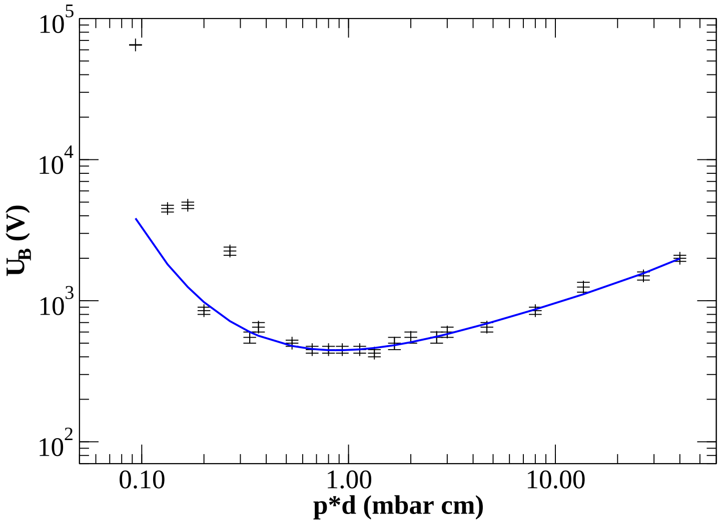

Figure 3.6.: Paschen curve for ammonia. The measurement used aluminum electrodes[Nat68].

the ionization coefficient

$$dI = \eta \cdot I \cdot dU \tag{3.16}$$

Integrating this equation yields the amplification for the initial current I_0

$$I = I_0 \cdot \exp\left[\eta (U - U_0)\right] \tag{3.17}$$

The integration constant U_0 is caused by space-charge effects at the electrodes and is usually in the range of (10-50) V. Since the breakdown voltages in our experiment are of the order of kilovolts, its effect is negligible. The experimental data for the ionization coefficient can be fitted to[Bro66]

$$\frac{\alpha}{p} = C_1 \cdot \exp\left[-C_2 \left(\frac{p}{E}\right)\right] \tag{3.18}$$

Unfortunately, the ionization rate is often very sensitive to traces of other gases, so that small impurities can lead to a significant change of the breakdown voltage.

Besides these direct ionization processes, secondary ionization processes play an important role. The secondary electrons can be liberated either at the cathode or in the gas. The agents that induce the processes can be positive ions, radiation quanta, or excited and meta-stable molecules. Which of these processes is dominant depends on the circumstances (E/p, cathode material, etc.). The rate coefficient for secondary processes is γ. If we take them into account, the current amplification is given by

$$I = I_0 \cdot \frac{\exp\left[\eta (V - V_0)\right]}{1 - \gamma(\exp[\eta (V - V_0)] - 1)} \tag{3.19}$$

We now determine the breakdown condition. At the point of gas breakdown, the initial current is multiplied by a very large factor, for example $I/I_0 = 10^{10}$. For all practical purposes, we can set the amplification to be infinite, yielding the condition that the denominator in Equation 3.19 must be zero, or, equivalently

$$\gamma(\exp[\eta(V_B - V_0)]) = 1 \tag{3.20}$$

so that the breakdown voltage V_B is

$$V_B = V_0 + \frac{1}{\eta} \cdot \ln\left(\frac{1}{\gamma} + 1\right) \approx \frac{1}{\eta} \cdot \ln\left(\frac{1}{\gamma}\right) \tag{3.21}$$

The coefficients η and γ, and therefore V_B depend on E/p. According to the Paschen law, the breakdown voltage can be written as a function of $p \cdot d$. This approximation holds only if the separation of the electrodes is small in comparison to the area of the electrodes, since otherwise some of the electrons and ions get lost at the borders, which alters the effective rate coefficients and therefore the breakdown voltage. In the case of a non-homogeneous electric field, as is the case in our experimental setup, the breakdown criterion must be altered to include the field variations[Dru40, Dru41]

$$\gamma \cdot \left(\exp\left[\int_{V_0}^{V_B} \eta \, dV\right] - 1\right) = 1 \tag{3.22}$$

The function $V_B(p \cdot d)$ is called a Paschen curve in the case of a homogeneous electric field. Figure 3.6 shows the Paschen curve in ammonia. The minimum breakdown voltage of $(440 \pm 20)\,\mathrm{V}$ is at $1\,\mathrm{mbar\,cm}$. In our chamber setup, the $p \cdot d$ value is in the range of (100 - 1000) mbar cm. So the discharges in our experimental setup are to the right of the Paschen minimum, even if we take the non-homogeneity of our electric field into account. A reduction of the gas density, for example by laser heating, therefore reduces the breakdown voltage.

3.3.2. Laser initiation

The laser beam is created by a carbon-dioxide laser (model: SLCR ML-204). It creates laser pulses with durations of less than 2 µs and a maximum energy of 12 J. With the help of a reflection grating, the wavelength of the laser can be tuned in the range of 9-11 µm. To maximize the laser absorption in ammonia, the laser wavelength is tuned to one of the two absorption bands of ammonia, located at (10309-10352) nm and (10706-10729) nm. While this reduces the maximum beam energy to 5 J, it is compensated for by the better absorption in ammonia[Ols81a]. Reflected by two plane copper mirrors and a copper focusing mirror, the laser pulse passes a ZnSe window and enters the vacuum system perpendicular to the beam axis. The pepperpot mask, which is made of polished molybdenum, is mounted at a 45° angle to the beam axis and therefore reflects the laser along the axis into the chamber, where the beam is absorbed.

For short distances, the decrease of the the laser intensity is proportional to the intensity (I), the gas density (or, equivalently, the gas pressure p), the traversed distance dz and a factor κ:

$$dI = -\kappa \, p \, I \, dz \tag{3.23}$$

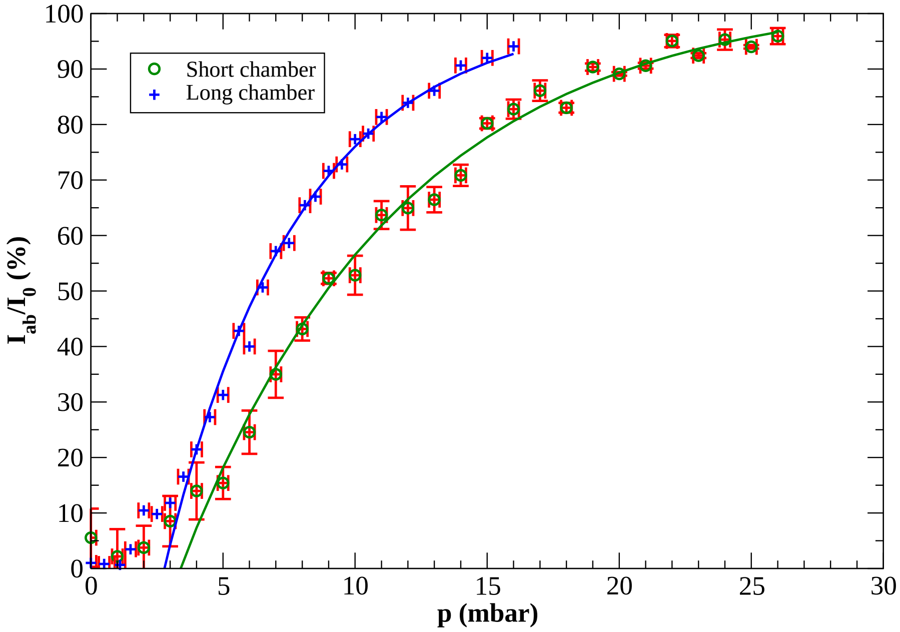

Figure 3.7.: Absorption measurements for the CO_2 laser in ammonia. Measurements for both the old, 50 cm long chamber[Nie02] and the new, 1 m long chamber are plotted.

If we assume that the absorption coefficient does not depend on the laser intensity, the intensity along the absorption path is

$$I(z) = I_0 \cdot \exp(-\kappa p z) \tag{3.24}$$

The relative absorption of the laser is therefore

$$\frac{I_{\text{ab}}}{I_0}(p,z) = \frac{I_0 - I(p,z)}{I_0} = 1 - \exp(-\kappa p z) \tag{3.25}$$

To measure the absorption, the transmission of the laser in the gas-filled chamber is compared to the transmission in the evacuated chamber. By this method, all losses due to the mirrors or the entrance window are eliminated from the calculation. Figure 3.7 shows the results of absorption measurements in ammonia for both the long and the short chamber. For pressures above 15 mbar, the laser is nearly totally absorbed in the long chamber. To compare the measurements with the theory, the data is fitted with the formula

$$\frac{I_{\text{ab}}}{I_0}(p,L) = \frac{I_0 - I(p,L)}{I_0} = a_0\,(1.0 - \exp\left[-a_1 \cdot (p - a_2)\right]) \tag{3.26}$$

where the pressure is measured in mbar. The length L is the total absorption length. It is the sum of the absorption length in the chamber, L_{ch}, and the path traversed between entering the pumping section through the germanium window and actually entering the chamber through the hollow anode. This path is approximately 30 cm long, so that the total absorption length is 80 cm for the short chamber and 130 cm for the long chamber. The parameter a_1 corresponds to $\kappa \cdot L$, whereas the parameters a_0 and a_2 take measurement errors into account.

Causes for errors are slight variations of the output energy of the laser and measurement errors of the laser detector (parameter a_0). Furthermore, there are uncertainties in the measurement of the gas pressure, due to impurities of the chamber gas and temperature variations. The fit parameters for the measurements in the short chamber are $a_0 = 1.04$, $a_1 = 0.12$, and $a_2 = 3.4$, the parameters for the measurements in the long chamber are $a_0 = 1.0$, $a_1 = 0.2$, and $a_2 = 2.8$. The absorption for low pressures is higher than expected. Pressures above 4 mbar agree well with the theory, provided that we shift the curve slightly, whereas the curve fails to fit the measurements at low pressures. This shift might be caused by uncertainties in the pressure measurements, which might be caused by the gas inlet that is near the pressure gauge. The ratio of the coefficients a_1 is consistent with the theoretical expectations ($a_1(\text{long})/a_1(\text{short}) = 1.3/0.8 \approx 2.0/1.2$), so that the absorption coefficient κ is identical, as expected. While the maximum absorption is at high pressures, it is nevertheless preferable to work at lower pressures (about 5 mbar for the long chamber) to get a homogeneous absorption profile along the chamber axis.

The initial temperature profile is calculated from the absorbed beam energy. The heat capacity of ammonia in the temperature range of 300 K to 2000 K is[Ger85]

$$C_p(T) = \left[1.478 + 2.094 \cdot 10^{-3} \frac{T}{\mathrm{K}} - 2.002 \cdot 10^{-7} \frac{T^2}{\mathrm{K}^2} - 8.079 \cdot 10^{-11} \frac{T^3}{\mathrm{K}^3}\right] \frac{\mathrm{kJ}}{58.82\,\mathrm{mol\ K}} \tag{3.27}$$

For temperatures above 2100 K ammonia starts to dissociate, which increases the specific heat and limits the maximum temperatures[Ols81a]. If we assume a Gaussian spatial profile of the laser intensity

$$I(r) = I_0 \cdot \exp\left[-\frac{r^2}{2\sigma_r^2}\right] \qquad \text{with} \quad I_0 = \frac{Q}{2\pi\sigma_r^2 L} \tag{3.28}$$

(Q: total pulse energy, L: absorption length) we get an integral equation for the absorbed energy

$$Q = \int dV n(\mathbf{x}) \int_{T_a}^{T_e(\mathbf{x})} C_V(T) dT = 2\pi L \frac{p_a}{R T_a} \int_0^\infty dr\, r \int_{T_a}^{T_e(r)} (C_p(T) - R) dT \tag{3.29}$$

Here n is the particle density, p_a the ambient gas pressure, T_a the ambient gas temperature and T_e the temperature immediately after the laser shot. If the radial temperature profile is also Gaussian

$$T_e(r) = T_a + T_0 \cdot \exp\left[-\frac{r^2}{2\sigma_r^2}\right] \tag{3.30}$$

the temperature increase T_0 can be calculated for a given pulse energy Q and radial width σ_r. Table 3.1 shows the calculated temperature profile for various laser parameters. These temperature profiles are the starting point for hydrodynamical simulations with CYCLOPS. It is a one-dimensional code that is able to calculate the rarefaction caused by the laser heating. The calculation assumes that the gas is heated instantaneously and starts therefore with a Gaussian temperature profile (Eqn. 3.30) and a homogeneous gas density in the channel. The parameters for the calculations are taken from Table 3.1, assuming a homogeneous absorption along the channel. As stated before, in reality the absorption is exponential and the laser

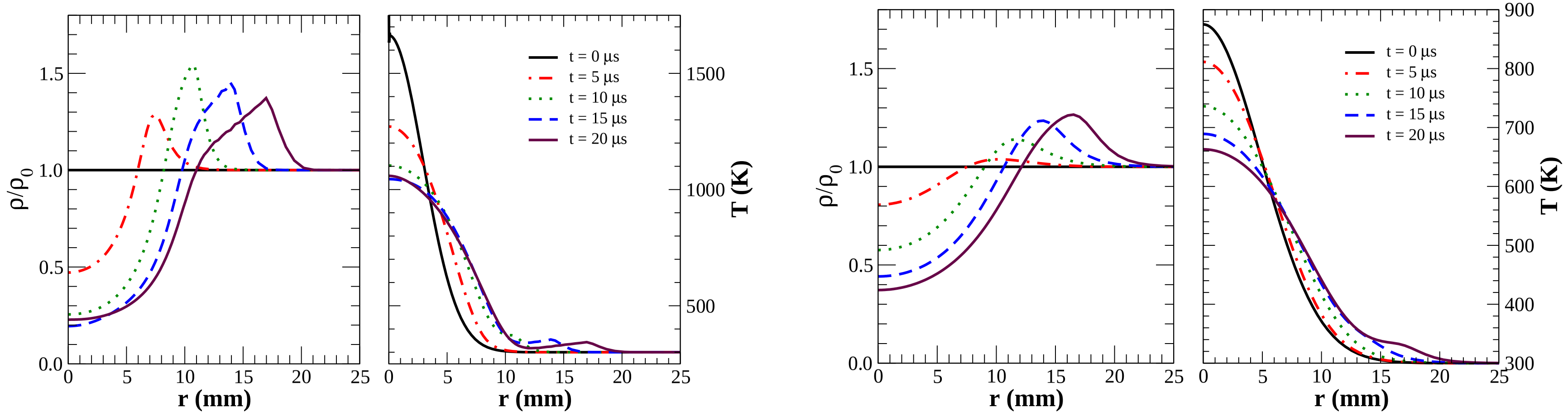

(a) Ammonia, 1 mbar, T_0 = 1365 K, σ_r = 3 mm

(b) Ammonia, 1 mbar, T_0 = 575 K, σ_r = 5 mm

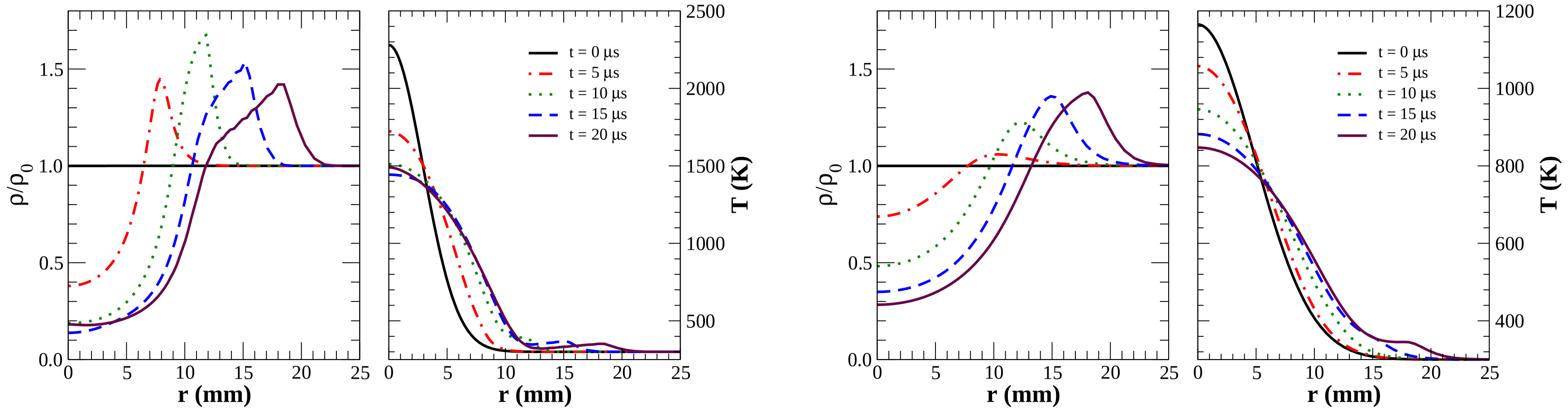

(c) Ammonia, 5 mbar, T_0 = 1980 K, σ_r = 3 mm

(d) Ammonia, 5 mbar, T_0 = 865 K, σ_r = 5 mm

Figure 3.8.: CYCLOPS calculations for laser heating in the long chamber. Calculations for four different sets of parameter are shown. The parameters for the initial temperature profile are taken from Table 3.1. For each set of parameters, the density and temperature profiles are plotted. Densities are plotted relative to the initial density.

	1 mbar, 0.15 J	5 mbar, 1.2 J	10 mbar, 2.25 J	15 mbar, 2.7 J
$\sigma_r = 3\,\mathrm{mm}$	$T_0 = 1365\,\mathrm{K}$	$T_0 = 1980\,\mathrm{K}$	$T_0 = 1890\,\mathrm{K}$	$T_0 = 1580\,\mathrm{K}$
$\sigma_r = 4\,\mathrm{mm}$	$T_0 = 845\,\mathrm{K}$	$T_0 = 1250\,\mathrm{K}$	$T_0 = 1190\,\mathrm{K}$	$T_0 = 990\,\mathrm{K}$
$\sigma_r = 5\,\mathrm{mm}$	$T_0 = 575\,\mathrm{K}$	$T_0 = 865\,\mathrm{K}$	$T_0 = 820\,\mathrm{K}$	$T_0 = 675\,\mathrm{K}$

Table 3.1.: Laser absorption in ammonia and resulting temperature profile for a 3 J laser pulse for various widths and at various gas pressures (1.3 m total absorption length). The calculated temperatures are averages over the whole absorption length.

parameter varies along the axis due to focusing. Nevertheless, the gradient of the absorption is sufficiently small to justify using a one-dimensional model and considering the result as the channel dynamics averaged over the whole length of the chamber. Figure 3.8 shows the results for four different sets of parameters. The plots show the gas density (as a fraction of the initial density) and the gas temperature at the beginning ($t = 0$) and after 5 µs, 10 µs, 15 µs, and 20 µs. The initial gas pressure ranges from 1mbar to 5mbar. The calculations show that a rarefaction channel develops in all cases. Its depth is strongly influenced by the laser diameter: the small beam triggers a rarefaction down to 20% of the initial density. In contrast, the wide beam only halves the density in the center, creating a wider, shallower channel. There is only a slight dependence on the initial gas density, since the laser absorption is nearly proportional to it in the considered density regime. The maximum rarefaction is reached after 10 µs and remains stable for more than 20 µs. The simulation results are consistent with gas density measurements[Nef03, Nef02].

3.3.3. Ion-beam initiation

The applicability of CO_2-laser heating is limited to ammonia. Efficient heating of other chamber gases requires the use of a short-pulse laser. Yet the UNILAC ion beam with its kinetic energy of 11.4 MeV/u is an alternative, since it ionizes the gas along its path, thereby removing the need for a short-pulse laser. Since the ion beam is needed for beam-transport measurements anyway, its use for ionizing the gas does not require any additional experimental effort.

The modelling of the ionization of the gas is complicated. Yet the energy loss of ions in gas can be calculated with SRIM[Zie85], a semi-empirical code based on energy loss measurements. This energy loss per ion gives an upper limit on the free electrons that can be created by an ion, depending on the ionization energy of the gas. These calculations show that an beam on average deposits an energy of 8-30 MeV, depending on the gas species, traversing 1 m ($p = 1$ mbar). If the total energy was used for ionization, this would result in up to 10^6 free electrons per beam ion (see also Table 2.2). Of course the real number is lower, since parts of the deposited energy end up in kinetic energy or excitations. Nevertheless, the ion beam is able to guide the discharge.

This ionization must take place before the start of the prepulse. Since the beam pulse has typical lengths of around 100 µs, this is no problem. The prepulse is simply delayed some microseconds after the beginning of the beam pulse. The downside of ion-beam initiation is that it can only be used during beamtimes and is therefore not suited to test the experimental

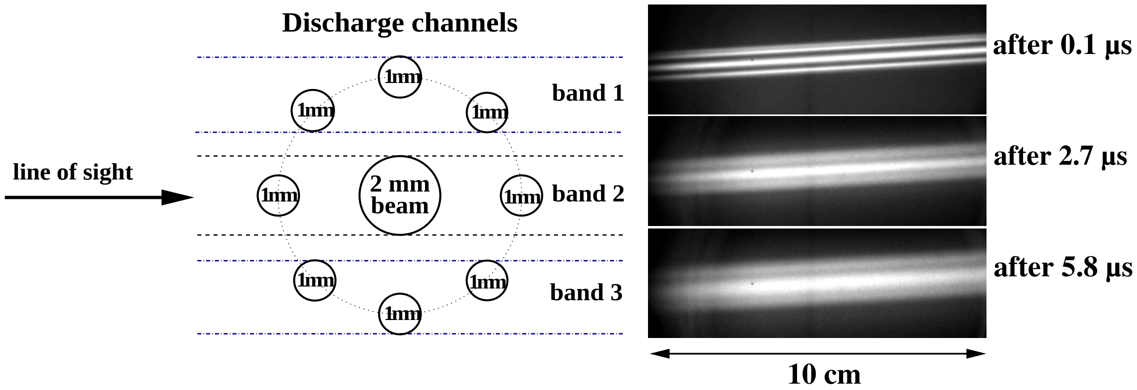

Figure 3.9.: Formation of multiple channels after ionization using a pepperpot mask. The beam is shaped into nine beamlets, as shown on the left. The pictures on the right show the discharge at three different times. The discharges were created without a prepulse, which smooths out the channel.

setup or to study the channel dynamics outside of beamtimes. On the other hand, this approach allows to study other gases, like xenon or krypton, which absorb only a small percentage of the carbon-dioxide laser. This removes the restriction of using ammonia as a chamber gas and allows us to test gases which are more suitable for a fusion reactor concept. Ion-beam initiation has been successfully applied. Photographs show that the discharge path strictly follows the path of the initial ionization. This is illustrated in Figure 3.9. For this measurement, no prepulse was employed and a special pepperpot mask was used which divides the beam into nine separate beamlets, as indicated in the left picture. The right picture shows a lateral view of the central part of the discharge channel. The first photograph is taken 0.1 µs after the beginning of the discharge and clearly shows three ‘stripes’, the central one being thicker than the outer ones. The cause of this pattern is indicated in the schematic drawing on the left: due to the lateral perspective, each of the three ‘stripes’is the superposition of three channels, the central one being bigger due to the large channel in the center. The photographs show that the channels expand and merge into one channel at later times.

Obviously, this initiation method would be of little use for our beam transport studies if we had to deal with several separated channels. Yet the prepulse, which is triggered 10 µs before the main discharge, smooths out the channels, so that we can create a homogeneous channel for our transport measurements.

3.3.4. Prepulse

After the channel initiation, either by laser heating or by ionization, the second step of channel creation, the prepulse, takes place. The purpose of the prepulse is to create, or in the case of laser heating enhance, a rarefaction channel along the axis that is surrounded by a wall of increased gas density. Such a gas density profile stabilizes the subsequent main discharge against kink instabilities[Man73]. The prepulse is therefore not strictly necessary for creating a channel, but improves its stability.

In order to damp the oscillations of the discharge, a 5 Ω resistor is connected in series with the prepulse generator. This limits the duration of the prepulse to less than 2 µs. During the discharge, the gas is heated on the axis, and afterwards it expands radially, creating the rarefaction. Due to the numerous physical processes taking place in the prepulse, it is too complex to be solved analytically. To get a qualitative understanding of the channel dynamics during the prepulse, it is simulated with CYCLOPS. For a description of the model used in Cyclops see Apendix C. Naturally, the results of the simulation must not be taken to be numerically exact, as it uses various approximations, among them the assumption of perfect cylindrical symmetry during the whole process.

The starting point of the simulation is the final result of the laser-heating simulation described in Section 3.3.2. The following simulation studies a 25 kV prepulse in 5 mbar of ammonia and starts with the rarefaction channel created by a laser pulse with 3 mm width (see Figure 3.8c). The simulation lasts 10 µs. The results of the simulation are shown in Figure 3.10 and Figure 3.11. The discharge current reaches its maximum of 3 kA after 0.4 µs (see Figure 3.11b). The oscillations of the discharge current are efficiently damped by the 5 Ω resistor that is connected in series; the capacitor is therefore fully discharged after 2 µs.

The simulation includes both the discharge and the subsequent expansion of the gas. The discharge leads to a pinching of gas (see Figure 3.10a), resulting in a 10-fold increased mass density on axis. After the current has subsided, the gas expands outwards, deepening the rarefaction channel and steepening its edge. After 10 µs, the gas density at the center has dropped to 10 % of the initial density. The rarefaction channel has a width of roughly 15 mm and is surrounded by a flank of twice the initial gas density.

Figure 3.10b shows the development of the electron density. The simulation starts with a non-zero initial electron density to guarantee the numerical stability of the algorithms. As long as the initial electron density is well below the electron densities encountered during the discharge and sufficiently high to avoid numerical errors, the initial density does not influence the final values in the channel. The calculation starts with an initial electron density of $10^{12}\,\mathrm{m}^{-3}$. At the time of the current maximum, the electron density reaches $10^{23}\,\mathrm{m}^{-3}$. These high densities are not reached in the whole rarefaction channel, but only in the innermost section with a radius of 2 mm. Outside this region, the electron density drops rapidly and finally reaches its initial value. After the discharge is over, the electron density spreads outwards, reaching a final radius of 5 mm and a maximum density of $10^{22}\,\mathrm{m}^{-3}$. It should be noted here that the simulation run does not take recombination effects into account, since no proper parameters for the hydrogen-nitrogen mixture are known, so that in reality the final electron density should be lower.

The temperature profile is shown in Figure 3.10c. After reaching a maximum of 18,000 K at the time of the current maximum, the temperature decreases to 6,000 K at the end of the simulation. The maximum of the temperature is initially slightly off-axis, as the density there is lower, resulting in a higher energy per ion and electron. After the end of the discharge, the profile smooths out, resulting in a rather flat profile with its maximum on the axis. At the border of the channel, the temperature reaches the ambient temperature of 300 K.

Figure 3.10d shows the conductivity of the channel. CYCLOPS uses the Drude conductivity

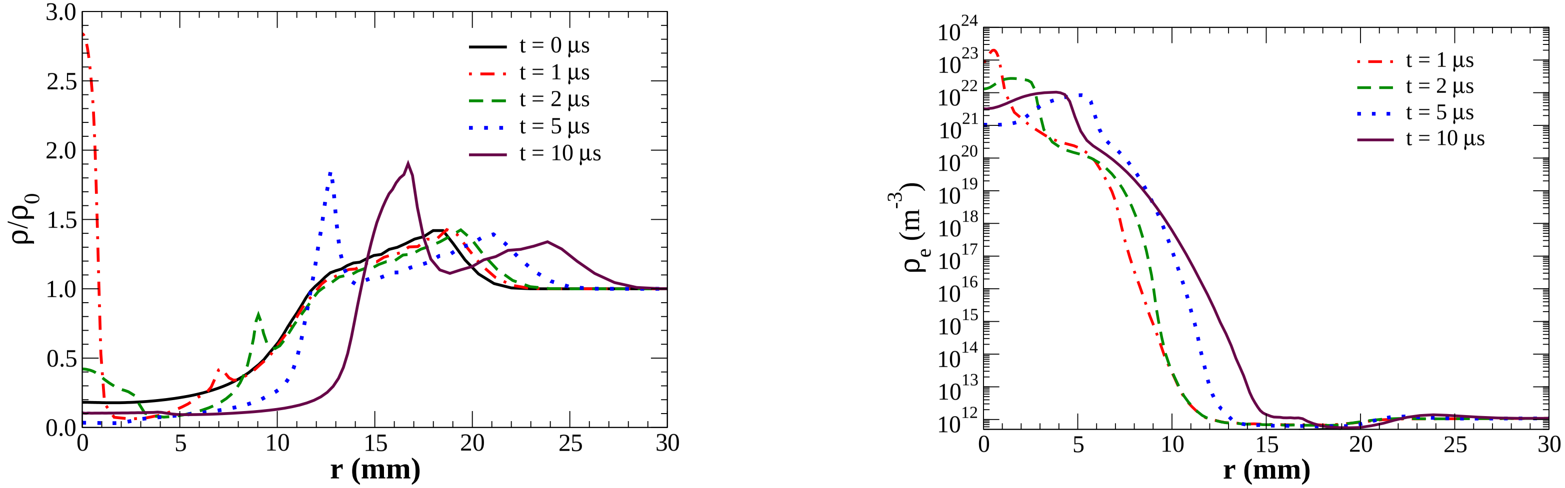

(a) Mass density of the gas, relative to ambient density

(b) Electron density

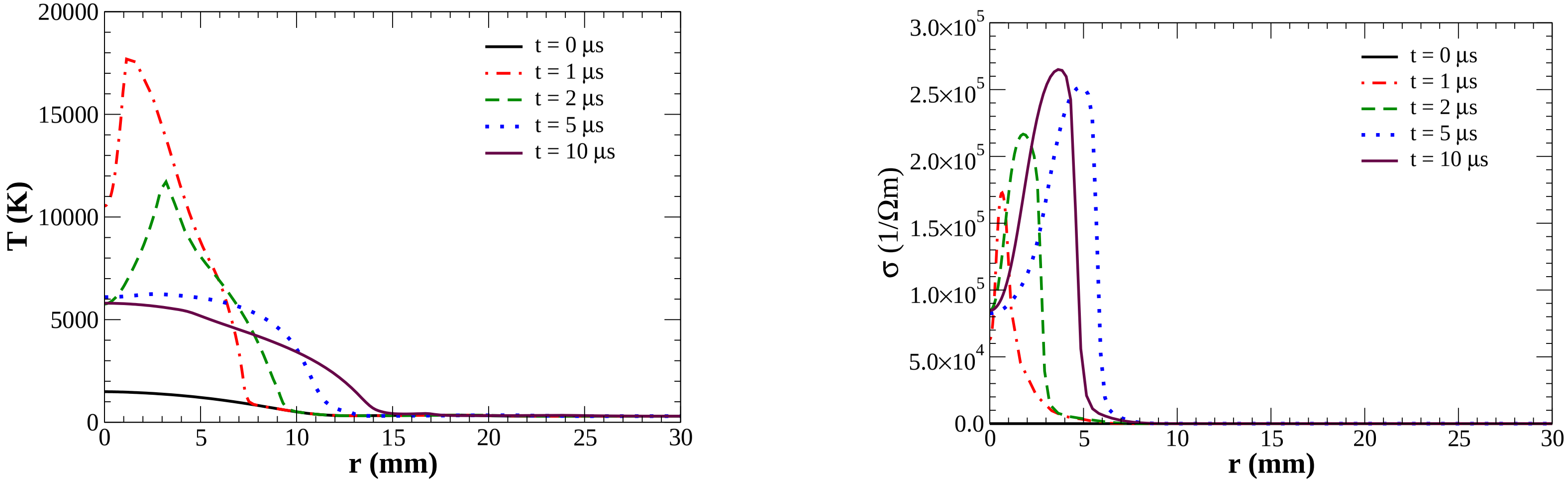

(c) Temperature

(d) Conductivity

Figure 3.10.: CYCLOPS calculations for a 25 kV prepulse in 5 mbar ammonia. The starting point of this simulation is the result of the calculation depicted in Figure 3.8c.

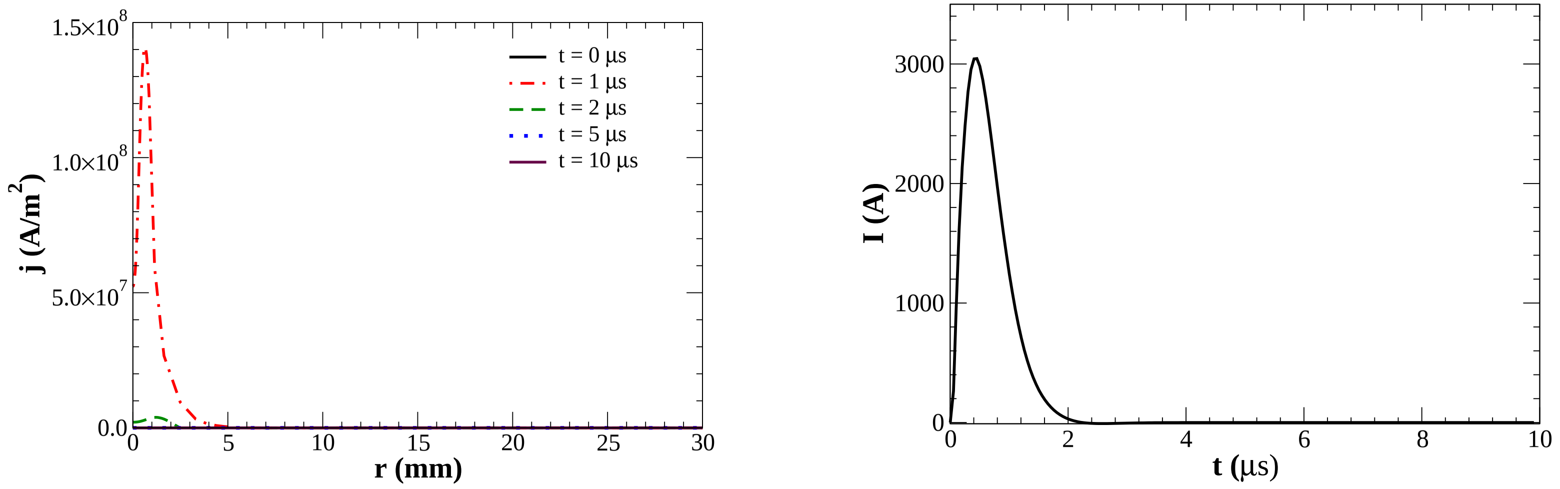

(a) Current density

(b) Discharge current

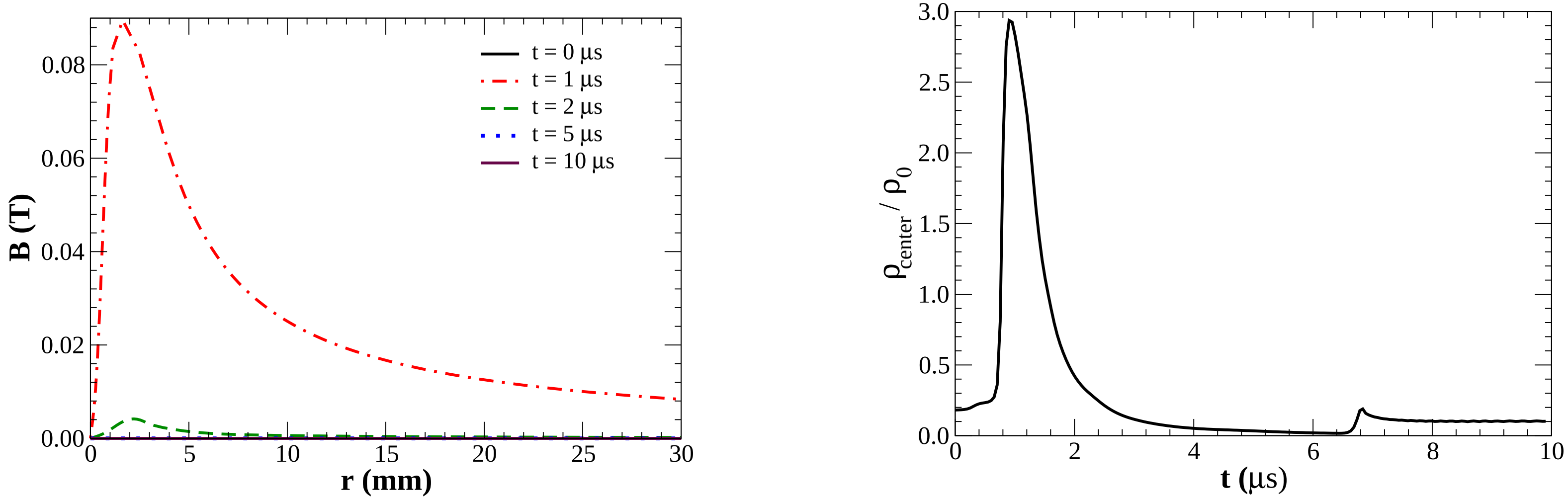

(c) Magnetic field

(d) Density at center, relative to ambient density

Figure 3.11.: CYCLOPS calculations for a 25 kV prepulse in 5 mbar ammonia. The starting point of this simulation is the result of the calculation depicted in Figure 3.8c.

model[Lib90]

$$\sigma = e n_e \mu = \frac{e^2 n_e}{m_e \nu_{\mathrm{coll}}} \tag{3.31}$$

where e is the electron charge, n_e the electron density, μ the mobility, m_e the mass of the electron, and ν_{coll} the collision frequency. The collision frequency is estimated with an empirical formula. Since the conductivity is proportional to the electron density, the maximum conductivity is also slightly off-center. The maximum conductivity is reached at the end of the simulation, since the collision frequency decreases with decreasing temperature, thereby compensating the reduction of the electron density.

The current density and the magnetic field are shown in Figure 3.11a and Figure 3.11c, respectively. The total current of 3 kA is distributed over a channel of roughly 2 mm radius, resulting in a current density of nearly $1.5 \cdot 10^8\,\mathrm{A/m^2}$. This current creates a maximum magnetic field of 0.09 T. Naturally, the current density and the magnetic field drop to zero after the end of the discharge.

3.3.5. Main discharge

After the prepulse and the subsequent expansion phase is completed, the main discharge is triggered. The delay between the triggering of the prepulse and the triggering of the main discharge is between 5 µs and 20 µs. If the delay between prepulse and main discharge is shorter, the timing of the main discharge becomes unreliable. As before, the channel dynamics is illustrated with a CYCLOPS simulation run. One should keep in mind that CYCLOPS makes several approximations, so that its results should be interpreted qualitatively and not be taken as quantitatively exact. Due to numerical instabilities of the simulation code, the heat radiation was neglected in the calculation. This results in temperatures which are systematically too high, which in turn leads to a conductivity and a discharge current which are too high.

The simulation starts with the final results of the prepulse simulation. The main capacitor bank is charged to a voltage of 20 kV. The results of the calculations are shown in Figure 3.12 and Figure 3.13. The spatially resolved quantities (gas density, electron density, temperature, conductivity, current density, and magnetic field) are plotted for five times, ranging from $t = 0$ to $t = 4\,\mu\mathrm{s}$, whereas the current and the density at the center are plotted continuously from $t = 0$ to $t = 5\,\mu\mathrm{s}$. The simulation was limited to this time span, since the simulation became numerically unstable for later times. The discharge current (Figure 3.13b) reaches a maximum of nearly 50 kA, which is twice as large as the measured current. The maximum current is reached after 4.5 µs, whereas in reality the maximum is reached after 6 µs (see Figure 4.4).

The evolution of the mass density is plotted in Figure 3.12a. At the beginning, an inner section, which is roughly 2.5 cm in diameter, is nearly cleared from ammonia, and surrounded by a wall of doubled gas density, which separates the rarefaction channel from the ambient gas. The discharge leads to a pinching of the gas on the axis, resulting in a density profile with its peak on the symmetry axis. According to the simulation, the density on axis is eight times the ambient gas density and the diameter of this peak is roughly 5 mm. The pinching on axis leads to an additional rarefaction wave, resulting in a ‘blanket’ of cold gas travelling outwards. Figure 3.12c shows the evolution of the temperature profile. The profile is peaked at the boundary of the pinched gas and reaches a maximum of roughly 16 eV. For greater radii, the temperature falls gradually until it reaches the ambient gas temperature of 300 K at the border of the channel.

The electron density (Figure 3.12b) is peaked on the axis and reaches a maximum of $10^{24}\,1/\mathrm{m}^3$. Outside the pinched gas, the electron density is nearly constant at $10^{22}\,1/\mathrm{m}^3$. Both limits are in the range of electron densities measured at the old experimental setup. Figure 3.12d shows the conductivity in the channel. CYCLOPS uses an empirical model for the collision frequency which takes both the gas density and the electron density into account, so that the density dependence is more complicated than in Equation (A.3). The conductivity of the channel is nearly constant along the channel and stays approximately constant at $1.5 \cdot 10^5\,1/\Omega\mathrm{m}$. The width of this profile is a little bit smaller than the width of the electron density profile. The current density is peaked on the axis and reaches a maximum of $3.6 \cdot 10^8\,\mathrm{A/m}^2$ (Figure 3.13a). The current density in the outer regions of the channel is roughly $0.5 \cdot 10^8\,\mathrm{A/m}^2$. Due to this current density profile, the magnetic field is no longer linear, but consists of two roughly linear sections (Figure 3.13c). In the next chapter, the simulation results are compared with measurements.

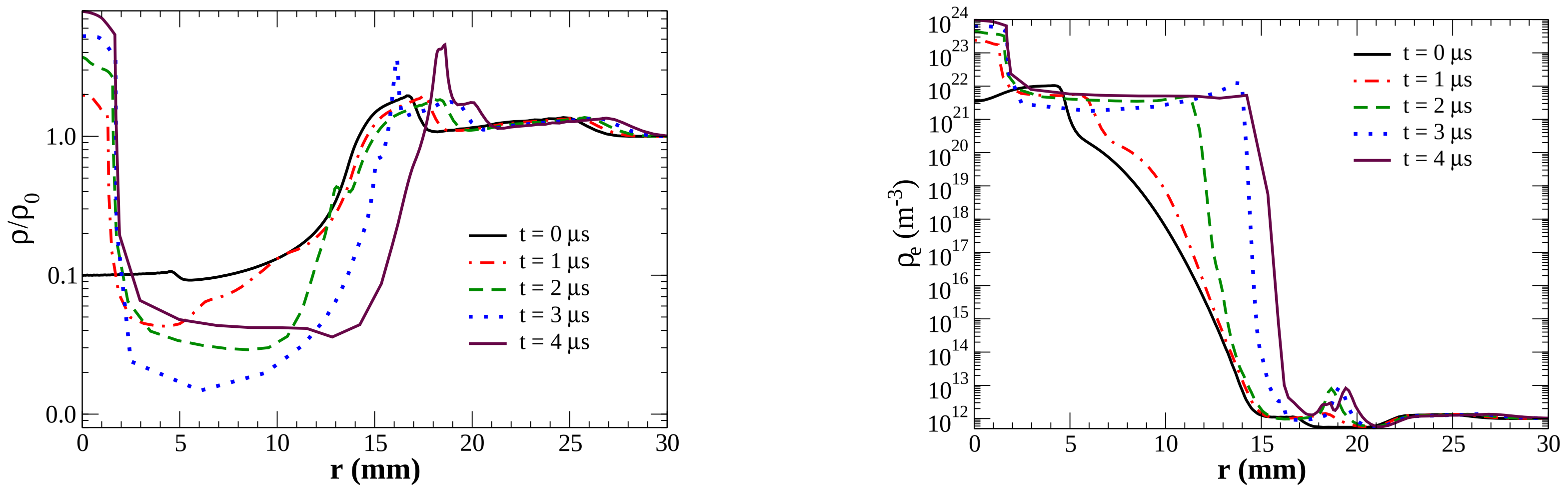

(a) Gas density, relative to ambient density

(b) Electron density

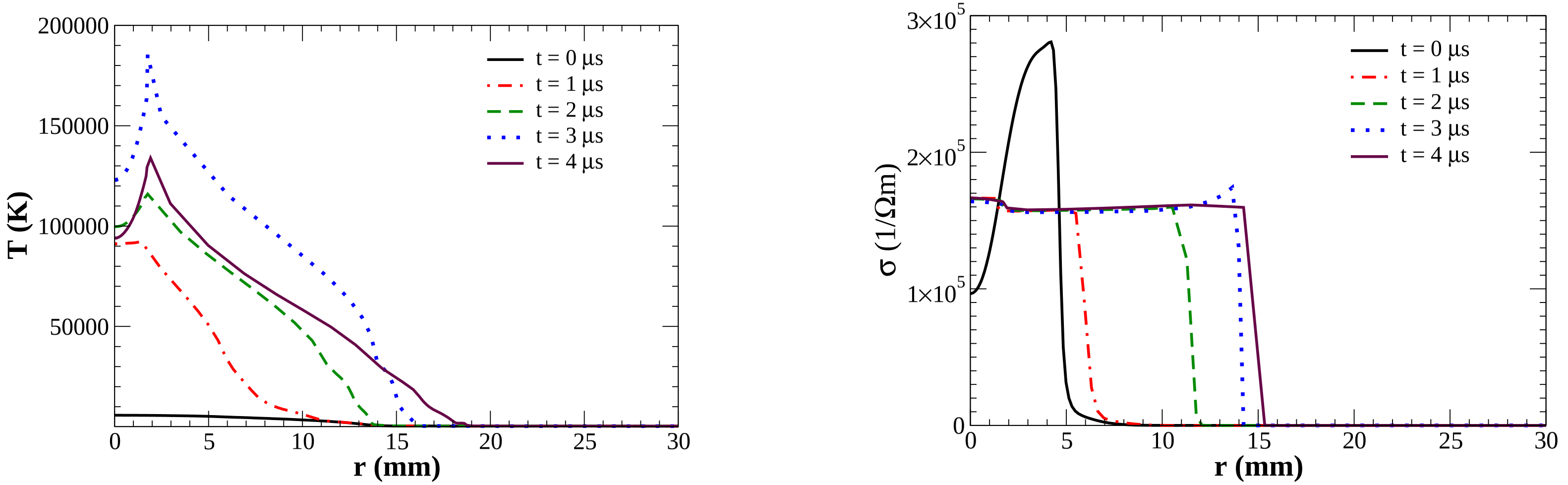

(c) Temperature

(d) Conductivity

Figure 3.12.: CYCLOPS calculations for a 20 kV main discharge in 5 mbar ammonia. The starting point of this simulation is the result of the prepulse simulation.

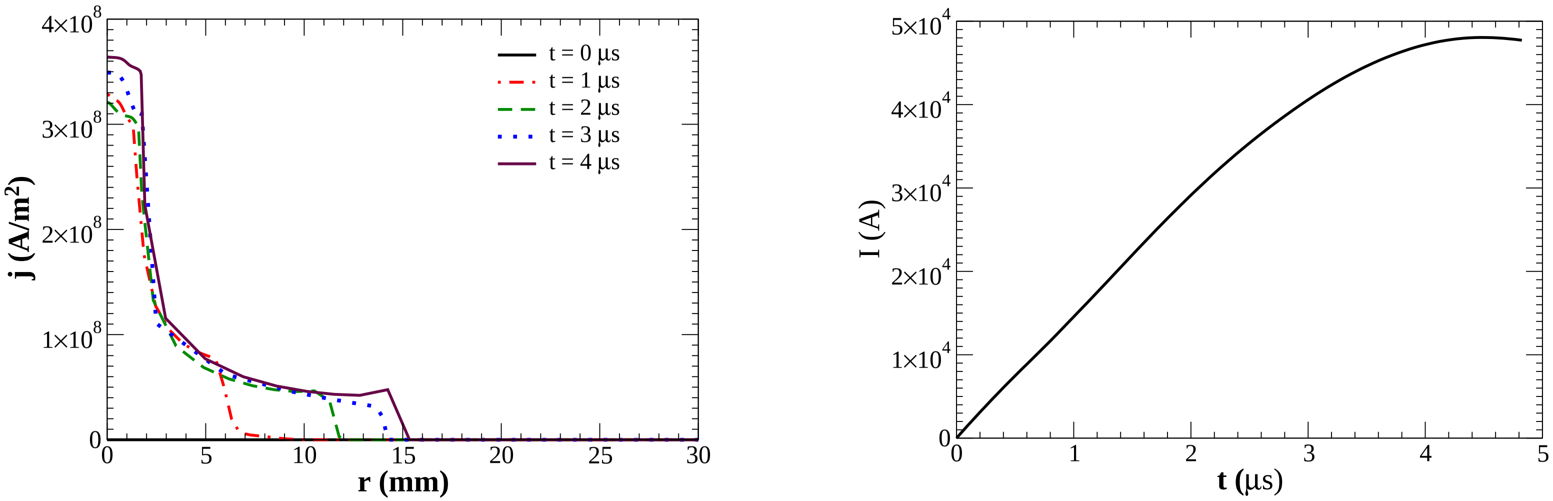

(a) Current density

(b) Discharge current

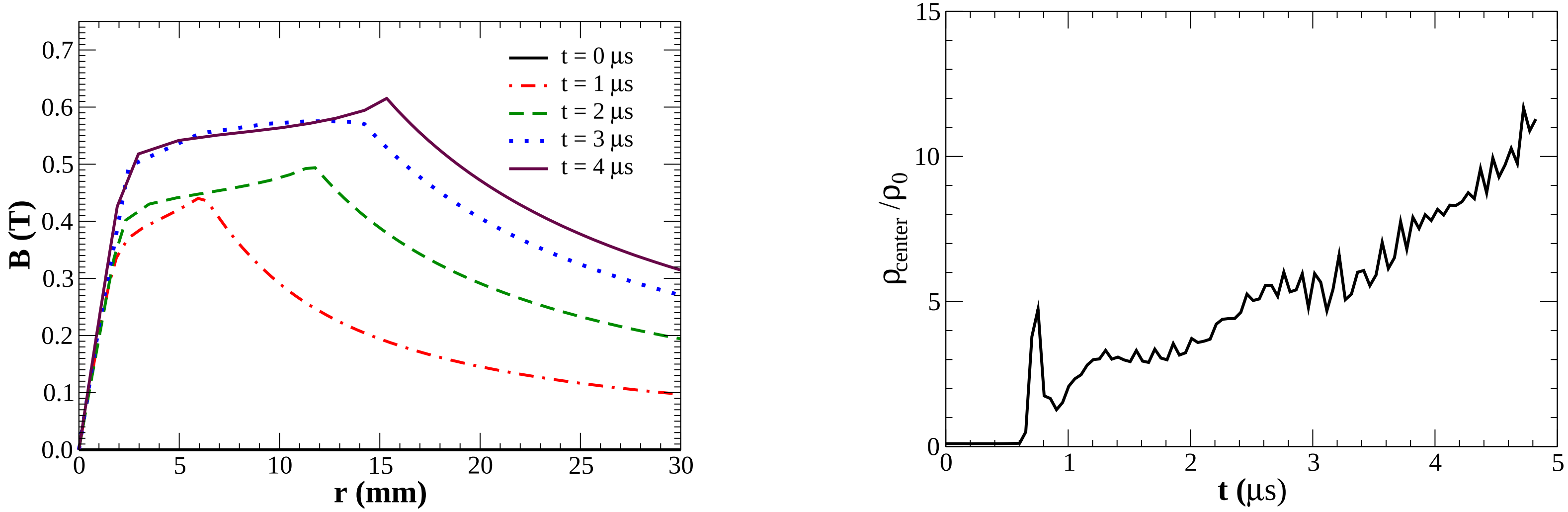

(c) Magnetic field

(d) Density at center, relative to ambient density

Figure 3.13.: CYCLOPS calculations for a 20 kV main discharge in 5 mbar ammonia. The starting point of this simulation is the result of the previous prepulse simulations.

4. Measurements

The experiment is located at the *Gesellschaft für Schwerionenforschung* and uses ion beams from the 'Universal Linear Accelerator' (UNILAC). The accelerator can provide a wide range of ions with energies up to 11.4 MeV/u and electric beam currents of up to 1 mA.

Figure 4.1 shows the experimental setup during a beamtime. The discharge chamber is mounted inside a Faraday cage, which shields the cameras and the laser from the rf-noise generated by the high-current discharge in the chamber. The beam of the carbon-dioxide laser on the right is directed by a set of plane mirrors and a focusing mirror onto the pepperpot mask, which is mounted in the beamline at the back side of the chamber. Also shown are the prepulse generator and the main generator. Three cameras are used to analyze the channel dynamics and the beam transport properties. One camera (PCO DicamPro) is mounted on the beam axis to take images of the scintillator mounted inside the cathode. Another DicamPro camera takes pictures of the central section of the discharge via a mirror and a window in the chamber. Both DicamPro cameras have an image resolution of 1280×1024 pixels. On the opposite side a framing camera (DRS Hadland Ultra) is mounted to take image series of the discharge evolution. While its optical resolution of 520×520 pixel is worse than that of a DicamPro camera, its ability to take eight consecutive pictures during one discharge make it essential for the study of instabilities, which by their very nature are not reproducible. The relative timing of the pictures is arbitrary, as long as their exposures do not overlap. A disadvantage of the framing camera is that it requires more light than the DicamPro cameras for a sufficient exposure of the images. This rules out its use for taking series of scintillator images, yet the light emitted by the discharge is more than sufficient for using the framing camera. For images of the discharge channels minimum exposure times of 10 ns were used with both cameras, whereas the scintillator images required an exposure time of 0.5 µs. The timing of the cameras is controlled with computer programs and is checked by comparing the timing signal of the cameras with the current profile of the discharge. The optical diagnostics are supplemented by the measurement of the total discharge current and of the current that flows through the voltage divider.

As the purpose of the experiments is to demonstrate successful beam transport in the prolongated chamber, the experiments can be divided in three major groups: determining the pressure range for channel creation, studying the stability of the discharge, and determining the beam transport properties of the channel. First measurements show that the channel causes no significant increase of the beam emittance (for further information see [Kno04]). Typical channel properties, such as electron temperature, electron density, and magnetic field, had already been measured with the old experimental setup[Nie03b, Nie02, Nie03c, Nie01, Nef02, Pen02c]. Doubling the channel length has little effect on the channel parameters, so the results of the measurements at the old chamber still hold. The measurements used both laser-initiated channels in ammonia and ion-beam-initiated channels in various other gases, most importantly

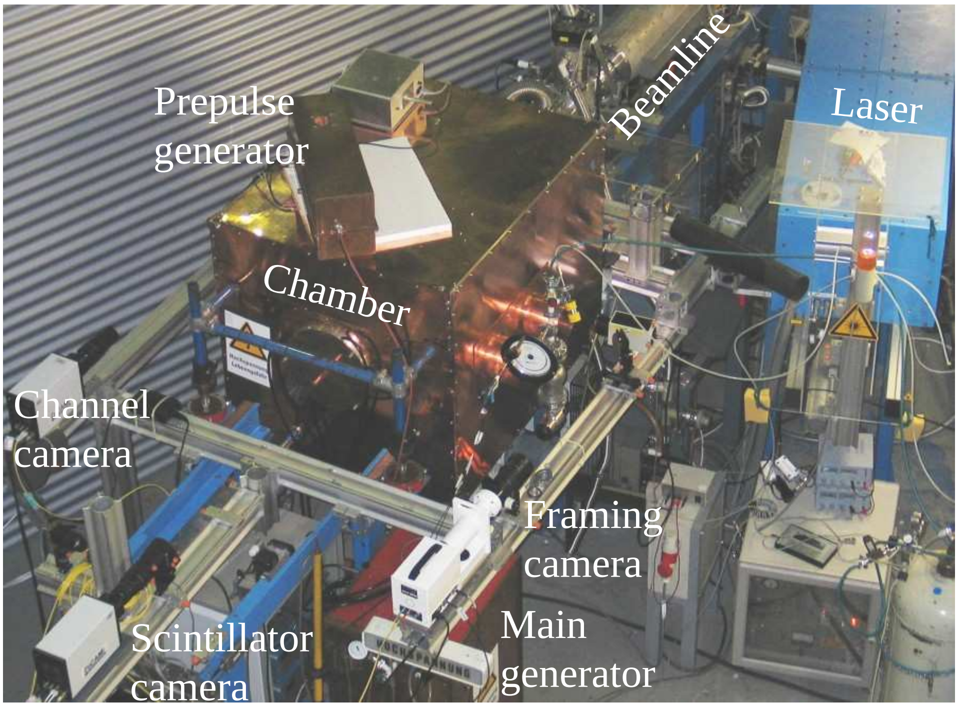

Figure 4.1.: A photograph of the experimental setup. The chamber is mounted inside a Faraday cage.

krypton and xenon. Channels were also created in nitrogen, neon, and argon, but the channel quality was better in the aforementioned two gases (that is the probability of breakdowns to the walls was lower), so that the measurements focused on these gases. The reason for this is probably the larger energy loss of the beam ions in xenon and krypton (see Table 2.2) in comparison to the other gases. In combination with their low ionization energy, this results in a high degree of ionization, which guides the subsequent discharge efficiently along the axis. As the chamber geometry is fixed, two free parameters for the discharge remain: the initial gas density in the chamber and the magnitude of the voltage applied at the electrodes.

In krypton channels were created for pressures between 0.5 mbar and 1.2 mbar and in xenon in the pressure range from 0.5 mbar to 1.0 mbar. Figure 4.2 shows the breakdown measurement in ammonia. These measurements used only the prepulse. As indicated in the graph, discharge channels can be initiated for pressures between roughly 1 mbar and 10 mbar. In this region, the breakdown voltages increases linearly with the gas pressure, which is in accordance with the Paschen curve. Channels can also be created at pressures higher than 10 mbar with the main pulse generator, but the discharge shows then a varying delay from the time of the trigger pulse and gets unstable (see also Section 4.2). A more detailed description of the operating regime is given in [Kno04]).

The measurement of the discharge current yields an estimate of the current density inside the channel (and thereby the magnetic field of the channel) and the relative timing of the discharge and the cameras and other diagnostics. The situation is depicted in Figure 4.3, in which the discharge current and the monitor signals of the scintillator camera and the side-

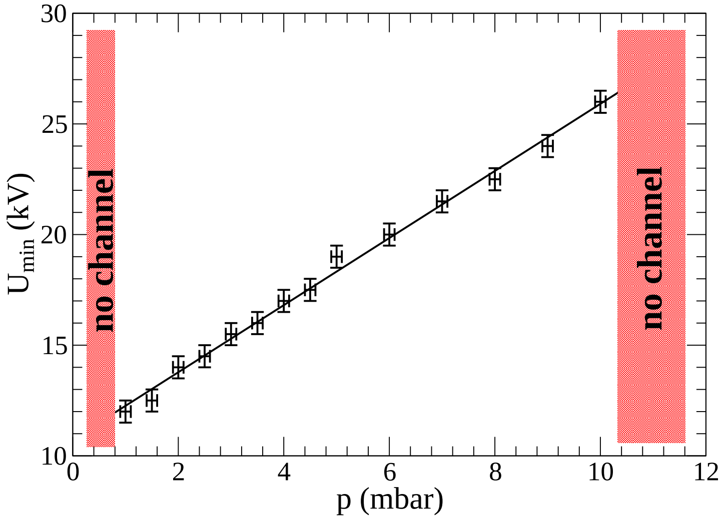

Figure 4.2.: Minimum voltages for channel creation in ammonia in the extended chamber. The measurements used only the prepulse and the carbon-dioxide laser.

view camera are plotted. The monitor signal lasts over the whole exposure time, in the case of the scintillator camera 1 µs and in the case of the side-view camera 10 ns. After determining the start of the discharge (marked by a blue bar), the timing of both cameras can be determined from the oscilloscope data. Provided that the channel is stable, the discharge can be repeated under identical conditions with a varied timing of the cameras and these measurements can be combined to a time series of the channel evolution.

The magnitude of the discharge current has a large influence on the channel dynamics. A reliable measurement of the discharge current is therefore necessary. The measurements originally used a 1 mΩ shunt to measure the discharge current, but the discharge currents were suspiciously high. Therefore the current shunt was replaced by a calibrated current transformer for a more accurate measurement of the discharge current.

One current transformer with a sensitivity of 1 mV/A (Pearson current monitor 5664) measured the total discharge current in the generator, while a second transformer with a sensitivity of 10 mV/A (Pearson current monitor 4160) measured the current passing the voltage divider. The current passing the discharge chamber is the difference between the total current and the current through the voltage divider.

Figure 4.4 shows a measurement for a 20 kV discharge in 4.5 mbar ammonia. The discharge current reaches a maximum of 25 kA after 6.2 µs, whereas the current through the voltage divider reaches its maximum of 1.3 kA directly after the triggering of the discharge, when the resistance of the channel is still high. Apart from this early stage, the current through the voltage divider is only a small fraction of the total current, typically a few percent. As indicated in Figure 4.4, the current in the voltage divider and the channel can actually flow in opposite directions. This can be explained by applying Kirchhoff's loop rule to our setup, in which the voltage divider with its resistance R_{vd} is connected in parallel to the discharge

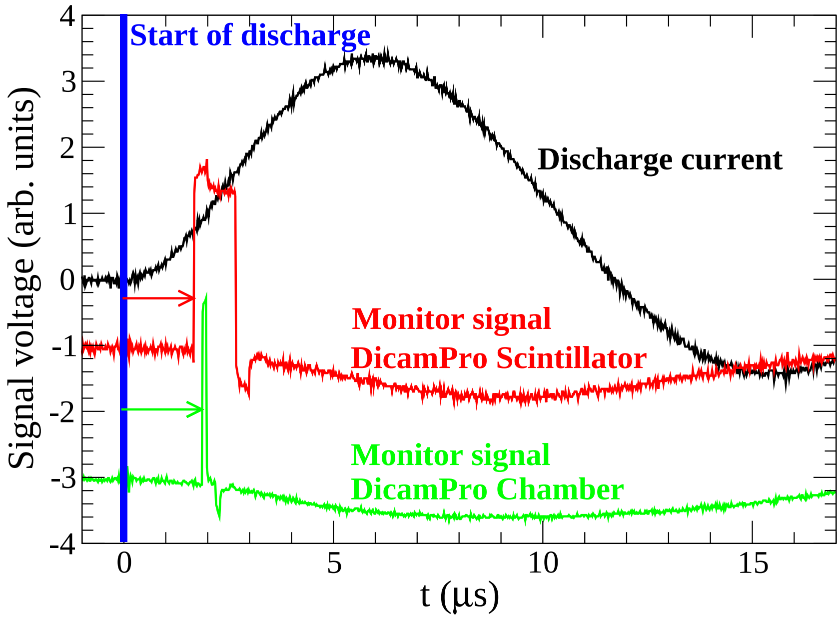

Figure 4.3.: Measurement of the relative timing of the cameras. Plotted are the discharge current and two camera signals.

channel with resistance R_{ch} and inductance L_{ch}. Therefore the relation

$$I_{\mathrm{vd}} = \frac{1}{R_{\mathrm{vd}}} \cdot \left(I_{\mathrm{ch}} \cdot R_{\mathrm{ch}} + L_{\mathrm{ch}} \cdot \frac{dI_{\mathrm{ch}}}{dt} \right) \tag{4.1}$$

holds, where I_{ch} is the current through the channel and I_{vd} the current through the voltage divider. After the current maximum, the second term in the bracket becomes negative and eventually the bracket turns negative, resulting in a current flowing in the opposite direction of the discharge current.

In order to check the phase lag between the total current and the current through the voltage divider, the current curves are calculated with a simplified model for the channel resistance. The simulations with CYCLOPS suggest that the final channel conductivity is reached within the first microsecond. Thus the conductivity essentially switches from the value for a cold gas (σ_0) to the plasma conductivity ($\sigma_{\max}$). In order to avoid discontinuities which arise from the use of a step function, the switching processes is modelled by

$$\sigma(t) = (\sigma_{\max} - \sigma_0) \cdot \left(1 - \frac{1}{\exp\left[\alpha \cdot (t - t_0)\right] + 1} \right) + \sigma_0 \tag{4.2}$$

This function switches between σ_0 and $\sigma_{\max}$ and reaches the average $(\sigma_0 + \sigma_{\max})/2$ for $t = t_0$. The steepness of the curve is determined by the parameter α. The resistance of the channel is therefore also time dependent and is given by

$$R_{\mathrm{ch}} = \frac{4L}{\sigma(t) \cdot \pi D_{\mathrm{ch}}^2} \tag{4.3}$$

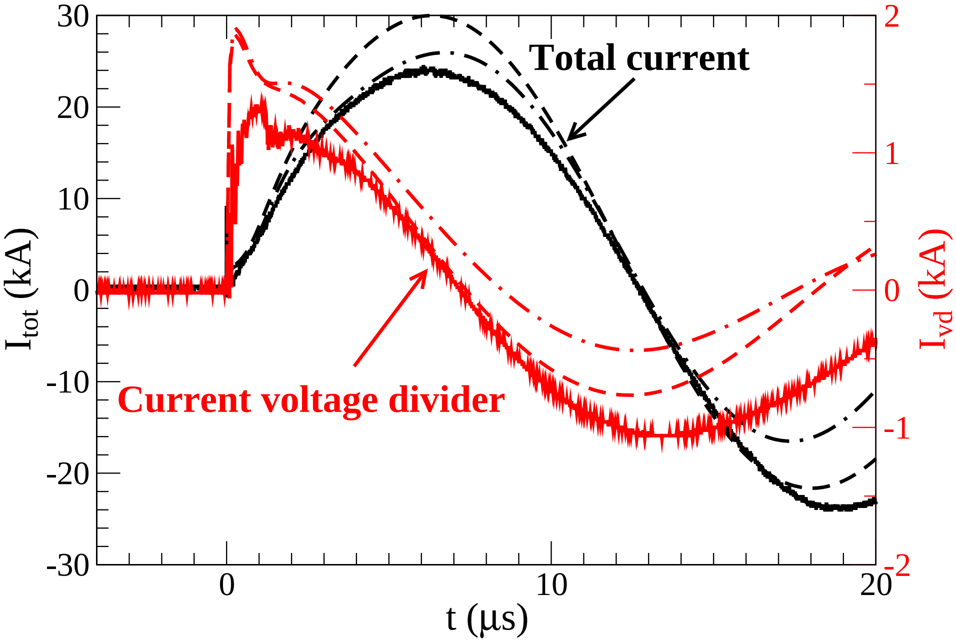

Figure 4.4.: Total discharge current and current passing the voltage divider for a 20 kV discharge. Plotted are measured currents for a discharge in 4.5 mbar ammonia (solid lines) and curves calculated with the model described in the text for two sets of parameters: $\sigma_{\text{max}} = 10^4/\Omega\text{m}$, $L_{\text{ch}} = 1100\,\text{nH}$ (dashed lines) and $\sigma_{\text{max}} = 5 \cdot 10^3/\Omega\text{m}$, $L_{\text{ch}} = 700\,\text{nH}$ (dash-dotted lines).

where L is the channel length and D_{ch} is the channel diameter. The circuit is modelled in detail (see Figure 4.5). The main capacitor bank and the cables are represented by a resistor, a capacitor, and an inductance connected in series (their parameters are given in [Pen02c]). The voltage divider acts as a resistor. Its capacitance is negligible, and since through it is small, its inductance is less important than the channel inductance and is therefore neglected to simplify the modelling. The plasma channel in the discharge chamber is represented by a resistor and an inductance, as derived in the previous chapter. The differential equation describing the circuit is obtained by Kirchhoff's rules. Combining them yields

$$\begin{aligned} Q \cdot \left(\frac{1}{C} + \frac{R_{\text{ch}}}{R_{\text{VD}} \cdot C} \right) + \frac{dQ}{dt} \cdot \left(R_{\text{cables}} + \frac{R_{\text{ch}} \cdot R_{\text{cables}}}{R_{\text{VD}}} + R_{\text{ch}} + \frac{L_{\text{ch}}}{R_{\text{VD}} \cdot C} \right) \\ + \frac{d^2Q}{dt^2} \cdot \left(L_{\text{cables}} + \frac{R_{\text{ch}} \cdot L_{\text{cables}}}{R_{\text{VD}}} + \frac{L_{\text{ch}} \cdot R_{\text{cables}}}{R_{\text{VD}}} + L_{\text{ch}} \right) + \frac{d^3Q}{dt^3} \left(\frac{L_{\text{ch}} \cdot L_{\text{cables}}}{R_{\text{VD}}} \right) = 0 \end{aligned} \tag{4.4}$$

where $Q(t)$ is the capacitor charge. To yield a solution, three initial conditions are required. The first condition is the initial capacitor charge, that is

$$Q(t = 0) = C \cdot U_0 = Q_0 \tag{4.5}$$

where U_0 is the charging voltage. Secondly, the initial discharge current is zero

$$\dot{Q}(t = 0) = 0 \tag{4.6}$$

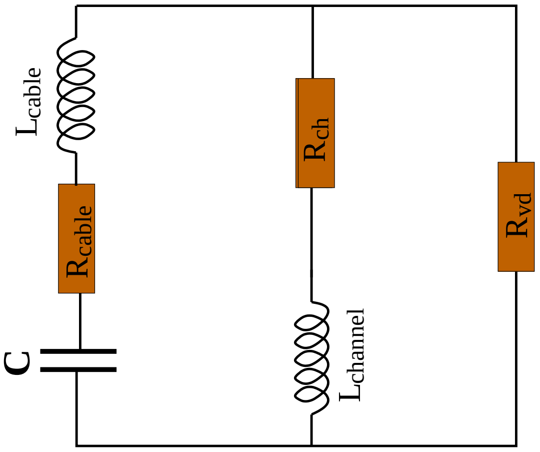

Figure 4.5.: Schematic of the simulated discharge circuit. The capacitor bank and the cables are represented by a RLC series.

Thirdly, the current passing the channel must also be zero. This implies

$$\frac{d^2Q}{dt^2}(t=0) = -\frac{Q_0}{L_{\text{cables}} \cdot C} \tag{4.7}$$

The problem is thus completely specified and can be solved numerically with Mathematica, a mathematical software package. The calculation simulates a 20 kV discharge in ammonia. In Equation 4.2, the initial conductivity of the channel σ_0 is 100/Ωm and the final conductivity is adjusted to fit the measured currents. The parameter t_0 is taken as 1 µs and the parameter α as $5 \cdot 10^6$/s. The maximum conductivity is reached after roughly 2 µs.

The calculation also takes the channel expansion into account. The time-dependent channel radius r_{ch} is calculated from a quadratic fit to measured data, in this case taken as

$$r_{\text{ch}}(t) = 0.74\,\text{cm} - 9.6 \cdot 10^{-3}\frac{\text{cm}}{\mu\text{s}} \cdot t + 2.93 \cdot 10^{-2}\frac{\text{cm}}{(\mu\text{s})^2} \cdot t^2 \tag{4.8}$$

Based on this model, the resistance of the channel is calculated according to Equation 4.3. For the sake of simplicity, the calculation assumes that the channel inductance does not vary during the discharge. Its value is adjusted to fit the current measurements. The resistance of the voltage divider is 10 Ω. In the calculations the inductance of the voltage divider was neglected. The inductance and the resistance of the generator and its cables were measured[Pen02c], and are taken as 437 nH and 52 mΩ, respectively.

Figure 4.4 shows the results of this calculation. Plotted are the measured curves and the calculated ones for two sets of parameters. The first set, corresponding to the dashed lines in the plot, assumes a final channel conductivity of 10^4/Ωm and a channel inductance of 1100 nH. The comparison with the measurements shows that the calculated discharge current is too high in this case. The calculated current through the voltage divider is too high, which is caused by the neglect of its inductance, which reduces the current. The calculated curves for a second set of parameters, namely a final conductivity of $5 \cdot 10^3$/Ωm and a channel inductance of 700 nH, are plotted in dash-dotted lines. The curve of the total current is in very good agreement with the measurement. It diverges after approximately 15 µs when the quadratic fit for the channel radius no longer holds. The current through the voltage divider is again too high. All in all, the simulations are consistent with a channel conductivity of roughly $5 \cdot 10^3/\Omega\text{m}$ in this setup. All qualitative features are obtained, especially the phase shift between the main current and the current through the voltage divider.

4.1. Ion beam transport and channel evolution

Three sets of data are combined to analyze the beam transport in the channel: the discharge current, the evolution of the channel diameter, and the size of the ion beam. By combining these data, the measurements can be compared with the predictions of the calculations. Starting with the explanation of the measurement techniques and data analysis, we will then proceed to interpret the results. The measurements of the channel diameter and beam size both require digital high-speed cameras. As these cameras can only take one picture per discharge, the discharge is repeated under identical discharge conditions with varied camera timings, so that the combination of the results yields a time series. Tests verified the reproducibility of the discharge, provided that no instabilities develop. By comparing the monitor signal with the measured current profile, the exact timing of each exposure is determined.

The measurement of the channel diameter is straightforward. The starting point is a side-on image of the central section of the channel with up to 4096 intensity steps (see Figure 4.9c). Taking vertical slices of the images yields intensity profiles $I(y)$ which are fitted with a Gaussian curve

$$I(y) = I_0 \cdot \exp\left[-(y-y_0)^2/2\sigma_r^2\right] \tag{4.9}$$

The full-width-half-maximum (FWHM) W of the channel is related to the fit width by

$$W = 2\,\sigma_r \cdot \sqrt{2\ln(2)} \tag{4.10}$$

Naturally, the width of the channel is not absolutely constant along the axis. Additionally, the intensity profiles are not perfect Gaussian curves. To minimize the fitting error, the width is calculated for each vertical line of the picture and the average over all fits is calculated. In a second step, the average intensity profile of the channel is calculated and again fitted with a Gaussian function. Taking the average of both methods yields the channel width. In addition, this averaging yields an estimate of the fitting error caused by spatial variations of the channel. All these calculations are performed automatically in a small IDL[Res99] program.

The results are plotted in Figure 4.9, 4.10, and 4.11. Fitting these curves with a quadratic function

$$W(t) = a_0 \cdot (\text{cm}) + a_1 \cdot \left(\frac{\text{cm}}{\mu\text{s}}\right) \cdot t + a_2 \cdot \left(\frac{\text{cm}}{(\mu\text{s})^2}\right) \cdot t^2 \tag{4.11}$$

yields an analytic formula for the evolution of the channel diameter. The curves are plotted in the figures and the fitting parameters are listed in Table 4.1. The average velocity $\bar{v}$ of the channel for the first 10 µs is given by

$$\bar{v} = \bar{\dot{R}} = 0.5 \cdot \bar{\dot{W}} = \frac{1}{2}\frac{W(10\,\mu\text{s}) - W(0)}{10\,\mu\text{s}} \tag{4.12}$$

Gas	p (mbar)	U_{main} (kV)	I_{max} (kA)	a_0	a_1	a_2	$\bar{v}$ (m/s)
NH_3	2.6 - 2.7	20	33.6	0.775	$7.26 \cdot 10^{-3}$	$1.87 \cdot 10^{-2}$	1000
	5.0	25	56.0	0.742	$-9.56 \cdot 10^{-3}$	$2.93 \cdot 10^{-2}$	1350
Krypton	0.5-0.8	25	51.2	0.374	$1.67 \cdot 10^{-1}$	$-3.42 \cdot 10^{-3}$	650
	1.8	25	42.0	0.481	$1.89 \cdot 10^{-1}$	$-1.05 \cdot 10^{-2}$	400
Xenon	0.9-1.1	25	52.8	0.496	$9.55 \cdot 10^{-2}$	–	450

Table 4.1.: Fit parameters for the channel evolution. The evolution of the channel diameter is fitted with a quadratic curve with parameters a_0, a_1, and a_2. U_{main} is the capacitor voltage, I_{max} is the maximum current, and $\bar{v}$ is the average expansion velocity of the channel.

and varies between 400 m/s in krypton and up to 1350 m/s in ammonia. Since the channels expand rapidly, it is obvious that the pressure inside the channel must be much larger than in the case of an equilibrium. For a homogeneous current density inside the channel, the equilibrium pressure profile is given by Equation 2.21. The pressure gradient in this case is given by

$$\frac{dp}{dr} = -p_0 \cdot \frac{2r}{R^2} \tag{4.13}$$

where p_0 is the pressure on the axis and R is the radius of the channel. The lower limit for the pressure on the axis is therefore given by

$$p_0 = \frac{\mu_0 I^2}{4\pi^2 R^2} \propto \frac{I^2}{R^2} \tag{4.14}$$

The radii of the channels at current maximum vary between 0.5 cm and 0.8 cm, so that the minimum pressure varies between 1 bar and 0.5 bar for a 10 kA discharge and between 20 bar and 8 bar for a 40 kA discharge. The high expansion velocity indicates that the real pressure is much bigger.

This section focuses on beam dynamics measurements, that is measuring how the beam size evolves over time. The method of these measurements is simple: a mask shapes the beam prior to entering the channel and a scintillator detects its shape after passing the channel. A sketch of the diagnostic setup is shown in Figure 4.6. The ion beam comes from the left and hits a pepperpot mask, which blocks most of the beam ions and thereby creates an exactly defined spatial beam profile. This makes it much easier to study the beam dynamics, since distortions and inversions of the beam can be easily spotted on the scintillator image. The pepperpot mask is mounted in the differential pumping section and has an angle of 45° to the beam axis. It is made of molybdenum, has small hole borings with diameters between 1 mm and 2 mm and separates two distinct regions: to its right the gas density is equal to the (ambient) density inside the chamber, whereas to its left the pumping section reduces the density to fore-vacuum conditions, that is to a pressure of roughly 10^{-2} mbar. The purpose of the pepperpot is thus threefold: to shape the spatial profile of the ion beam, to reduce the gas throughput to the differential pumping section, and to serve as a mirror for the carbon-dioxide laser that reflects it into the chamber. After passing the pepperpot, the remaining ions enter

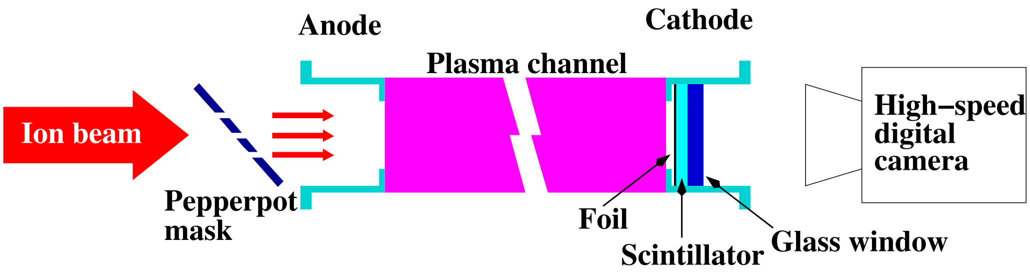

Figure 4.6.: Principle of beam transport measurements with a pepperpot mask, a scintillator, and a digital camera.

the chamber through the hollow anode, travel inside the channel, and finally hit the scintillator (BC-100) mounted inside the cathode at the other end of the chamber. A 10 µm thin nickel foil blocks light from the discharge, but causes only a negligible energy loss of the ions. Behind the scintillator is a glass window that protects it from the atmospheric pressure outside the chamber. A high-speed digital camera photographs the scintillator, which emits light when hit by the ions. Since the intensity of the light emitted by the scintillator is much weaker than that emitted from the discharge, the minimum exposure time is 0.5 µs, in contrast to 10 ns for images of the discharge.

The scintillator images yield qualitative information about the beam transport properties of the channel: a distortion of the beam shape indicates non-linearities of the magnetic field and the information whether the beam is inverted or not limits the range of possible betatron wavelengths. For a more profound analysis of the transport properties, quantitative data are necessary. The size of the beam is a suitable measure that can be derived from the images and can be compared with the theoretical calculations.

Measuring the beam size is straightforward. In order to analyze a large number of pictures efficiently, it is necessary to automate the analysis, so the whole analysis is carried out by a small IDL[Res99] program to which the user only specifies the name of the image to be analyzed. The boundary of the beamlets is determined by their contour lines (see Figure 4.9a). Since the betatron oscillation does not rotate the beam but at most inverts it, the size of the beam is proportional to the area of the rectangle that covers the whole beam. The size of this rectangle is given by

$$F_{\text{beam}} = (x_{\text{max}} - x_{\text{min}}) \cdot (y_{\text{max}} - y_{\text{min}}) \tag{4.15}$$

where x_{min} refers to the minimum x coordinate encountered in any of the contour lines, x_{max} to the maximum x coordinate, and correspondingly for y_{min} and y_{max}. To get a quantity that scales linearly with the proportions of the beam, the average ‘diameter’ of the beam is defined as

$$D_{\text{av}} = \sqrt{F_{\text{beam}}} \tag{4.16}$$

Figure 4.7 shows three typical scintillator images. The first picture is a reference picture of the beam passing a chamber without a discharge channel. As the ion beam did not overlap with the whole pepperpot mask, some of the mask ‘points’ that are shown in Figure 2.6a are missing, but this has no major effect on the analysis besides reducing the beam size. The

Without channel *Partly focused* *Full focus*

Figure 4.7.: Scintillator pictures for three stages of the transport. The pepperpot mask was not fully illuminated by the ion beam, so that only a part of the cross shape is visible.

second image shows a partly focused beam. While the shape of the cross and its orientation are still clearly visible, its size is drastically reduced. The last image shows a focused beam. In this case the beam ions are now focused in a very small area, so that the orientation of the cross is no longer discernible.

To be able to analyze the data, it is necessary to calculate the effects predicted by the theory. In the following, we always assume that the current density inside the channel is homogeneous, so that the particle trajectories are given by betatron oscillations. The size of the ion beam on the scintillator depends on the phase of the betatron oscillation after traversing the whole channel. The size $r(t,z)$ is given by

$$r(t,z) = r_0 \cdot \cos\left[\phi(t,z)\right] \tag{4.17}$$

where ϕ denotes the betatron phase at time t and at z and r_0 is the initial size of the beam. Obviously, the phase at the scintillator is given by $2\pi L/\lambda_B$, L being the channel length. The betatron wavelength was derived in Section 2.3.4 as

$$\lambda_B = \underbrace{\sqrt{\frac{(2\pi)^3 \cdot m_u \cdot c}{e \cdot \mu_0}}}_{\text{constant}} \cdot \underbrace{\sqrt{\frac{\beta \cdot N}{Z_{\text{eff}}}}}_{\text{beam parameters}} \cdot \underbrace{\frac{R(t)}{\sqrt{I(t)}}}_{\text{channel parameters}} \tag{4.18}$$

where m_u is the nucleon mass, N the mass number, R the channel radius, and I the discharge current. The first two factors are constant, whereas the last depends only on the channel dynamics. All measurements used a $^{209}_{83}\text{Bi}$ beam with a kinetic energy of 11.4 MeV. Inserting the beam data, the expression for the betatron wavelength simplifies to

$$\lambda_B = 1.796 \cdot 10^4 \sqrt{\text{A}} \cdot \frac{R(t)}{\sqrt{I(t)}} \tag{4.19}$$

As the wavelength grows linearly with the channel radius and is inversely proportional to the square-root of the discharge current, the variations of the channel have a major influence on the focusing properties of the channel. Focal points are essential for the analysis of the beam

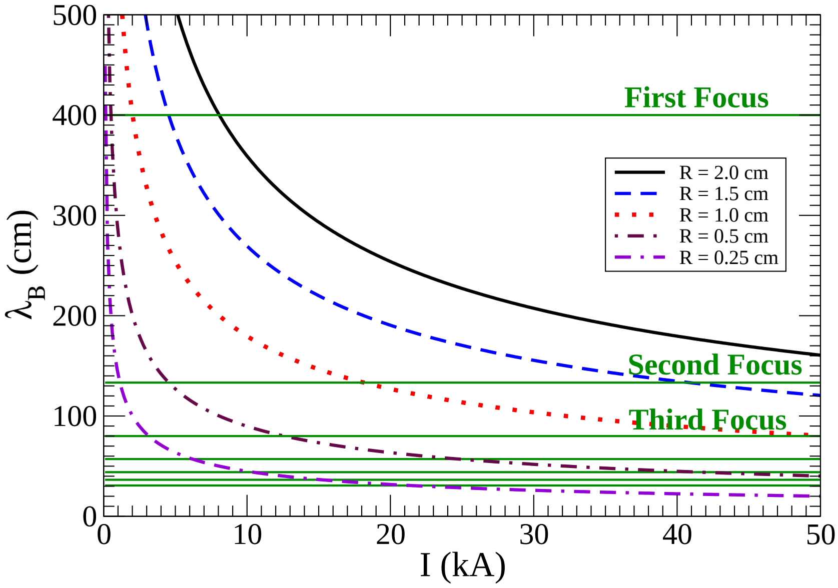

Figure 4.8.: The betatron wavelength λ_B calculated for five different channel radii, depending on the discharge current in the channel. In addition, the wavelengths corresponding to the first focal points are marked. The curves are calculated for a $^{209}_{83}$Bi beam with a kinetic energy of 11.4 MeV.

transport, since the beam reaches its minimum size and is inverted when passing these points. The focal points are given by the condition

$$L = (2n+1)\,\lambda_B/4 \qquad n \in \mathcal{N}_0 \tag{4.20}$$

or, conversely,

$$\lambda_B = 4L/(2n+1) = (4L, 4L/3, 4L/5, 4L/7, \ldots) = (400\,\mathrm{cm}, 133.3\,\mathrm{cm}, 80\,\mathrm{cm}, \ldots) \tag{4.21}$$

Figure 4.8 shows plots of the betatron wavelength, the focal points being indicated by horizontal lines. The beam is inverted between the first and the second focal point, twice inverted (and thus upright again) between the second and the third focal point, thrice inverted between the third and the fourth focal points, and so on. As can be seen in the figure, the beam dynamics is very sensitive to the channel radius, a smaller radius leading to more beam inversions.

The transport properties were measured for five different sets of channel parameters: one channel in xenon, two channels in krypton, and two channels in ammonia. The data are plotted in the Figures 4.9, 4.10, and 4.11. The plots show the discharge current, the evolution of the channel diameter, and the evolution of the beam diameter. In addition, inversions of the beam are indicated in the plots. It was not possible to detect inversions in all measurements, as in the case of the measurements with xenon and 1.8 mbar krypton, the beam was most of the time too small to detect its orientation. All beam transport measurements used a bismuth beam with a kinetic energy of 11.4 MeV/u.

Naturally, all measurements start with the initial beam size $D_{\mathrm{av}}(t=0)$ which is approximately 1.2 cm. At the beginning the discharge current is equal to zero and the betatron wavelength therefore infinite. It is also clear that the inversion of the current flow direction results in

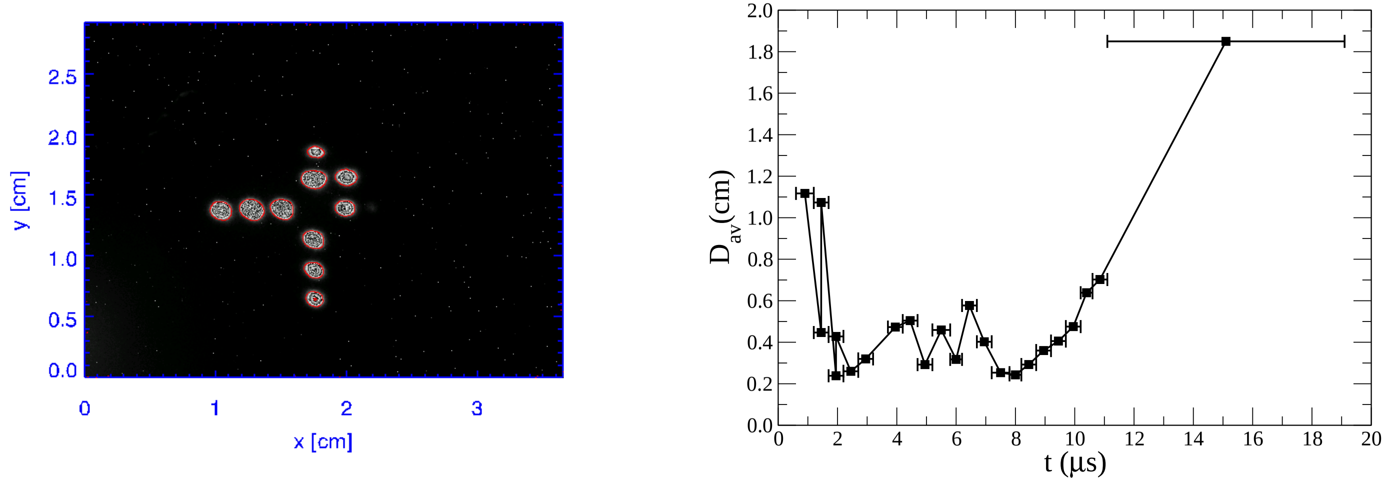

(a) A scintillator image with contour lines

(b) Xenon, 1 mbar, 25 kV / 25 kV

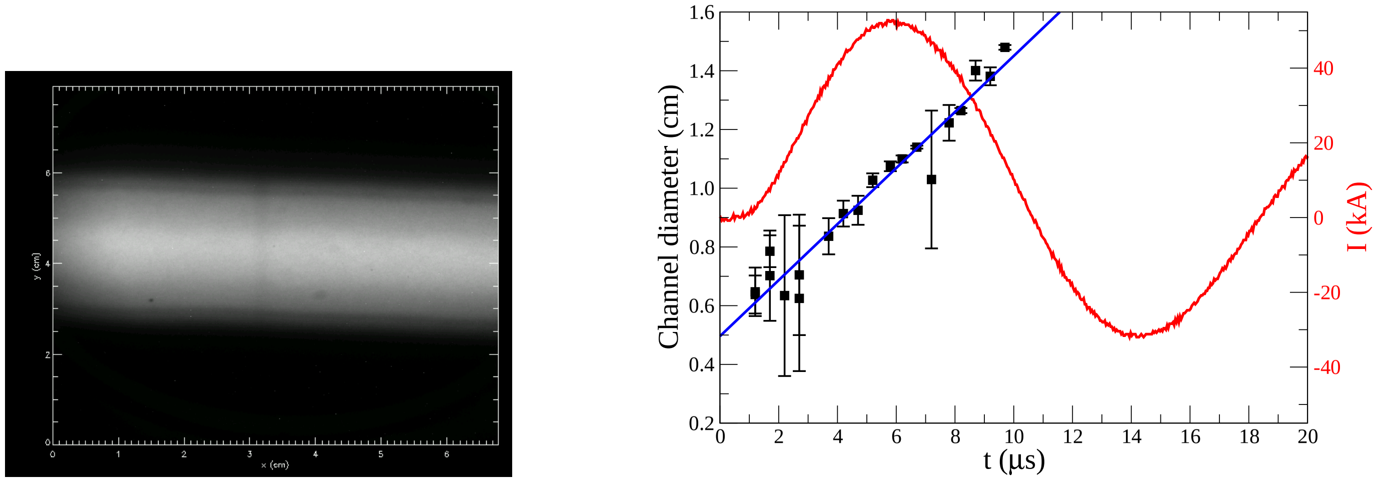

(c) An image of the discharge channel

(d) Channel diameter (FWHM) and discharge current

Figure 4.9.: Image of the scintillator with contours and of the discharge channel. Measured size of the beam and channel for a ^{209}Bi beam with 11.4 MeV/u in Xenon. The beam is too much focused in xenon to detect a beam inversion.

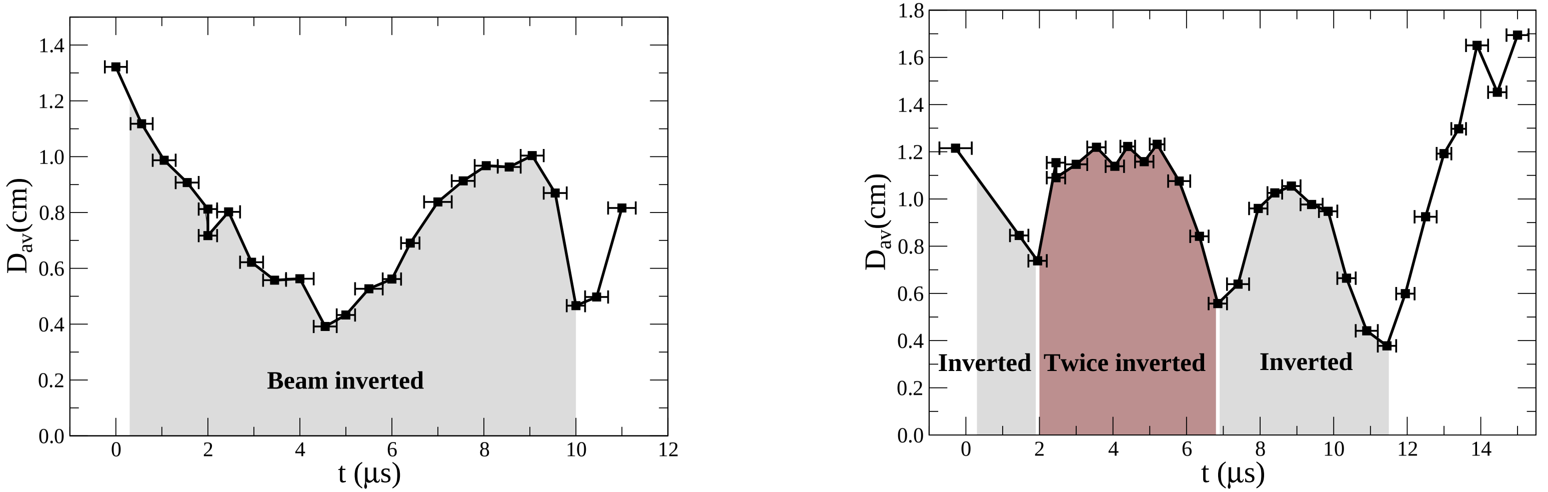

(a) Ammonia, 2.6 mbar, 25 kV / 20 kV

(b) Ammonia, 5 mbar, 25 kV / 25 kV

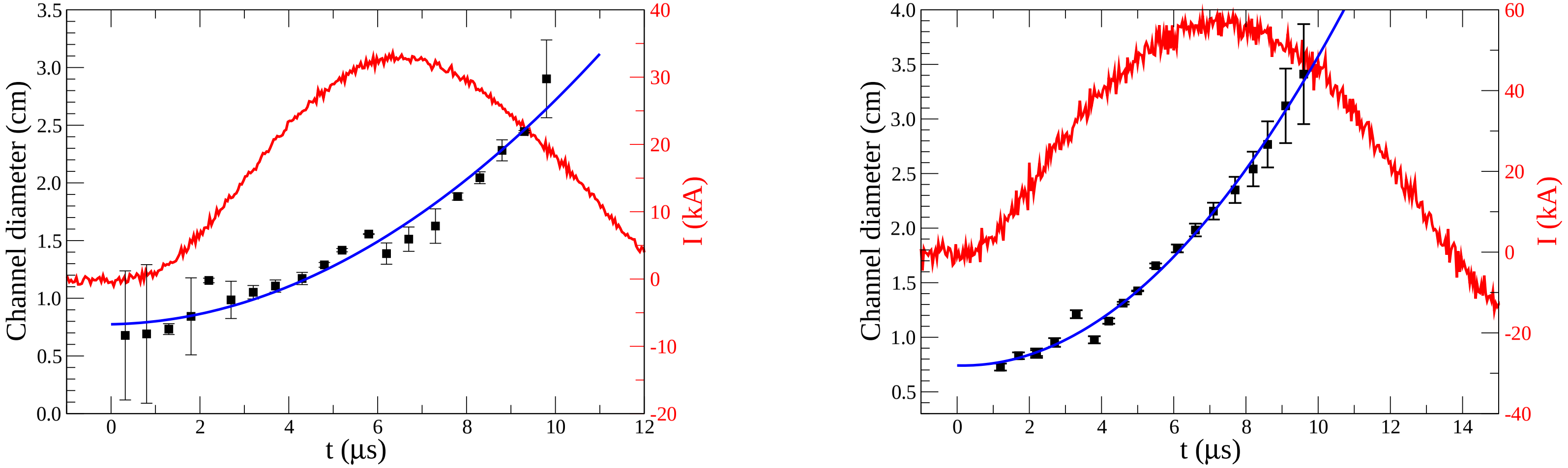

(c) Channel diameter (FWHM) and discharge current

(d) Channel diameter (FWHM) and discharge current

Figure 4.10.: Measurements of beam focusing and channel widths for ammonia at two pressures using a ^{209}Bi beam with 11.4 MeV/u.

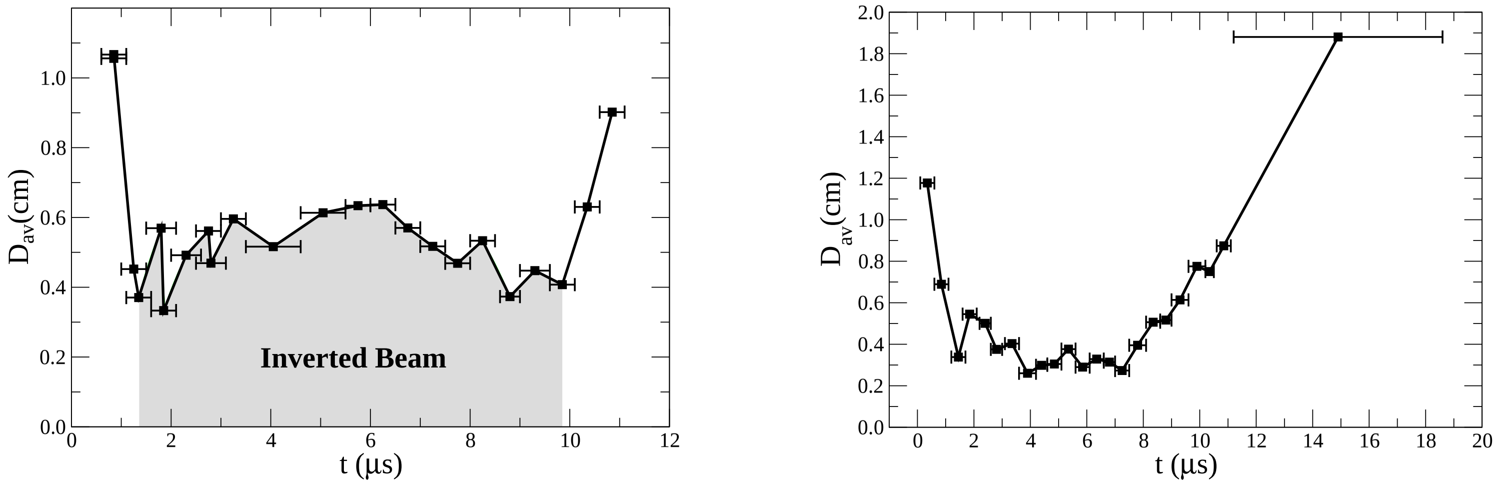

(a) Krypton, 0.6 mbar, 25 kV / 25 kV

(b) Krypton, 1.8 mbar, 25 kV / 25 kV

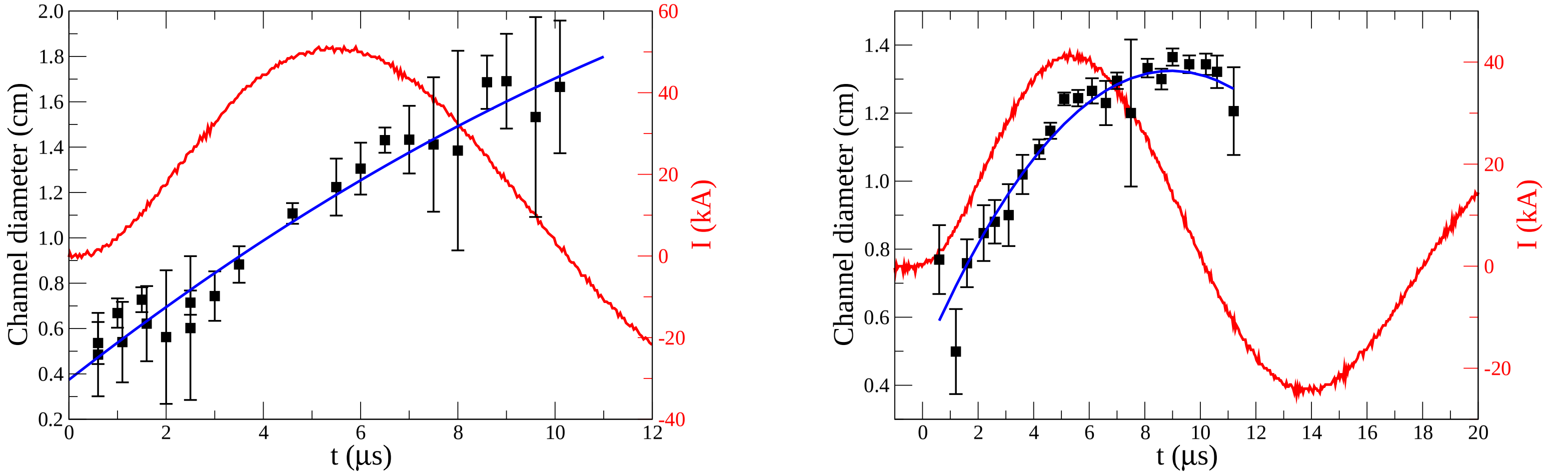

(c) Channel diameter (FWHM) and discharge current

(d) Channel diameter (FWHM) and discharge current

Figure 4.11.: Channel width measurements for krypton at two pressures, using a ^{209}Bi beam with an energy of 11.4 MeV/u. The beam is too much focused at 1.8 mbar to judge if it is inverted.

a diverging beam and thus a largely growing beam size. All measurements show that after the first half period of the discharge, which takes roughly 10-12 µs, the beam size indeed increases rapidly, getting bigger than it would be without a channel. The dynamics between these two limits is complicated and depends, as indicated above, sensitively on both the channel radius and the discharge current. In the initial stage the channel is 0.5 cm to 0.7 cm in diameter and thus actually smaller than the beam diameter, so that we have the situation of a mismatched beam, described in Section 2.3.5. The dynamics during the first half period can be divided in two sections. In the time before the current maximum (roughly at 6 µs), both the channel diameter and the discharge current increase. Since an increasing diameter increases the betatron wavelength, whereas an increasing current decreases it, these effects partly compensate each other, resulting, at least initially, in an overall decrease of the betatron wavelength. After the current maximum, the discharge current decreases, so that the betatron wavelength increases from that point on. The expansion rate of the channel varies between the different measurements and is the fastest for ammonia, resulting in large variations of the betatron wavelength. In the following, a short overview of the measurements is given:

- 1 mbar xenon: The discharge uses a capacitor voltage of 25 kV. The maximum discharge current is 52.8 kA and is reached after 6 µs. In that time, the channel expands from 0.6 cm to 1.1 cm. The beam diameter drops rapidly drops rapidly during the first 2 µs and stays very small for the subsequent 6 µs. The beam is so small that it is impossible to detect beam inversions.

- 0.6 mbar krypton: The discharge uses a capacitor voltage of 25 kV. The maximum discharge current is 51.2 kA and is reached after roughly 5.5 µs. In that time, the channel expands from an initial diameter of 0.5 cm to 1.2 cm. The beam diameter drops during the first 2 µs to roughly 0.5 cm and varies little in the subsequent 8 µs. The beam is inverted, but due to the rapid decline of the beam diameter in the beginning, it is not clear if it is once or thrice inverted.

- 1.8 mbar krypton: The discharge uses a capacitor voltage of 25 kA. The maximum discharge current is 42 kA and is reached after 5.5 µs. In that time, the channel expands from 0.6 cm to 1.2 cm. The beam size drops to 0.4 cm during the first 2 µs and stays roughly at this level for the next 6 µs. The beam is so small that it is not possible to detect beam inversions.

- 2.6 mbar ammonia: The discharge uses a capacitor voltage of 20 kV. The maximum discharge current is 33.6 kA and is reached after 6 µs. During this time, the channel diameter increases from 0.7 cm to 1.5 cm. The beam size drops nearly linearly during the first 5 µs and then expands again before it is again reducing after 9 µs. The beam is inverted early on; it is not clear if the beam is once or thrice inverted.

- 5 mbar ammonia: The discharge uses a capacitor voltage of 25 kV. The maximum discharge current is 56 kA and is reached after 7.5 µs. During this time, the channel expands from an initial diameter of 0.7 cm to 2.5 cm. The beam size ‘oscillates’ between its initial size and minimum sizes of 0.4-0.6 cm. The beam is inverted in the beginning, then

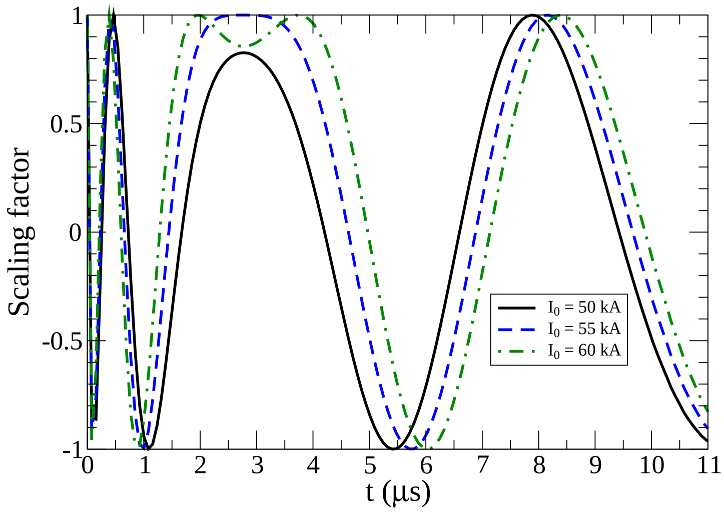

Figure 4.12.: Calculated scaling for a discharge in ammonia. The channel evolves according to the measurement in 5 mbar ammonia.

twice inverted (and thus being upright again), and the inverted until the final expansion after 11.5 µs.

To compare the measurements with the theory, the focusing beam according to the simple betatron model was calculated for the parameters of the discharge in 5 mbar ammonia. The calculation modelled the channel expansion with a quadratic curve fitted to the measurement data and assumed a sinusoidal discharge current. The results for three different discharge currents are plotted in Figure 4.12. The curves show a fast oscillation of the beam size during the first 0.5 µs. As the exposure time for the images is at least 0.5 µs, this is not detectable in our measurement. For the next 1 µs, the beam is inverted, followed by roughly 4 µs, during which it is upright again and has roughly its original size and is then inverted again. If we compare this to the measurements, we see that the qualitative behavior is similar, but that the calculated curve oscillates faster than in the measurements. This might be due to uncertainties in the channel radius or measurement errors for the discharge current. All in all, the calculations produce results similar to the measurements, but a fitting of the measurements with calculated curves is not possible due the extreme sensitivity of the scaling with regard to changes in the channel diameter or the discharge current.

4.2. Channel instabilities

It is essential to limit the growth of channel instabilities, since their uncontrolled growth might worsen the beam transport properties of the channel and even lead to its disruption. Therefore it is necessary to keep the instabilities small until the beam has passed the channel. In the following, the study is limited to pure magnetohydrodynamical instabilities. Ion-beam induced instabilities of the beam-plasma system are important only for large beam currents and can therefore not be studied with our experimental setup. The results of the theoretical analysis of these instabilities are outlined in Section 2.3.9.

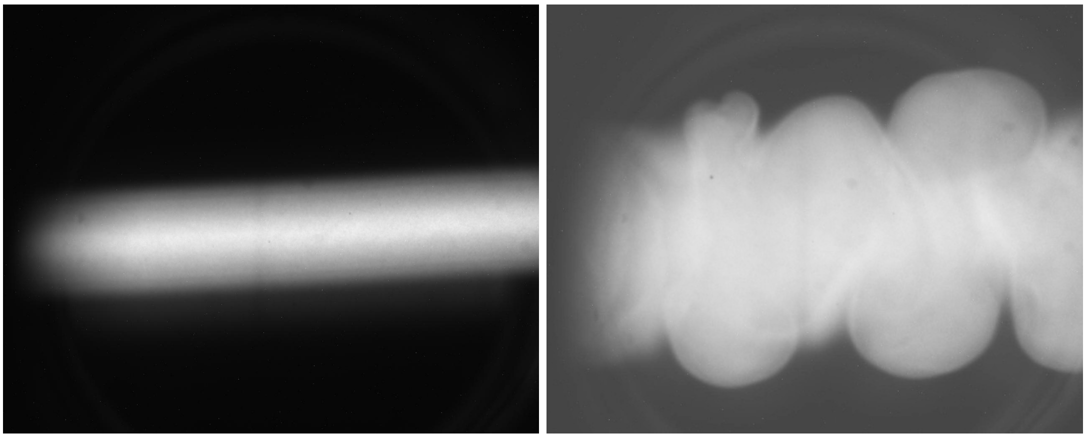

(a) Stable discharge (b) Unstable discharge

Figure 4.13.: A stable channel and a fully developed kink instability in ammonia. Both photographs show a 6.8 cm central section of the channel.

The difference between a stable and an unstable channel is illustrated in Figure 4.13. Here the unstable channel shows the typical helix-like structure of a kink instability. The development of instabilities was studied for channels in ammonia, xenon, and krypton. For normal operating conditions, that is for pressures up to 10 mbar in ammonia and around 2 mbar in krypton and xenon, no pronounced instabilities were observed. A thorough search for instabilities in ammonia revealed that they develop for pressures above 15 mbar. As indicated in Figure 4.2, it is not possible to use the prepulse, since it does not create a discharge channel at these high pressures. Due to its larger stored energy, the main discharge is still able to create a discharge channel, but usually only with a delay of several microseconds (see Figure 4.14).

The lack of a prepulse is one of the factors that make the channel more susceptible for instabilities. Another factor is the high gas density itself. As indicated in Figure 3.7, the laser pulse is fully absorbed at a pressure of roughly 20 mbar. For such high pressures, the laser absorption along the axis is very inhomogeneous and the resulting variations in the density and temperature profiles along the axis can drive the development of instabilities. In addition, the channel rarefaction at these high pressures is less efficient than for lower pressures, so the stabilizing effect of the density profile is smaller.

In order to compare the experiment with the theory, which is described in Section 2.2.4, it is necessary to measure both the wavelength and the growth rate of the instability. This requires a time series of channel images that can be analyzed. For stable channels such time series can be measured simply by repeating the discharge with constant parameters and adjusting the time of the snapshot for each iteration, but this method cannot be used for unstable channels. As, by their very nature, instabilities are not reproducible, it is necessary to take all images of the time series during one discharge. The framing camera used in our experiment makes this possible, as it is able to take eight subsequent images in a row, each picture having a minimum exposure time of 10 ns. The relative timing of these images can be adjusted freely, provided that the exposures do not overlap. Figure 4.15 shows such a series of images, taken during a discharge in 22 mbar of ammonia. The series starts at the time of the current maximum

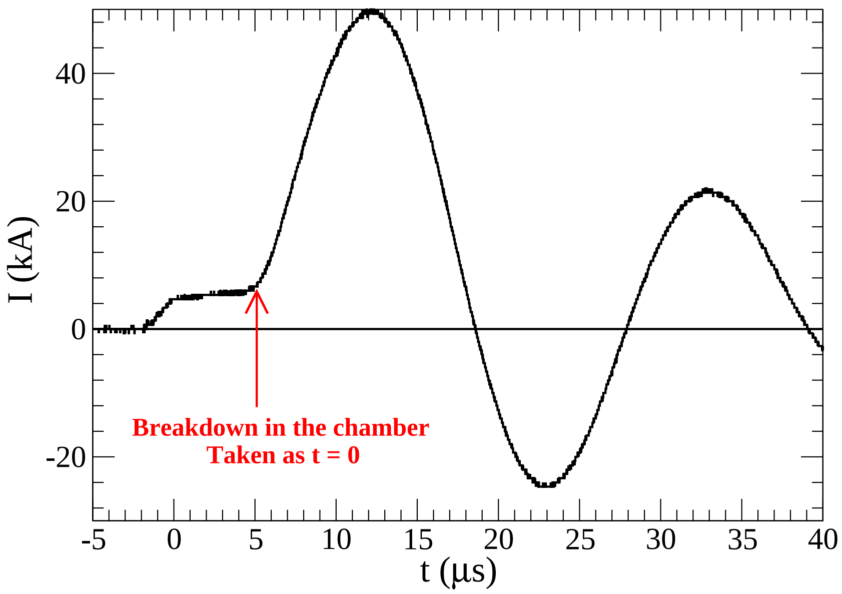

Figure 4.14.: The discharge current in 22 mbar ammonia. The curve indicates that the breakdown in the chamber occurs with a delay of 6 µs. Before that breakthrough, the current is limited by the resistance of the voltage divider.

.

when, as can be seen in the first picture, the development of an instability has already set in. The subsequent pictures, which were taken in 1 µs steps, show that the spatial structure of the instability stays constant and that its amplitude increases.

As mentioned above, the characteristic properties of a kink instability are its wavelength λ and its amplitude. The images show that the instability of the channel can only approximately be described by the helical structure of a kink instability, so the aim of the measurements is to determine its *averaged* wavelength and its *averaged* amplitude.

To this end, the images of the framing camera are analyzed with a small program written in the *Interactive Data Language* (IDL)[Res99]. The analysis is semi-automatic and illustrated in Figure 4.16. After the picture is selected, the program starts by determining the border of the channel (indicated in red) with a contour fit. The program then calculates the averaged boundaries of the channel from the contour data, yielding in turn the center of the channel and an averaged channel radius. The averaged boundaries and the central axis of the channel are indicated with dashed lines in the figure. So far, no user interaction was required, but now the maxima and the minima of the kink must be specified by the user. The selected points are indicated by small squares in the figure. Based on these data, the program calculates the averaged wavelength and the averaged amplitude of the instability. The interactive selection of the maxima and minima is the largest source for errors in the analysis, since it is based on subjective decisions. Yet the averaging process limits the effect of these errors on the calculations.

The analysis of the instabilities requires amplitudes of at least 0.1 cm, as otherwise the extrema cannot be marked accurately. The method is therefore not applicable to the early stages of the instability, when the instability is already discernible, but its amplitude is still small. For

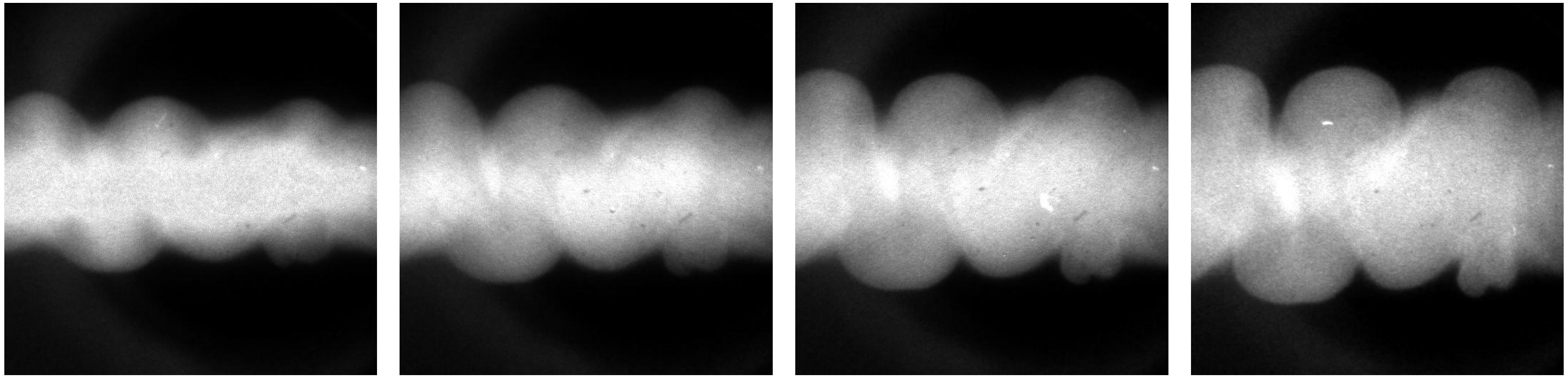

(a) $t = 8\,\mu s$ (current maximum) (b) $t = 9\,\mu s$ (c) $t = 10\,\mu s$ (d) $t = 11\,\mu s$

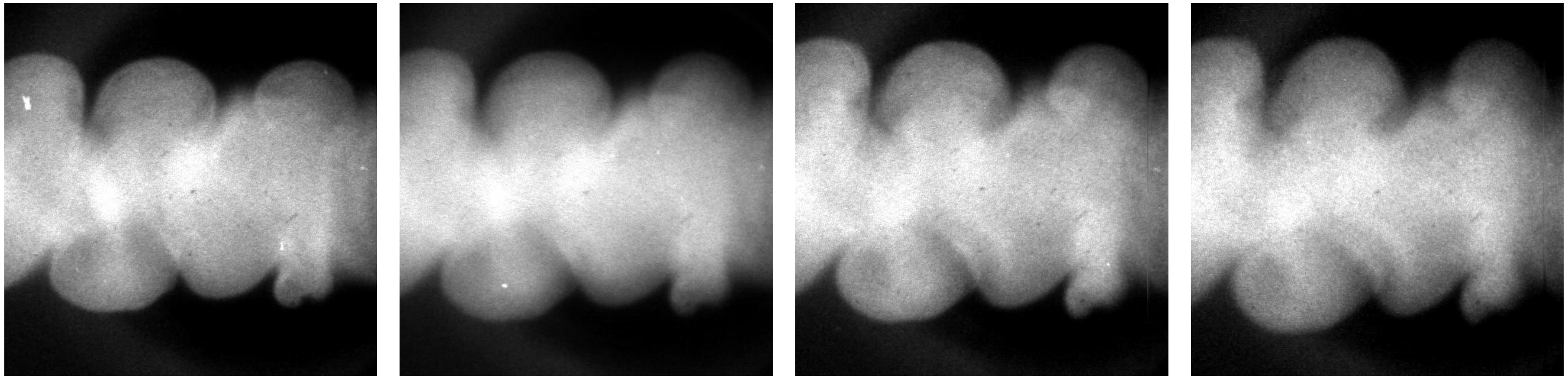

(e) $t = 12\,\mu s$ (f) $t = 13\,\mu s$ (g) $t = 14\,\mu s$ (h) $t = 15\,\mu s$

Figure 4.15.: Framing images which show the development of an instability in an discharge in 22 mbar of ammonia. The discharge was created without a prepulse and a main capacitor voltage of 25 kV. For better visibility, the brightness and the contrast of the pictures were adjusted for each picture. The pictures show a 6.5 cm long section of the channel.

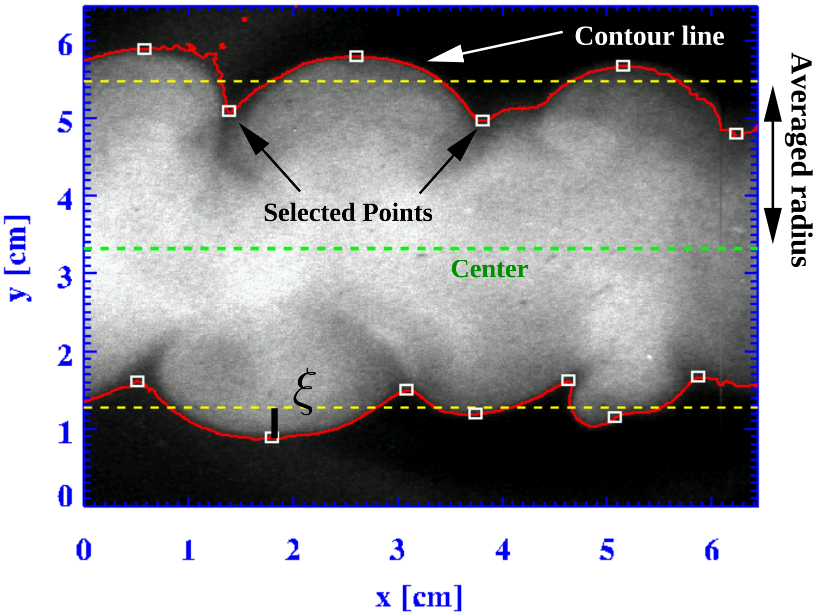

Figure 4.16.: The measurement of the channel perturbation. The surface of the channel, indicated in red, is detected automatically. Likewise, the axis of the channel and the average diameter are calculated automatically. The extrema, indicated by small squares, are selected by the user.

pressures between 15 mbar and 20 mbar instabilities are visible but cannot be analyzed because of this limitation. In the following, four measurements with identical discharge parameters are compared. All measurements used 22 mbar ammonia and a capacitor voltage of 25 kV. The results of the measurements are shown in Figure 4.17, which shows the development of the amplitude of the instability and of the channel radius. The expansion velocity of the channel was determined by linear regression of the data. Likewise, an average growth rate $\dot{\xi}$ of the instability was determined. In addition, the amplitude data was fitted with the function

$$\xi(t) = \xi_0 \cdot \exp(\Gamma \cdot t) \tag{4.22}$$

that describes the exponential growth of the instability. The fit parameters are listed in Table 4.2. The measurements show that the expansion of the channel is five to ten times faster than the growth of the instability.

In the following, the experimental results are compared with the theoretical model outlined in Section 2.2.4. Obviously the model and the channel in our experiment differ in several important aspects. Most importantly, the model starts with a stationary channel and assumes that the whole current flows on the surface of the pinch, whereas in the experiment the channel is rapidly expanding and the current density is homogeneous inside the channel.

The measurements show that the wavelength of the instability varies only little between the individual measurements and is on average 1.9 cm. According to the theory, the wavelength

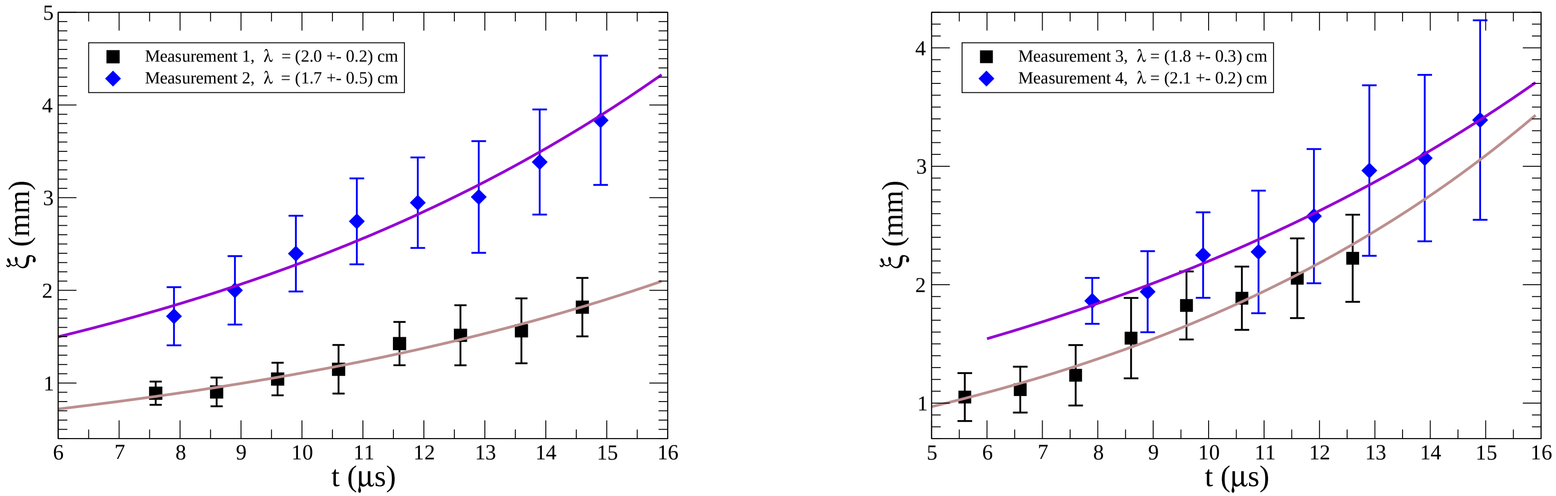

(a) Instability amplitude ξ for the first two measurements

(b) Instability amplitude ξ for the last two measurements

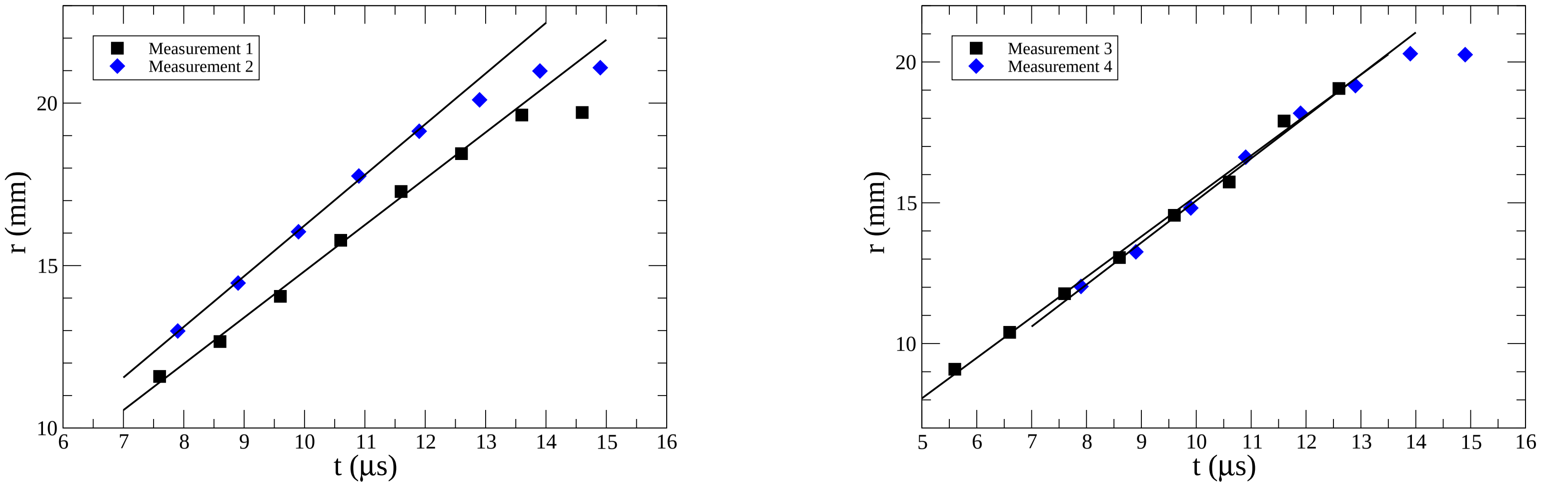

(c) Averaged channel radius r for the first two measurements

(d) Averaged channel radius r for the last two measurements

Figure 4.17.: Measurement of instability growth in 22 mbar of ammonia. The discharges used no prepulse and the main pulse generator had a voltage of 25 kV. The top row shows the averaged instability amplitude and the bottom row shows the development of the averaged channel radius. Also given is the averaged wavelength λ of the perturbation. The current maximum was at $t = 7.6\,\mu\text{s}$.

Measurement	λ (cm)	$\Delta\lambda$ (cm)	v_r (m/s)	$\dot{\xi}$ (m/s)	$v_r/\dot{\xi}$	ξ_0 (mm)	Γ (1/s)
1st	2.0	0.2	1425	137	10.4	0.38	$1.08 \cdot 10^5$
2nd	1.7	0.5	1560	283	5.5	0.79	$1.07 \cdot 10^5$
3rd	1.8	0.3	1437	180	8.0	0.54	$1.16 \cdot 10^5$
4th	2.1	0.2	1492	224	6.7	0.91	$8.85 \cdot 10^4$

Table 4.2.: Parameters of the fits of the instability measurements. The wavelength of the instability is given by λ. The channel expansion velocity v_r and the averaged growth rate of the amplitude of the instability $\dot{\xi}$ are determined by linear regression. In addition, the data for the instability are also fitted with the exponential function $\xi(t) = \xi_0 \cdot \exp(\Gamma \cdot t)$.

corresponding to the maximum growth rate for a pinch surrounded by gas is given by

$$\lambda_{\max} \approx 9.2 \cdot r_p \tag{4.23}$$

where r_p is the radius of the pinch. The measured wavelength of 1.9 cm therefore corresponds to a channel diameter of 4.2 mm. Since the initial diameter of the discharge channels is typically between 4 mm and 8 mm, the measurement is consistent with the theory.

For small amplitudes, the growth rate of the instability is exponential. If the amplitude ξ exceeds a critical value, which is given by[Man73]

$$\xi > \frac{\lambda}{2\pi} \tag{4.24}$$

the growth rate is reduced and the amplitude ξ becomes proportional to $(t - t_0)^2$, where t_0 is the time of this transition. For a wavelength of 1.9 cm, the transition is reached for an amplitude of 3 mm. A comparison with the measured amplitudes (see Figure 4.17) shows that our measurements should correspond to exponential growth, the growth rate being on average roughly 10^5/s.

As expected, the analytical model is not able to quantitatively reproduce the measurements, since a growing instability with a wavelength of 2 cm would require a channel diameter of less than 7 mm, which is smaller than the measured diameters. Yet the qualitative statement of the theory, indicating a stabilization of the discharge by the surrounding gas blanket is verified by the measurements, since the channel is stable for normal operating parameters. This is in contrast to what would be expected for a pinch in vacuum which is very susceptible for kink instabilities.

5. Summary

Assisted pinched transport is studied as a promising alternative to neutralized-ballistic transport, since it can be used with all three kinds of chamber protection, namely thick-liquid wall, wetted-wall, and dry-wall schemes. It uses a plasma lens to focus the ion beam outside the chamber and a plasma channel to transport the beam towards the hybrid target at the center of the chamber. The channel plasma provides free electrons for the neutralization of the space charge and the current of the ion beam. In addition, a moderate discharge current of roughly 50 kA creates a large azimuthal magnetic field that prevents the ions from leaving the chamber. The appeal of the scheme is the decoupling of the focusing of the beam and the final transport, which relaxes the focusing requirements. Simulations and theoretical estimates indicate the system is able to transport high-current heavy-ion beams.

The purpose of this work is to demonstrate the feasibility of creating 1 m long, stable and free-standing discharges and to study their transport properties for low-current heavy-ion beams and the stability of the channel. To create such long channels, it was necessary to extend the chamber to twice its original length by inserting a new, 50 cm long, section. As this changed the proportions of the chamber significantly, the minimum electric field on axis dropped dramatically. In order to prevent breakdowns to the chamber walls, the electric field in the chamber was altered by electrically insulating the three chamber segments from each other with two nylon flanges and by setting them to three different potentials. The electrostatic code POISSON was used to calculate the electric field inside the chamber for different potential setups. The calculations showed a fifteen-fold increase of the minimum electric field on axis if three wall potentials were used instead of using only one potential for the whole chamber wall. With the help of this optimization, it is possible to create stable channels in various gases. The channels reach maximum discharge currents of more than 50 kA. The initial diameter of the channels varies between 0.5 cm and 1 cm. The channels expand, reaching diameters between 1 cm and 2 cm at the time of the current maximum , depending on the gas, the gas density, and the discharge voltage.

Two different channel initiation methods were used successfully: laser initiation with ammonia and ion beam initiation with various noble gases, most importantly xenon and krypton. Laser initiation with a carbon-dioxide laser requires an absorption band at roughly 10 µm in the gas for a sufficient laser absorption, thus limiting its use to ammonia in our experiment. This limitation does not apply to initiation with a short-pulse laser, as is proposed in the assisted pinched transport scenario. The channel formation was studied with CYCLOPS, a one-dimensional magnetohydrodynamical code. A simulation of the full channel creation process, that is laser-initiation, prepulse, and main discharge, was performed. The results agree qualitatively with the observations, but due neglected affects in the modelling the calculated plasma temperatures and related quantities, such as the conductivity, are too high.

The transport properties of the channel were studied in detail. A ^{209}Bi beam with a kinetic energy of 11.4 MeV was used in the experiments. The transport was studied quantitatively by measuring the beam size at the end of the chamber. This measurement was repeated at various stages of the discharge, thus yielding a time series. In addition, the channel diameter was measured at each stage. In combination with the measurement of the discharge current, this makes it possible to compare the measurements with that is expected if one assumes that the particle motion is described by betatron motions. The final size of the beam is very sensitive to both the discharge current and the channel radius, so it is not actually possible to fit the measurements with theoretical curves, due to the uncertainties of the measurements. Five time series were thus determined: one for xenon, and two for ammonia and krypton, respectively. Qualitatively, the measurements are consistent with the assumption of betatron oscillations, indicating a (nearly) homogeneous current density in the channel. Another indicator for a homogeneous current density is the fact that the ion beam is not distorted, since distortions would indicate non-linearities caused by variations in the current density.

Another focal point of this study is the examination of channel instabilities. Fortunately, no instabilities were observed for normal operating conditions. After an intensive search for instabilities in ammonia, it turned out that instabilities do develop, but only at pressures above 15 mbar. The instabilities show the characteristics of kink instabilities, since they have a helix-like structure. The evolution of the instability was studied quantitatively by analyzing a series of images taken with a framing camera. The analysis yielded the amplitude of the instability and the averaged channel radius at eight subsequent times during the discharge. The measurements were compared with a simple analytical model for kink instabilities. As predicted by the model, the wavelength of the instability is constant (within the margins of error) for identical discharge conditions and the growth of the instability is exponential as predicted. Yet the growth rates and the wavelength determined in the measurements differ from the predictions of the model, but this is not surprising as the model makes several assumptions that do not hold in our experiment, for instance that the whole discharge current flows on the surface of the channel.

This study has demonstrated the feasibility of creating discharge channels with parameters close to those required in a reactor. So far, no major obstacles for applying the scheme for the transport of high-current beams have been discovered. The most important point now would be to study the transport properties for high-current beams, which are so far only studied with simulations. Unfortunately, such beams are not available. An alternative is to use high-current proton beams, but since their stopping range is much shorter than that of the ions, it is not clear if the results of such measurements are applicable to heavy-ion beams. All in all, the results of this work show that the assisted pinched transport mode is a promising alternative to neutralized ballistic focusing and should as such be considered when designing a test facility.

A. Rate coefficients for a Maxwellian velocity distribution

The collision rates for various collisions (electron-electron, electron-ion) are necessary for calculating various transport properties like thermal and electrical conductivity. These calculations in turn require the rate coefficients $<\sigma v>$, which are calculated by averaging over the velocity distribution $f(\mathbf{v})$. The simplest case, which we will use here, is to assume an isotropic Maxwell distribution

$$f(v) = n\left(\frac{m}{2\pi T}\right)^{3/2} \cdot \exp\left(-\frac{m\mathbf{v}^2}{2T}\right) \tag{A.1}$$

where n denotes the number density, m the particle mass, and T the temperature of the particles. The rate coefficient is defined by

$$<\sigma v>= \int \sigma(v) \cdot v \cdot f(v)\, d^3\mathbf{v} \tag{A.2}$$

In general, the cross-section σ depends on the speed of the particles. If we write the integral in spherical coordinates, we obtain

$$<\sigma v>= \left(\frac{m}{2\pi T}\right)^{3/2} \cdot \int_0^{2\pi} d\phi \int_0^{\pi} d\theta \cdot \sin\theta \int_0^{\infty} dv_r \left[\sigma(v) \cdot v \cdot \exp\left(-\frac{mv^2}{2T}\right)\right] \tag{A.3}$$

The cross-section for electron-ion collisions is given by[Gol98]

$$\sigma_{ei} = \frac{Z_{\text{eff}}^2 e^4 \ln\Lambda}{4\pi\varepsilon_0^2 m_e^2 v^4} \tag{A.4}$$

where $\ln\Lambda$ is the Coulomb logarithm and $Z_{\text{eff}} = \sum_i n_i Z_i / \sum_j n_j$. Inserting this in equation A.3 yields

$$<\sigma v>= \sqrt{\frac{2}{\pi^3 m_e T_e^3}}\, \frac{Z_{\text{eff}}^2 e^4 \ln\Lambda}{12\,\varepsilon_0^2} \tag{A.5}$$

This formula does not include the mass and the velocity of the ions, since our calculation tacitly used the approximation of ions of infinite mass.

B. An analytical model for the dynamics of a z-pinch

In the following, an analytical model for the z-pinch is derived (S. Yu, private communication). The model describes the evolution of a homogeneous z-pinch with azimuthal symmetry, so cylindrical coordinates are used for convenience. The symmetry conditions for the fluid velocity $\mathbf{v}$, the mass density ρ, the pressure P, the current density $\mathbf{j}$ and the magnetic field $\mathbf{B}$ are

$$\mathbf{v} = v(r,t)\cdot\mathbf{e}_r;\rho = \rho(r,t);P = P(r,t);\mathbf{j} = j(r,t)\cdot\mathbf{e}_z;\mathbf{B} = B(r,t)\cdot\mathbf{e}_\theta \tag{B.1}$$

The continuity equation in cylindrical coordinates is then

$$\frac{\partial\rho}{\partial t} + \frac{1}{r}\frac{\partial}{\partial r}(r\cdot\rho\cdot v) = 0 \tag{B.2}$$

If we multiply this equation with $2\pi r^3$ and integrate over r, we obtain

$$2\pi\int_0^\infty r^3\frac{\partial\rho}{\partial t}dr = -2\pi\int_0^\infty r^2\cdot\frac{\partial}{\partial r}(r\cdot\rho\cdot v)dr = 4\pi\int_0^\infty r^2\rho\, v\, dr \tag{B.3}$$

using partial integration in the last step. Since the channel has only radial dynamics, the mass line density N

$$N = \pi\cdot r_0^2\cdot\rho_0 \tag{B.4}$$

is constant and can be calculated from the initial conditions (r_0: initial radius, ρ_0: initial mass density in the channel). In the following it is assumed that the mass density and current density inside the channel are homogeneous during the whole discharge. The dynamics of the pinch is then fully described by the evolution of the channel radius. The mass averaged radius R is defined by

$$R^2 = \langle r^2\rangle = \frac{2\pi}{N}\int_0^\infty r^3\rho\, dr = \frac{1}{2}R_{\text{ch}}^2 \tag{B.5}$$

where R_{ch} is the channel radius. Using this relation, Equation B.3 can be written as

$$N\cdot\frac{d}{dt}R^2 = 4\pi\int_0^\infty r^2\cdot\rho\cdot v\, dr \tag{B.6}$$

The magnetic force equation

$$\rho\cdot\frac{d\mathbf{v}}{dt} = -\nabla P + \mathbf{j}\times\mathbf{B} \tag{B.7}$$

is approximately (neglecting $(\mathbf{v}\cdot\nabla)\mathbf{v}$)

$$\rho\frac{\partial v}{\partial t} = -\frac{\partial P}{\partial t} - j\cdot B \tag{B.8}$$

If we take the time derivative of Equation B.6 we obtain

$$\begin{aligned} N\cdot\frac{d^2}{dt^2}R^2 &= 4\pi\int_0^\infty r^2\cdot\left[v\cdot\underbrace{\frac{\partial\rho}{\partial t}}_{\text{cont. eq.}}+\rho\cdot\underbrace{\frac{\partial v}{\partial t}}_{\text{force eq.}}\right]dr \\ &= 4\pi\int_0^\infty r^2\left[-\frac{v}{r}\frac{\partial}{\partial r}(r\cdot\rho\cdot v)-\frac{\partial P}{\partial r}-j\cdot B\right]dr \qquad \text{(B.9)} \\ &= -4\pi\int_0^\infty r\left[\frac{\partial}{\partial r}(r\cdot\rho\cdot v^2)-\underbrace{\rho\cdot v\cdot\frac{\partial v}{\partial r}+r\frac{\partial P}{\partial r}}_{=0}+r\cdot j\cdot B\right]dr \end{aligned}$$

The first integral can be simplified by partial integration

$$\int_0^\infty 2\pi\cdot r\cdot\frac{\partial}{\partial r}(r\cdot\rho\cdot v^2)\,dr=\underbrace{\left[2\pi r^2\cdot\rho\cdot v\right]_{r=0}^{\infty}}_{=0}-\int_0^\infty 2\pi r\cdot\rho\cdot v^2\,dr=-\left\langle v^2\right\rangle N \qquad \text{(B.10)}$$

where we introduced the average of the squared velocity, $\left\langle v^2\right\rangle$. This simplifies Equation B.9, resulting in

$$N\cdot\frac{d^2}{dt^2}R^2=2N\left\langle v^2\right\rangle-\int_0^\infty 4\pi r^2\left(\frac{\partial P}{\partial r}+j\cdot B\right)dr \qquad \text{(B.11)}$$

If we expand the second time derivative

$$\frac{d^2}{dt^2}R^2=2R\cdot\frac{d^2}{dt^2}R+2\left(\frac{dR}{dt}\right)^2 \qquad \text{(B.12)}$$

and use the self-similar edge approximation

$$\left\langle v^2\right\rangle\approx\left(\frac{dR}{dt}\right)^2 \qquad \text{(B.13)}$$

Equation B.11 simplifies to

$$\frac{d^2}{dt^2}R=-\frac{1}{N\cdot R}\int_0^\infty 2\pi r^2\left(\frac{\partial P}{\partial r}+j\cdot B\right)dr \qquad \text{(B.14)}$$

The dynamics of the pinch is determined by the magnetic force $j\cdot B$ and the pressure gradient. Assuming a homogeneous current density j in the channel (I: discharge current)

$$j=\frac{I}{\pi R_{\text{ch}}^2}=\frac{I}{2\pi\cdot R^2}\rightarrow B=\frac{\mu_0 I r}{4\pi R^2} \qquad \text{(B.15)}$$

results in

$$\int_0^\infty 2\pi r^2\,j\cdot B\,dr=\frac{\mu_0 I^2}{4\pi R^4}\int_0^{\sqrt{2}R} r^3\,dr=\frac{\mu_0 I^2}{4\pi} \qquad \text{(B.16)}$$

The integral over the pressure gradient can be simplified by partial integration

$$\int_0^\infty 2\pi r^2 \frac{\partial P}{\partial r}\, dr = -2\int_0^\infty 2\pi r \cdot P\, dr \tag{B.17}$$

leaving an integral over the pressure. The calculation of the pressure term is complicated by the fact that the discharge heats up the channel, so that the channel temperature is not constant. We therefore split the pressure in an adiabatic part P_{ad}, that describes the channel pressure if no heating takes place, and a part P_{heat} that takes the temperature increase due to heating into account:

$$P \approx P_{\mathrm{ad}} + P_{\mathrm{heat}} \tag{B.18}$$

The adiabatic part can be calculated from the initial conditions

$$P_{\mathrm{ad}} = P_0 \cdot \left(\frac{\rho}{\rho_0}\right)^{\gamma} = P_0 \cdot \left(\frac{R_0}{R}\right)^{2\gamma} \tag{B.19}$$

since the density is proportional to $1/R^2$. So the first part of the integral in Equation B.17 yields

$$\int_0^{\sqrt{2}R} 2\pi r P_0 \cdot \frac{R_0^{2\gamma}}{R^{2\gamma}}\, dr = 2\pi \cdot P_0 \cdot \frac{R_0^{2\gamma}}{R^{2\gamma-2}} \tag{B.20}$$

The pressure increase due to ohmic heating is more difficult to calculate. The change in the energy density ε caused by ohmic heating depends on the conductivity σ and the current density

$$\frac{d\varepsilon}{dt} = j \cdot E = \frac{j^2}{\sigma} = \frac{I^2}{\sigma \pi^2 R_{\mathrm{ch}}^4} = \frac{I^2}{4\pi \sigma R^4} \tag{B.21}$$

The total increase is calculated by integrating over time

$$\Delta\varepsilon(t) = \int_0^t \frac{I^2(\tau)}{\sigma(\tau)\, \pi^2 R^4(\tau)}\, d\tau \tag{B.22}$$

The pressure increase caused by this heating is given by

$$P_{\mathrm{heat}} = \frac{2}{f}\Delta\varepsilon \tag{B.23}$$

and depends on the degrees of freedom f. Inserting this in the pressure integral yields

$$\int_0^{\sqrt{2}R} 2\pi r P_{\mathrm{heat}}\, dr = \frac{2\pi R^2}{f}\int_0^t \frac{I^2(\tau)}{\sigma(\tau)\, \pi^2 R^4(\tau)}\, d\tau \tag{B.24}$$

Putting this in Equation B.14 yields a differential equation for the chamber radius

$$\frac{d^2}{dt^2} R = \frac{1}{N \cdot R}\left(4\pi P_0 \frac{R_0^{2\gamma}}{R^{2\gamma-2}} + \frac{4R^2}{f\pi}\int_0^t \frac{I^2(\tau)}{R^4(\tau) \cdot \sigma(\tau)}\, d\tau - \frac{\mu_0 I^2}{4\pi}\right) \tag{B.25}$$

For $f = 3$, that is $\gamma = 5/3$, the final result is therefore

$$\frac{d^2 R}{dt^2} = -\frac{\mu_0 \cdot I^2}{4\pi N \cdot R} + \frac{4\pi P_0 \cdot R_0^{10/3}}{N \cdot R^{7/3}} + \frac{4R}{3\pi N}\int_0^t \frac{I^2(\tau)}{R^4(\tau) \cdot \sigma(\tau)}\, d\tau \tag{B.26}$$

Solving this differential equation yields the channel radius $R_{\mathrm{ch}}(t) = \sqrt{2} \cdot R(t)$.

C. CYCLOPS

CYCLOPS is a one-dimensional magnetohydrodynamical code developed at LBNL to study the dynamics of z-pinches. The reduction to one spatial dimension is achieved by assuming cylindrical symmetry and neglecting variations along the channel axis, for example end effects near the electrodes. Using cylindrical coordinates, all plasma parameters then depend only on the radial coordinate r and the time t. The code uses a Lagrangian fluid description, so mass conservation is guaranteed. At the beginning of the simulation, the volume of the discharge chamber is divided in con-axial cylindrical shells with a volume V_i, which is given by

$$V_i = l_{\mathrm{ch}} \cdot \pi \cdot (r_{i+1}^2 - r_i^2) \tag{C.1}$$

where l_{ch} is the length of the discharge chamber, r_i the inner radius of the shell and r_{i+1} the outer radius of the shell. As the numerics is Lagrangian, the mass inside the shells stays constant during the whole simulation, thus resulting in a change of mass density ρ given by

$$\rho_i(t) = \rho_i(t=0) \cdot \frac{r_{i+1}^2(t=0) - r_i^2(t=0)}{r_{i+1}^2(t) - r_i^2(t)} \tag{C.2}$$

The plasma is modelled by a MHD model, which assumes identical electron and ion temperatures and quasi-neutrality, so that the whole plasma dynamics is described by the electron dynamics. The evolution of the electron particle density is governed by a continuity equation that takes ionization as well as recombination into account:

$$\frac{\partial n_e}{\partial t} + \nabla \cdot (\mathbf{v} n_e) = \underbrace{\alpha \cdot n_e}_{\text{ionization}} - \underbrace{\alpha_r \cdot n_e^2}_{\text{recombination}} \tag{C.3}$$

The ionization is governed by an avalanche coefficient that depends on the density and the electric field. The avalanche coefficient is calculated from an empirical model[Sha98]

$$\alpha = \frac{C_0 \cdot p_{\mathrm{eff}} \cdot S^3}{1 + C_1 \cdot S + C_2 \cdot S^2 + C_3 \cdot S^3} \tag{C.4}$$

The function S is given by

$$S = E_z^2 / P_0^2 \tag{C.5}$$

with $p_{\mathrm{eff}} = \max(0, \kappa T_0 (n_g - n_e))$, $p_0 = n_g \kappa T_0$, and $T_0 = 273.15\mathrm{K}$. The parameters C_i are empirical fitting parameters which depend on the gas used in the chamber.

The evolution of the fluid velocity v is described in the force equation, which considers the magnetic force as well as the effect of pressure gradients:

$$\rho \cdot \frac{d\mathbf{v}}{dt} = \mathbf{j} \times \mathbf{B} - \nabla p \tag{C.6}$$

where j is the current density, given by Ohm's law

$$\mathbf{j} = \sigma \left(\mathbf{E} + \mathbf{v} \times \mathbf{B} \right) \tag{C.7}$$

where σ is the plasma conductivity, given by

$$\sigma = \frac{e^2 \cdot n_e}{m_e \cdot \nu_m} \tag{C.8}$$

The momentum-transfer collision frequency ν_m is again described by an empirical model[Sha98]

$$\nu_m = A_0 \cdot p_{\mathrm{eff}} \frac{1 + A_1 \cdot T_{\mathrm{eff}}}{1 + A_2 \cdot T_{\mathrm{eff}}} \quad \text{with} \quad T_{\mathrm{eff}} = C_0 \cdot T + \frac{E_z^4}{p_{\mathrm{eff}}^4} \tag{C.9}$$

again with empirical parameters depending on the gas used.

The change in the energy density ε is given by

$$\frac{d\varepsilon}{dt} = - \underbrace{\nabla \cdot \mathbf{q}}_{\text{heat flow}} - \underbrace{\rho (\nabla \cdot \mathbf{v})}_{\text{volume work}} + \underbrace{\mathbf{j} \cdot \mathbf{E}}_{\text{joule heating}} - \underbrace{\sigma_{sb} \cdot T^4 / \lambda}_{\text{radiation}} - \underbrace{E_I (\alpha - \alpha_r \cdot n_e) n_e}_{\text{ionization/recombination}} \tag{C.10}$$

The heat current $\mathbf{q}$ is given by the Fourier ansatz

$$\mathbf{q} = -\kappa \cdot \nabla T \tag{C.11}$$

The pressure is calculated from the ideal gas law

$$p = \frac{\rho}{M} \cdot k_B \cdot T \tag{C.12}$$

where M is the mass of the ions. The electromagnetic fields are connected to the current and charge density by Maxwell's equation. If the displacement current is neglected, which is a typical assumption in MHD and valid as long as no very fast phenomena, such as light propagation, are considered, the Maxwell equations can be combined with Ohm's law and yield a differential equation for the magnetic field

$$\frac{\partial \mathbf{B}}{\partial t} = \nabla \times \left[\mathbf{v} \times \mathbf{B} - \frac{1}{\mu_0 \sigma} \nabla \times \mathbf{B} \right] \tag{C.13}$$

The boundary conditions for the magnetic field are given by $B(r = 0) = 0$ and

$$B(r_{\mathrm{ch}}) = \frac{\mu_0 \cdot I}{2\pi \cdot r_{\mathrm{ch}}} \tag{C.14}$$

where r_{ch} is the chamber radius. The chamber is connected in series with an external capacity, an external resistor, and an external inductance, which model the pulse generator and the cables. The code can model the hydrodynamic expansion after laser heating, the prepulse, and the main discharge.

D. Saha equations

The knowledge of the ionization state of a plasma, especially the effective charge of the ions, is essential to calculate important plasma properties like collision frequencies. If we assume that the plasma is in local thermal equilibrium with a (local) plasma temperature T and density n_e, we can derive the ionization degree by the use of statistical mechanics. In thermal equilibrium, the density ratio between two neighboring charge states z and $z-1$ is given by[Gri64, Hut00]

$$\frac{n_z}{n_{z-1}} = \frac{1}{n_e} \frac{2g_z}{g_{z-1}} \left(\frac{m k_B T}{2\pi\hbar^2} \right)^{3/4} \exp\left(-\frac{E_{z-1} - \Delta E_{z-1}}{k_B T} \right) \tag{D.1}$$

Here g_z is the statistical weight for the charge state z, E_z is the ionization energy for the charge state z, and ΔE_z is the decrease of the ionization energy due to plasma effects. The correction of the ionization energy is given by[Gri64]

$$\Delta E_{z-1} = \frac{z e^2}{4\pi \varepsilon_0 \lambda_D} \tag{D.2}$$

We now determine the ionization degree of an ammonia plasma. Ammonia starts to dissociate at about 2000 K[Ger85]. Since we study temperatures in the electron volt range, we can assume that the ammonia is already fully dissociated and neglect the dissociation process

$$\mathrm{NH_3} \rightarrow 3\,\mathrm{H} + \mathrm{N} \tag{D.3}$$

The possible species in the plasma are HI, HII and NI-NVIII. The ratio of hydrogen to nitrogen is constant, independent of the ionization degree. Furthermore the total charge of the ions must be identical to the negative of the electron charge. If we put this information together, we obtain a system of linear equations:

$$\begin{pmatrix} 1 & 1 & -3 & -3 & -3 & -3 & -3 & -3 & -3 & -3 \\ 0 & 1 & 0 & 1 & 2 & 3 & 4 & 5 & 6 & 7 \\ a_0 & -1 & 0 & 0 & 0 & 0 & 0 & 0 & 0 & 0 \\ 0 & 0 & a_1 & -1 & 0 & 0 & 0 & 0 & 0 & 0 \\ 0 & 0 & 0 & a_2 & -1 & 0 & 0 & 0 & 0 & 0 \\ 0 & 0 & 0 & 0 & a_3 & -1 & 0 & 0 & 0 & 0 \\ 0 & 0 & 0 & 0 & 0 & a_4 & -1 & 0 & 0 & 0 \\ 0 & 0 & 0 & 0 & 0 & 0 & a_5 & -1 & 0 & 0 \\ 0 & 0 & 0 & 0 & 0 & 0 & 0 & a_6 & -1 & 0 \\ 0 & 0 & 0 & 0 & 0 & 0 & 0 & 0 & a_7 & -1 \end{pmatrix} \cdot \begin{pmatrix} n(\mathrm{HI}) \\ n(\mathrm{HII}) \\ n(\mathrm{NI}) \\ n(\mathrm{NII}) \\ n(\mathrm{NIII}) \\ n(\mathrm{NIV}) \\ n(\mathrm{NV}) \\ n(\mathrm{NVI}) \\ n(\mathrm{NVII}) \\ n(\mathrm{NVIII}) \end{pmatrix} = \begin{pmatrix} 0 \\ n_e \\ 0 \\ 0 \\ 0 \\ 0 \\ 0 \\ 0 \\ 0 \\ 0 \end{pmatrix} \tag{D.4}$$

The coefficients a_i are the ratios given by equation (D.1). Solving this equation system yields the composition of the plasma and the effective charge state.

The statistical weight for the hydrogen atom is calculated directly. The calculated Saha equilibrium for an electron density of $n_e = 10^{22}\,1/\mathrm{m}^3$ is plotted in figure D.1.

Species	Ground state	Ionization energy	g_i
NI	$1s^2 2s^2 2p^3$	14.53 eV	20
NII	$1s^2 2s^2 2p^2$	29.60 eV	15
NIII	$1s^2 2s^2 2p^1$	47.45 eV	6
NIV	$1s^2 2s^2$	77.47 eV	28
NV	$1s^2 2s$	97.89 eV	8
NVI	$1s^2$	552.08 eV	1
NVII	$1s$	667.03 eV	2
NVIII	(nucleus)	-	1

Table D.1.: Ionization energies and statistical weights of nitrogen[Nie02, Her45, Arn85, Sob79].

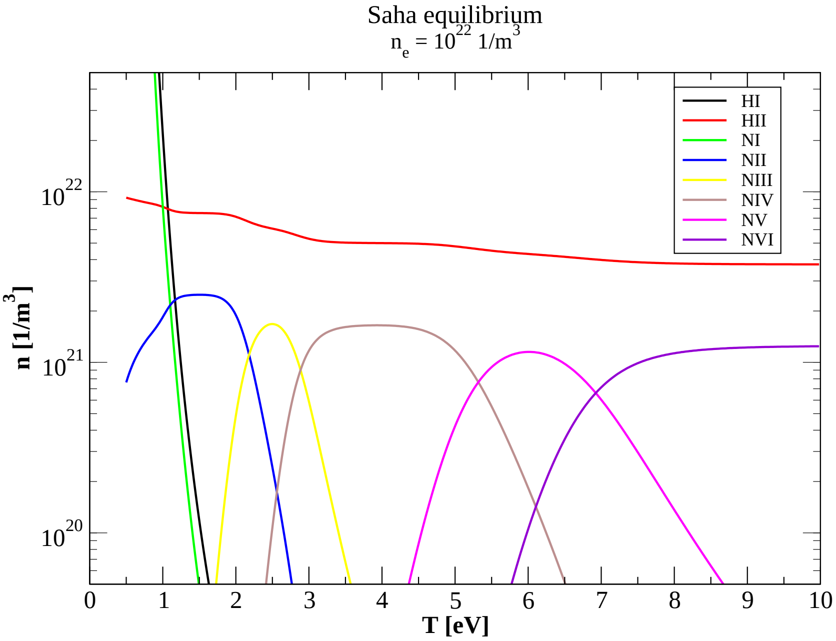

Figure D.1.: Saha equilibrium

Bibliography

[Ahl80] S. P. AHLEN. *Theoretical and experimental aspects of the energy loss of relativistic heavily ionizing particles.* Reviews of Modern Physics, vol. 52 (1), pp. 121–173 (1980).

[Arn85] M. ARNAUD AND R. ROTHENFLUG. *An updated evaluation of recombination and ionization rates.* Astronomy & Astrophysics Supplement Series, vol. 60, pp. 425–457 (1985).

[Atz04] S. ATZENI AND J. MEYER-TER VEHN. *The Physics of Inertial Fusion.* No. 125 in International Series of Monographs on Physics. Oxford Science Publications (2004).

[Bet72] H.-D. BETZ. *Charge States and Charge-Changing Cross Sections of Fast Heavy Ions Penetrating Through Gaseous and Solid Media.* Reviews of Modern Physics, vol. 44 (3), pp. 465–539 (1972).

[Bha76] A. K. BHATTACHARYA. *Measurement of breakdown potentials and Townsend ionization coefficients for the Penning mixtures of neon and xenon.* Physical Review A, vol. 13 (3), pp. 1219–1225 (1976).

[Bha79] A. K. BHATTACHARYA. *Measurement of Townsend ionization coefficients and the breakdown potentials for the Penning mixtures of Ne and Kr.* Journal of Applied Physics, vol. 50 (10), pp. 6207–6210 (1979).

[Bil93] J. BILLEN AND L. YOUNG. *POISSON/SUPERFISH on PC Compatibles.* In *Proceedings of the 1993 Particle Accelerator Conference*, vol. 2, pp. 790–792 (1993).

[Bog91] E. BOGGASCH, J. JACOBY, H. WAHL, K.-G. DIETRICH, D. H. H. HOFFMANN, W. LAUX, M. ELFERS, C. R. HAAS, V. P. DUBENKOV, AND A. A. GOLUBEV. *z-Pinch Plasma Lens Focusing of a Heavy-Ion Beam.* Physical Review Letters, vol. 66 (13), pp. 1705–1708 (1991).

[Bra99] S. BRANDT. *Datenanalyse.* Spektrum Akademischer Verlag (1999).

[Bro66] S. BROWN (editor). *Introduction to Electrical Discharges in Gases.* Series in Plasma Physics. Wiley & Sons (1966).

[Cal02] D. A. CALLAHAN, M. C. HERRMANN, AND M. TABAK. *Progress in heavy ion target capsule and hohlraum design.* Laser and Particle Beams, vol. 20, pp. 405–410 (2002).

[Cel03] C. M. CELATA, F. M. BIENIOSEK, E. HENESTROZA, J. W. KWAN, J. P. LEE, G. LOGAN, L. PROST, P. A. SEIDL, J.-L. VAY, W. L. WALDRON, ET AL. *Progress in heavy ion fusion research*. Physics of Plasmas, vol. 10 (5), pp. 2064–2070 (2003).

[Cha73] D. CHAMPENEY. *Fourier transforms and their physical applications*. Academic Press (1973).

[Coh50] R. COHEN, L. SPITZER, AND P. ROUTLY. *The Electrical Conductivity of an Ionized Gas*. Physical Review, vol. 80 (2), pp. 230–238 (1950).

[Col80] D. G. COLOMBANT, S. A. GOLDSTEIN, AND D. MOSHER. *Hydrodynamic Response of Plasma Channels to Propagating Ion Beams*. Physical Review Letters, vol. 45 (15), pp. 1253–1256 (1980).

[Dru40] M. DRUYVESTEYN AND F. PENNING. *The Mechanism of Electrical Discharges in Gases of Low Pressure*. Reviews of Modern Physics, vol. 12 (2), pp. 87–174 (1940).

[Dru41] M. DRUYVESTEYN AND F. PENNING. *Errata:Mechanisms of Electrical Discharges in Gases of Low Pressures*. Reviews of Modern Physics, vol. 13, pp. 72–73 (1941).

[Fre82] J. FREIDBERG. *Ideal magnetohydrodynamic theory of magnetic fusion systems*. Reviews of Modern Physics, vol. 54 (3), pp. 801–903 (1982).

[Ger85] W. GERHARTZ (editor). *Ullmann's Encyclopedia Of Industrial Chemistry*, vol. A2. VCH (1985).

[Gol98] R. J. GOLDSTON AND P. H. RUTHERFORD. *Plasmaphysik*. Vieweg Lehrbuch (1998).

[Gri64] H. GRIEM. *Plasma Spectroscopy*. McGraw-Hill (1964).

[Ham70] D. A. HAMMER AND N. ROSTOKER. *Propagation of High Current Relativistic Electron Beams*. Physics of Fluids, vol. 13 (7), pp. 1831–1850 (1970).

[Her45] G. HERZBERG. *Atomic Spectra and Atomic Structure*. Dover Publications (1945).

[Hof90] D. H. H. HOFFMANN, K. WEYRICH, H. WAHL, D. GARDÉS, R. BIMBOT, AND C. FLEURIER. *Energy loss of heavy ions in a plasma target*. Physical Review A, vol. 42 (4), pp. 2313–2321 (1990).

[Hub92] R. F. HUBBARD, S. P. SLINKER, M. LAMPE, G. JOYCE, AND P. OTTINGER. *Current Neutralization in Ballistic Transport of Light Ion Beams*. NRL Report 4790, Naval Research Laboratory (1992).

[Hum90] S. HUMPHRIES. *Charged Particle Beams*. John Wiley & Sons (1990).

[Hut00] I. HUTCHINSON. *Principles of Plasma Diagnostics*. Cambridge University Press (2000).

[Jac98] J. D. JACKSON. *Classical Electrodynamics*. 3rd edn. John Wiley & Sons (1998).

[Kag01] I. D. KAGANOVICH, G. SHVETS, E. STARTSEV, AND R. C. DAVIDSON. *Nonlinear charge and current neutralization of an ion beam pulse in a pre-formed plasma*. Physics of Plasmas, vol. 8 (9), pp. 4180–4192 (2001).

[Kip75] R. KIPPENHAHN AND C. MÖLLENHOFF. *Elementare Plasmaphysik*. B.I. Wissenschaftsverlag (1975).

[Kno04] R. KNOBLOCH. *Beam Emittance Measurement and Plasma Channel Properties in Channel-based Ion Beam Transport*. Diplomarbeit (2004).

[Law73] J. LAWSON, P. LAPOSTOLLE, AND R. GLUCKSTERN. *Emittance, Entropy and Information*. Particle Accelerators, vol. 5, pp. 61–65 (1973).

[Lej80] C. LEJEUNE AND J. AUBERT. *Advanced Electronics and Electron Physics, Supplement 13A*, chap. Emittance and Brightness: Definitions and Measurements, pp. 159–259. Academic Press (1980).

[Lib90] R. L. LIBOFF. *Kinetic Theory*. Prentice Hall (1990).

[Lin98] J. LINDL. *Inertial Confinement Fusion*. AIP Press (1998).

[Man73] W. M. MANHEIMER, M. LAMPE, AND J. P. BORIS. *Effect of a surrounding gas on magnetohydrodynamic instabilites in a Z pinch*. Physics of Fluids, vol. 16 (7), pp. 1126–1134 (1973).

[Nar82] E. NARDI AND Z. ZINAMON. *Charge State and Slowing of Fast Ions in a Plasma*. Physical Review Letters, vol. 49 (17), pp. 1251–1254 (1982).

[Nat68] NATIONAL BUREAU OF STANDARDS. *Electrical breakdown in ammonia at low pressure*. Report 9882 (1968).

[Nef02] S. NEFF. *Diagnostik und Simulation eines laserinduzierten Plasmakanals für Ionenstrahltransportexperimente*. Diplomarbeit, TU Darmstadt (2002).

[Nef03] S. NEFF, A. TAUSCHWITZ, C. NIEMANN, D. PENACHE, D. H. H. HOFFMANN, S. YU, AND W. SHARP. *Gas density measurements with heavy ion beams*. Journal of Applied Physics, vol. 93 (5), pp. 3079–3081 (2003).

[Nef04] S. NEFF, D. H. H. HOFFMANN, R. KNOBLOCH, C. NIEMANN, D. PENACHE, A. TAUSCHWITZ, AND S. YU. *Heavy-ion Beam Transport in Plasma Channels*. In *Proceedings EPAC 2004* (2004).

[Nie99] C. NIEMANN, D. PONCE, S. YU, W. LEEMANS, T. FESSENDEN, G. DAHLBACKA, K. VANDERSLOOT, W. SHARP, AND A. TAUSCHWITZ. *Faraday Rotation Measurements in a Laser Initiated Discharge Channel for Ion Beam Transport*. In *APS Plasma Physics Meeting, Seattle, Washington* (1999).

[Nie01] C. NIEMANN, D. PONCE, S. YU, G. DAHLBACKA, T. FESSENDEN, W. LEEMANS, A. TAUSCHWITZ, AND D. H. H. HOFFMANN. *Development of a Faraday Polarimeter for Magnetic Field Measurements in a Discharge Channel for Ion Beam Transport.* Nuclear Instruments and Methods A, vol. 464, pp. 339–342 (2001).

[Nie02] C. NIEMANN. *Plasma diagnostics of discharge channels for neutralized ion-beam transport.* Dissertation TU Darmstadt (2002).

[Nie03a] C. NIEMANN, S. NEFF, A. TAUSCHWITZ, D. PENACHE, R. BIRKNER, C. CONSTANTIN, R. KNOBLOCH, R. PRESURA, F. ROSMEJ, D. H. H. HOFFMANN, AND S. YU. *Laser-guided, intersecting discharge channels for the final transport in heavy-ion fusion.* Journal of Applied Physics, vol. 93, pp. 9470–9476 (2003).

[Nie03b] C. NIEMANN, D. PENACHE, A. TAUSCHWITZ, F. ROSMEJ, S. NEFF, R. BIRKNER, C. CONSTANTIN, R. KNOBLOCH, R. PRESURA, S. YU, ET AL. *Diagnostics of discharge channels for neutralized chamber transport in heavy ion fusion.* Laser and Particle Beams, vol. 21, pp. 13–15 (2003).

[Nie03c] C. NIEMANN, F. ROSMEJ, A. TAUSCHWITZ, S. NEFF, D. PENACHE, R. BIRKNER, C. CONSTANTIN, R. KNOBLOCH, R. PRESURA, D. H. H. HOFFMANN, S. YU, AND R. LEE. *Spectroscopic density and temperature measurements and modelling of a discharge plasma for neutralized ion-beam transport.* Journal of Physics D, vol. 36 (17) (2003).

[Ols81a] J. N. OLSEN. *Laser-initiated channels for ion transport:*CO_2*-laser absorption and heating of* NH_3 *and* C_2H_4 *gases.* Journal of Applied Physics, vol. 52 (5), pp. 3279–3285 (1981).

[Ols81b] J. N. OLSEN AND L. BAKER. *Laser-initiated channels for ion transport: Breakdown and channel evolution.* Journal of Applied Physics, vol. 52 (5), pp. 3286–3292 (1981).

[Ols82] J. N. OLSEN AND R. J. LEEPER. *Ion beam transport in laser-initiated discharge channels.* Journal of Applied Physics, vol. 53 (5), pp. 3397–3404 (1982).

[Ott79] P. F. OTTINGER, D. MOSHER, AND S. A. GOLDSTEIN. *Microstability of a focused ion beam propagating through a z-pinch plasma.* Physics of Fluids, vol. 22 (2), pp. 332–337 (1979).

[Ott80] P. F. OTTINGER, D. MOSHER, AND S. A. GOLDSTEIN. *Propagation of intense ion beams in straight and tapered z-discharge plasma channels.* Physics of Fluids, vol. 23 (5), pp. 909–920 (1980).

[Ott81a] P. F. OTTINGER AND S. A. GOLDSTEIN. *Stability Considerations for Light-Ion Beam Transport in Z-Discharge Channels.* NRL Report 4548, Naval Research Laboratory (1981).

[Ott81b] P. F. OTTINGER, D. MOSHER, AND S. A. GOLDSTEIN. *Electromagnetic instabilities in a focused ion beam propagating through a z-discharge channel.* Physics of Fluids, vol. 24 (1), pp. 164–170 (1981).

[Ott82] P. F. OTTINGER, S. A. GOLDSTEIN, AND D. MOSHER. *Constraints on Transportable Ion Beam Power.* NRL Memorandum Report 4948, Naval Research Laboratory (1982).

[Ott00] P. F. OTTINGER, F. C. YOUNG, S. J. STEPHANAKIS, D. V. ROSE, J. M. NERI, B. V. WEBER, M. C. MYERS, D. D. HINSHELWOOD, D. MOSHER, C. L. OLSON, AND D. R. WELCH. *Self-pinched transport of an intense proton beam.* Physics of Plasmas, vol. 7 (1), pp. 346–358 (2000).

[Pau00] W. PAULI. *Electrodynamics*, vol. 1 of *Pauli Lectures on Physics*. Dover Publications (2000).

[Pen02a] D. PENACHE, C. NIEMANN, A. TAUSCHWITZ, R. KNOBLOCH, S. NEFF, R. BIRKNER, M. GEISSEL, D. H. H. HOFFMANN, R. PRESURA, C. PENACHE, M. ROTH, AND H. WAHL. *Experimental investigation of ion beam transport in laser initiated plasma channels.* Laser and Particle Beams, vol. 20, pp. 559–563 (2002).

[Pen02b] D. PENACHE, C. NIEMANN, A. TAUSCHWITZ, R. PRESURA, R. KNOBLOCH, S. NEFF, M. GEISSEL, D. H. H. HOFFMANN, C. PENACHE, M. ROTH, AND H. WAHL. *Transport Experiments of a 2.2 GeV Gold Ion Beam in a Plasma Channel at the GSI-UNILAC facility.* In *Proceedings Pulsed Power Plasma Science (PPPS), Las Vegas*, pp. 1354–1357 (2002).

[Pen02c] D. L. PENACHE. *Heavy-ion Beam Transport in Laser-initiated High-current Gas-discharge Channels.* Dissertation TU Darmstadt (2002).

[Res99] Research Systems, Boulder (USA). *Using IDL* (1999).

[Ros04] D. V. ROSE, D. R. WELCH, C. L. OLSEN, S. S. YU, S. NEFF, W. M. SHARP, AND THE ARIES TEAM. *Impact of the Beam Transport method on the Chamber and Driver Design for Heavy Ion Inertial Fusion.* Fusion Science and Technology, vol. 46 (3), pp. 470–493 (2004).

[Saw00] M. E. SAWAN, R. R. PETERSON, AND S. S. YU. *Shielding analysis for a heavy ion beam chamber with plasma channels for ion transport.* Fusion Engineering and Design, vol. 51-52, pp. 1137–1142 (2000).

[Sch87] M. SCHWARTZ. *Principles of Electrodynamics.* Dover Publications (1987).

[Sha98] W. M. SHARP, T. J. FESSENDEN, E. P. LEE, AND S. S. YU. *Numerical Models in CYCLOPS.* Tech. rep., Lawrence Livermore National Laboratory (1998).

[Sim71] K. SIMONYI. *Theoretische Elektrotechnik.* Deutscher Verlag der Wissenschaften (1971).

[Sob79] I. SOBELMAN. *Atomic Spectra and Radiative Transitions.* Springer (1979).

[Spa90] K.-H. SPATCHEK. *Theoretische Plasmaphysik.* Teubner Studienbücher (1990).

[Spi53] L. SPITZER AND R. HÄRM. *Transport Phenomena in a Completely Ionized Gas.* Physical Review, vol. 89 (5), pp. 977–981 (1953).

[Spi56] L. SPITZER. *Physics of Fully Ionized Gases.* Interscience Publishers (1956).

[Tab97] M. TABAK AND D. CALLAHAN-MILLER. *Design of a distributed radiator target for inertial fusion.* In *Nuclear Instruments and Methods A*, vol. 415, pp. 75–84. Elsevier (1997).

[Tau93] A. TAUSCHWITZ. *Die stromtragende Plasmalinse, eine effektive Möglichkeit zur Fokusierung hochenergetischer Teilchenstrahlen.* Dissertation, TH Darmstadt (1993).

[Tau95] A. TAUSCHWITZ, E. BOGGASCH, D. H. H. HOFFMANN, J. JACOBY, U. NEUNER, M. STETTER, S. STÖWE, R. TKOTZ, M. DE MAGISTRIS, AND W. SEELIG. *Heavy-ion beam focusing with a wall-stabilized plasma lens.* Laser and Particle Beams, vol. **13** (2), pp. 221–229 (1995).

[Tau96a] A. TAUSCHWITZ. *Plasma lens focusing and plasma channel transport for heavy ion fusion.* Fusion Engineering and Design, vol. 493, pp. 32–33 (1996).

[Tau96b] A. TAUSCHWITZ, S. YU, R. BANGERTER, J. BARNARD, S. EYLON, T. FESSENDEN, J. KWAN, W. LEEMANS, C. PETERS, L. REGINATO, AND W. SHARP. *Plasma Lens Focusing and Plasma Channel Transport for Heavy Ion Fusion.* Fusion Engineering and Design, vol. 32-33, pp. 493–502 (1996).

[Tau96c] A. TAUSCHWITZ, S. YU, R. BANGERTER, J. BARNARD, S. EYLON, T. FESSENDEN, J. KWAN, W. LEEMANS, C. PETERS, L. REGINATO, AND W. SHARP. *Plasma Lens Focusing and Plasma Channel Transport for Heavy Ion Fusion.* In *Proceedings of the International Conference of High Power Particle Beams, Prague,* pp. 91–94 (1996).

[Tau99] A. TAUSCHWITZ, C. NIEMANN, D. PENACHE, R. PRESURA, E. WILLE, U. N. FUNK, M. GEISSEL, D. H. H. HOFFMANN, U. NEUNER, A. GOLUBEV, ET AL. *Ion Beam Transport in a Laser initiated Discharge Channel.* In *Proc. Int. Conf. on Inertial Fusion Sciences and Applications (IFSA), Bordeaux,* pp. 521–526 (1999).

[Tau01] A. TAUSCHWITZ. *Space charge and current neutralized transport and focusing of heavy ion beams with discharge plasmas.* Habilitation, TU Darmstadt (2001).

[Tau02] A. TAUSCHWITZ, C. NIEMANN, D. PENACHE, R. BIRKNER, D. H. H. HOFFMANN, R. KNOBLOCH, S. NEFF, R. PRESURA, D. PONCE, F. ROSMEJ, AND S. YU. *Plasma Channel Transport for Heavy Ion Fusion: Investigation of Beam Transport, Channel Initiation and Stability*. In *Proceedings International Conference on High Power Particle Beams, Albuquerque*, pp. 391–396. AIP (2002).

[Wei59] E. S. WEIBEL. *Spontaneously growing transverse waves in a plasma due to an anisotropic velocity distribution*. Physical Review Letters, vol. 2 (3), pp. 83–84 (1959).

[Wel01] D. R. WELCH, D. V. ROSE, B. V. OLIVER, AND R. E. CLARK. *Simulation techniques for heavy ion fusion chamber transport*. Nuclear Instruments and Methods in Physics Research A, (464), pp. 134–139 (2001).

[Wel02] D. R. WELCH, D. V. ROSE, B. V. OLIVER, T. C. GENONI, R. E. CLARK, C. L. OLSON, AND S. S. YU. *Simulations of intense heavy ion beams propagating through a gaseous fusion target chamber*. Physics of Plasmas, vol. 9 (5), pp. 2344–2352 (2002).

[Wel03] D. R. WELCH, T. C. GENONI, D. V. ROSE, B. V. OLIVER, R. E. CLARK, C. L. OLSON, AND S. S. YU. *Assisted-pinch transport of heavy-ion beams in a fusion chamber*. Physics of Plasmas, vol. 10 (6), pp. 2442–2448 (2003).

[Wit73] A. WITTIKOWER AND H. BETZ. *Equilibrium-charge-state Distributions of Energetic Ions ($Z > 2$) in Gaseous and Solid Media*. Atomic Data, vol. 5 (2), pp. 113–159 (1973).

[You93] F. C. YOUNG, D. D. HINSHELWOOD, R. F. HUBBARD, M. LAMPE, J. M. NERI, C. L. OLSON, P. F. OTTINGER, D. V. ROSE, S. P. SLINKER, S. J. STEPHANAKIS, AND D. R. WELCH. *Current Neutralization of Intense MeV Proton Beams Transported in Low-Pressure Gas*. Physical Review Letters, vol. 70 (17), pp. 2573–2577 (1993).

[Zie85] J. ZIEGLER, J. BIERSACK, AND U. LITTMARK. *The Stopping and Range of Ions in Solids*. Pergamon Press (1985).

Acknowledgments

Hereby I would like to thank all the people that contributed to this work and thus made it possible. In particular I would like to thank:

Professor Dr. Dr. h.c./RUS Dieter Hoffmann for the opportunity of take part in this interesting research project and the research at the Lawrence Berkeley National Laboratory and for making it possible for me to join the *Graduiertenkolleg Physik und Technik von Beschleunigern*.

Dr. Andreas Tauschwitz for his support and guidance in modifying and carrying out the experiments and for providing new ideas and impulses for my work. He was also very helpful with the proof-reading of the manuscript.

Dr. Simon Yu for giving me new insights and a much better overview over the ARIES project in general and especially the assisted pinched mode. I would also like to thank him for his support during my stay at Berkeley and the opportunity to take part at the ARIES group meetings.

My colleague Renate Knobloch for her assistance in preparing and carrying out the experiments and for proof-reading the manuscript. I also would like to thank my former colleagues Dr. Christoph Niemann and Dr. Dan Lucius Penache for getting me started in the experiment, their previous work being the starting point of my thesis.

Finally I would like to thank the members of the plasma physics group at GSI for the good working atmosphere and their support. Also I would like to thank the members of the AFRD group at Berkeley for their hospitality and the good working atmosphere during my stay in Berkeley.

Lebenslauf

Persönliche Angaben

Name	Stephan Neff
Anschrift	Am Seeberg 17, 64625 Bensheim
Geburtsdatum	27.09.1975
Geburtsort	Bensheim
Staatsangehörigkeit	Deutsch
Familienstand	Ledig

Ausbildung

1982 - 1986	Grundschule Reichenbach
1986 - 1995	Altes Kurfürstliches Gymnasium, Bensheim
1995	Abitur
Oktober 1995-März 1996	1. Semester Physik an der TU Darmstadt
April 1996-Februar 1997	Grundwehrdienst
April 1997 - Februar 2002	Fortsetzung des Diplomstudiums an der TU Darmstadt
Februar 2002	Diplom der Physik. Diplomarbeit: ‘Diagnostik und Simulation eines laserinduzierten Plasmakanals für Ionenstrahltransportexperimente’
April 2002	Beginn der Doktorarbeit in der Plasmaphysik Arbeitsgruppe der GSI
April 2002 - Oktober 2002	Forschungsaufenthalt am Lawrence Berkeley National Laboratory in der Arbeitsgruppe Fusion and Accelerator Design

Hiermit erkläre ich, dass ich die Arbeit selbständig und nur mit den angegebenen Hilfsmitteln angefertigt und nicht schon früher eine Promotion versucht habe.

31. Januar 2005 Stephan Neff